Thermographic inspection to provide quality assurance for reinforced 3D printer filaments

A thesis

submitted in fulfilment

of the requirements for the degree

of

Master in Engineering

at

The University of Waikato

by

Monique Ding Yi Huang

2020

Abstract

This research demonstrates the feasibility of active thermography in inspecting 3D printing filaments. Examine the potential of pulsed phase thermography in quality assurance of short and natural fibre reinforced polymer composites. Signal analysis scripts were built in Matlab to process the raw data recordings collected. These scripts included were; Single Pixel Analysis (SPA) that consisted of 2D wavelet denoising and single pixel plotted through time; Thermal Signal Reconstruction (TSR); and Pulsed Phase Thermography (PPT) that implemented the inbuilt with Fast Fourier Transform (FFT). 3D printed natural fibre composites offer sustainable and cost-effective solutions to material challenges. When considering combining natural fibres and 3D printing there are several manufacturing challenges that must be overcome. The focus of this research is to ascertain if active thermography is a suitable tool for online inspection of fibre reinforced filaments used for 3D printing composites. The aim of the inspection is to identify fibre rich and fibre poor regions along the filament, where uniformly distributed fibres and heating along the filament are preferred. Regions with a locally high weight percent of fibres, known as a fibre bunch, can cause problems when used to print a part resulting in a waste of materials and failed print jobs. The paper presents a feasibility study showing the potential of using pulsed thermography to identify fibre bunching. An external heating stimulus is applied to the sample and an infrared detector is used to monitor the thermal decay. The thermal contrast produced by fibre bunches compared to regions of uniformly distributed fibres is used to identify potential problem areas and provide a means of quality control. Investigation includes variation of the heating stimulus, data collection and data processing routines. Flat bottom holes (FBH) and notches of the samples were easiest to detect, filaments mixed with fibres and salt were more challenging and difficult to detect, which will require further investigations.

Acknowledgements

I wish to express my warmest gratitude to everyone has been through this journey with me.

First and foremost I would like to thank my parents for all that they have given throughout my lifetime.

I wish to give special thanks to my academic supervisor, Dr. Rachael Tighe, for her incredible academic supervision and personal support in every step of the way in the research.

I wish to thank my co-supervisor, Dr. John Mcdonald-Wharry, for his academic support and guidance.

I wish to thank Prof. Kim Pickering for providing the samples.

I wish to give warm thanks to Cheryl Ward, for her tireless support and assistance.

I also wish to thank the MAPE technicians who provided the technical assistance for my research, especially Pete,Higgins, Dr. Stella, Helen, Duncan

I would like thank my friends and also the other composites group members, Maria Oliveira and Tom Sunny.

I am also grateful to my sweetest friends, Dr. Safiya Noorzai, Dr. Khadija Bahiss, Deron and Maria for their constant encouragement and valuable suggestions.

And finally, I would like to thank God (SWT) for everything and everyone.

Table of Contents

List of Figures

List of Tables

List of Abbreviations

PLA	Polylactic acid
IR	Infrared
PT	Pulse thermography
PPT	Pulsed phase thermography
LT	Lock-in thermography
NFCs	Natural fibre reinforced composites
3D	Three dimensional
IRT	Infrared thermography
PPT	Pulsed phase thermography
DTT	Dynamic thermal tomography
2D	Two dimensional
NDE	Non-destructive evaluation
AM	Additive manufacturing
FDM	Fused deposition modelling
CAD	Computer-aided design
ET	Electromagnetic testing
VT or VI	Visual testing
AE	Acoustic emission
UT	Ultrasonic testing
FBH	Flat bottom holes
PMMA	Polymethyl methacrylate
SEM	Scanning electronic microscope
SNR	Signal-to-noise
NaCl	Sodium chloride (salt)
SAW	Surface acoustic wave
FFT	Fast Fourier transform
FOV	Field of view
XCT	X-ray computed tomography
RT	Radiographic testing
TOFD	Time of flight diffraction
ABS	Acrylonitrile-butadiene-styrene
SLA	Stereolithography
DLP	Digital light processing
LOM	Laminated object manufacturing
EBM	Electron (digital) beam melting

Chapter 1

Introduction

1.1 Background and motivation

1.1.1 Additive Manufacturing (AM)

Three dimensional (3D) printing technologies are also known as additive manufacturing (AM). Over the recent years, the popularity of AM grew rapidly, particularly among aerospace, automotive and medical industries. AM technologies are used to fabricate highly complex computerized geometrical, light weighted and compatible parts [1]. AM first gained its popularity in architectural uses, where 3D printed structure models were for demonstrational purposes. Nowadays, AM process have developed living functional tissues such as vascularized cardiac patches and small-scale human hearts [2], a 3D printer can be used to fabricate novel electromagnetic structures for electromagnetic architecture control [3]. The potentials of 3D printing was therefore expanded from fabrication of mechanical materials to the integration of electrical circuits/elements of manufacturing process, such as electrochemical sensors of different geometries [3-8].

The most commonly used 3D printing technique is Fused Deposited Modelling (FDM), because it has a wide variety of machine sizes, it is cost-effective, is reliable in making 3D products with good resolution, dimension and stability [9]. FDM refers to the process where successive layers of material are deposited based on computerized control into a controlled environment to print 3D products. FDM has great flexibility and easily integrated with computerized software such as SolidWorks and computer-aided design (CAD) software packages. FDM technique is commonly used in creating prototypes, conceptual models and engineering components for different industries.

FDM is a thermally controlled technique, in which materials such as thermoplastic composites were melted prior to the deposition process. Important factors for FDM printing are; thermal properties of materials such as glass transition temperature and rheological properties of materials such as melt flow index (MFI) [10]. The main limitations of using 3D printing methods such as FDM in industrial applications are the narrow range of available materials and that fabricated parts are mostly used for demonstrational or conceptual purposes only [10].

In FDM process, filaments are molten, extruded, deposited, cooled, solidified and bonded with the adjoining material. The final product is the result of incremental layers built by repeated procedures of next depositing materials [11]. Prototypes as such are composite structures composed of partially bonded filaments [11]. The most common filament materials used in FDM are unreinforced polymers, which however have limited applications [1; 12].

1.1.2 Polymer composites

Fibre-reinforced polymer composites have been investigated for both industrial and academic purposes [13; 14] [15].. For decades, a variety of materials have been reinforced by natural or synthetic fibres and these composites have provided users with incredible advantages in terms of mechanical properties [16]. The quality of the natural fibre reinforced polymer composites can be variable and can be difficult to assess. This is mainly due to the multiple interfaces, complex geometries and different properties that different composites have [17].

The whole lifecycle and specific properties of the polymer composites may vary and this may influence the quality assurance techniques of materials. The main concern of production processes are cost-effectiveness and material wastage, and one way this can be addressed is by inspecting the quality of the materials prior to production process (such as 3D printing production).

As an example, in FDM process, the machine is sensitive to material defects such as aggregated fibres which blocks the nozzle and formation of air bubbles/voids. Both of these types of filament irregularities or defects can cause 3D printing parts to fail or lower the quality of the printed part.

1.1.3 Non-destructive evaluation

Non-destructive testing inspection of the filament before it reaches the 3D printing process can provide an opportunity to two reject defective filament/materials and reduce 3D printing failures in return.

There is a variety of non-destructive evaluation (NDE) available; radiography, ultrasonic testing and infrared thermography (IRT) [18-20]. IRT in particular is used in quality assurance process of composites materials, as well as in bonded joints of components [21]. The most prominent advantage of IRT is that IRT can be performed safely and quickly, whereas radiography has health and safety restrictions, and ultrasonic testing takes longer (and complex equipment) depending on the scale of component [22; 23]. The main concern of IRT is the limited depths it can inspect, limited at scale of millimetres [24].

1.2 Aims and objectives

The main goals of this research project were to detect fibre clumps which were the ultimate defect of interest as they block 3D printer nozzles. By determining the defect depth detecting limit, the feasibility in identifying defects and irregularities of the available samples was also defined. These defects could include: air bubble or inclusion of other types of voids, fibre aggregation due to bunching or tangles of fibres and other possible subsurface defects.

All samples except for 10 wt% and 30 wt% harakeke reinforced polymers were custom made throughout the research project [15; 25]. These two samples were the ultimate goal in terms of the complex and difficult to analyse the real-world reinforced fibre filaments.

The simpler samples were custom-made with larger and more distinct defects to test the feasibility of IRT inspection approach developed in this research project. A list of the samples used were ordered by increasing inspection difficulty.

1. Inspecting the artificial flat bottom holes milled on a flat surface; PMMA plate, - holes of various depths but constant diameter.
2. Inspecting the artificial square notes on non-flat surfaces; pure PLA filaments. The filaments were painted matt black to minimise the reflections. Notches were varied in depths and had the same width.
3. Inspecting PLA filaments mixed with large salt particles, which varied in sizes and observed under optical microscope.
4. Inspecting PLA filaments mixed with small percentages of untreated (coarse and unpulped) harakeke fibres, this was used as a model defect for a large fibre aggregate /bunch.
5. Inspecting treated harakeke fibre reinforced polymers with higher weight percentages of fibres mixed.

Overall, the sizes, depths and types of defects were inspected under IRT and processed with the specially scripted Matlab.

1.3 Project Overview

A larger range of artificial defects were custom-made for exploring the boundaries of the IRT technique developed in this project. Based on the types of defects used; the easiest defect to detect was the flat bottom holes. Flat bottom holed defects (FBH) were previously tested in 2002, when the calibration of FBH enabled to establish a mathematical relationship between the translation factor and the observed structure depth [26]. This was where the advantages of Fourier PPT was applied and its defect depth estimation was independent of the shape/size of the defect, however the sensitivity of the calibration process has its disadvantages. Based on this, smaller flat bottom holes (3x smaller) and increasing in varieties of samples were tested in this project. Sample varieties of this project were: Flat bottom holes and square notches of various depths on different materials surfaces, mixture of particles of various sizes and types and a range of different weight percentages of the natural fibre mixture/reinforcements.

Pure polylactic acid (PLA) filaments with artificial defects were inspected after the flat bottom holed defects on Polymethyl methacrylate (PMMA) plate. NaCl and low weight percentage (wt %) of coarse harakeke fibres mixed with PLA filaments were the following samples for inspections. The non-commercialised natural fibre reinforced polymers; harakeke reinforced polymers were inspected last.Using experimental methods of pulse thermography (PT) and processed the signal data using established online inspection processing such as thermal signal reconstruction (TSR) and pulsed phase thermography (PPT). An additional signal processing technique known as two-dimensional (2D) wavelet denoising was used to aid the process and plotted temporal data for data and image analysis.

There are six chapters in this thesis. The first chapter comprises of the background and motivation of the project and introduced the objectives to address the aims of this project. The second chapter provides a general overview of polymer composites, AM of polymer composites, review of the non-destructive evaluations (NDE), signal data processing and applications of thermography on natural fibre reinforced composites (NFC).

In Chapter 3, where the NDE techniques applied throughout this project were described in detail. This included inspection of different types of defects and other abnormal thermal response of the objects. Within the signal data processing, the collected thermal data and the processed pulsed phase values were evaluated and stored for defects identifications.

Chapter 4, contains the results and discussion of experimental work illustrated along with Matlab plotted figures. This included figures, thermal images (thermograms) and phase images, which were analysed to provide information on defects.

Based on the findings of the experimental observations and analysis, the conclusion of the experimental work and corresponding problems were summarised in Chapter 5. Recommendations of future work were also presented in this chapter.

Chapter 2

Literature Review

2.1 Polymers and composites

Developments in various manufacturing techniques have accelerated the investigations and productions of polymer products.

2.1.1 General Background

Polymers are categorised into thermosets (phenolic, epoxies) and thermoplastics (semi-crystalline and amorphous samples) [27]. The primary difference is that thermoplastics can be melted [28], whereas thermosets cannot, therefore thermosets and thermoplastics are used in different applications.

Composite materials are when two or more different materials are combined to form the materials that offer the means of overcoming limitations of traditional structural materials [29]. Enhanced mechanical performance of polymers by reinforcing them is a basic composite property.

Thermoplastic composites offer substantial advantages over other thermoplastics [30]. Higher toughness of the matrix material, in which the thermoplastics composites off higher impact resistance. The manufacturing cycles times includes melting process of the matrix, shaping and the consolidation with cooling are shorter than with thermoset counterpart [31].

Currently, most commercialised polymer products are difficult to recycle or degrade, therefore to improve sustainability investigations into alternative materials are ongoing. There is a large demand for biodegradable polymers and composites driven by environmental and health concerns over current commercial products [32].

Over the years, the possibilities in polymer composites' applications have extended from aerospace industries into architectural industries and medical industries [1; 33; 34].

Polymer composites can be reinforced with compatible materials, one of which was in the matrix phase and another could be in either particle or fibre form [35]. Natural materials (fibres) such as hemp and flax are of the popular options for reinforcing polymers [36]. Reinforced polymer composites can be used to address the strength and functionality limitations of pure polymers and can be produced by a rapid tooling and manufacturing technique; 3D printed polymer composites [1].

Fibre volume fraction is a measurement to be considered in signal data processing (online inspection). It is also known as the maximum fibre ratio. Maximum fibre ratio varies theoretically depending on the shapes of the fibres and the directions of their configurations. Fibre volume fraction can be determined mathematically in relation to the elastic modulus of the composite in the fibre direction of the unidirectional composite:

$$E = \left(1 - V_f\right)E_m + V_f E_m \tag{2-1}$$

Where: V_f is the fibre volume ratio, E_f is the elastic modulus of the fibres and E_m is the elastic modulus of the matrix. Fibre volume fraction is therefore one of the main parameters throughout this project.

Fibre volume fraction determines the fibre poor and fibre rich regions of the materials and can be the site of defects or differing mechanical properties.

2.1.1 Natural fibre reinforced polymers

With the target of a reduced environmental impact, material systems less based on petroleum products have been developed. These include common thermoplastic matrix materials such as polylactic acid (PLA), polypropylene (PP), polyethylene (PE) and polyvinyl chloride are considered more environmental friendly as functional materials. The most commonly used polymer matrices are PP and PE [15; 16; 37].

Naturally sourced fibre alternatives include sisal, jute, hemp, kenaf, flax, date palm and harakeke fibres are available [38; 39]. The most commonly used natural fibres are hemp and flax. Novel fibre such as harakeke fibres were used to create the alternatives [15].

In this thesis, main matrix material used was polylactic acid (PLA), which was easy to process and access, it had good chemical compatibility and commercial potential [40]. PLA is biodegradable as its monomer is typically made from lactic acid and lactic acid is usually made from fermented milk. PLA is therefore an appealing material as bio-based alternative to other samples.

PLA is a semi-crystalline polyester thermoplastic [41]. Like every other material, PLA has disadvantages; it is brittle under tensile loads unlike some semi-crystalline polyesters

[42]. Toughening is therefore significant for applications of PLA due to its brittleness [43]. PLA also has low impact resistance and commonly strengthened by reinforcing pure PLA with fibres; synthetic, manmade and natural fibres [16; 44; 45]. Synthetic fibres such as carbon fibres are commonly used for research and industrial products. Although the production of synthetic fibres is cheaper and less time consuming than natural fibres, these reinforcing materials do not provide a sustainable or biodegradable product.

Ductility of the PLA can be improved by blending with poly (butylene succinate), also known as PBS with varied weight ratio [46]. PLA yields in a plastic manner, by increasing the degrees of polymerization and crystallinity of PLA cause PLA to have great resistance to elastic deformation [47].

Natural fibres take longer to process but can be abundantly supplied, produced at a lower cost and preferably sustainable [35]. The properties of the natural fibre reinforced polymers (or natural fibre composites, NFC) are depended on fibres' type, properties and structure [45].

Harakeke reinforced composites is ultimately the goal material of this research project to test on. The reason being was that harakeke fibre is native to New Zealand and therefore locally resourced. It is locally sourced therefore has additional benefits from sustainability point of view. It is found that natural fibres showed promise in NFC [15]. Within this research, harakeke fibre is representative of an NFC in terms of the thermal properties and in relation to that, the results gathered focusing on this material may be more generally applied in manufacturing.

2.2 Additive manufacturing (AM) of polymers and composites

2.2.1 AM of polymers

Additive manufacturing (AM) permitted the fabrication of objects with high geometrical complexity at reduced fabrication time and cost [48].

Additive manufacturing (AM), also known as 3-dimentional (3D) printing, it has numerous methods; stereolithography (SLA), digital light processing (DLP), laminated object manufacturing (LOM), digital beam melting (EBM), fused deposition modelling and more [49]. Fused deposition modelling (FDM) is most commonly used method for fabricating polymer composites [1].

In FDM, thermoplastic filaments were melted and extruded through the machine's nozzle. The nozzle was controlled by a 3-axes system, which allowed the molten plastic to be deposited onto a print bed [25]. The nozzle can sometimes be blocked due to variety of the filaments and/or the feeding rate, which sometimes could be heated externally to run the filaments feeding process smoothly [50]. Thermoplastics used for FDM are usually amorphous polymers or those consisted low levels of crystallinity. This was due to the low degree of polymer shrinkage exhibited, which determined the accuracy of products [15]. The quality criteria of the final product were measured in terms of its strength, surface finish and porosity, which are tied to the process parameters of FDM production processes [10].

Acrylonitrile-butadiene-styrene (ABS) and polylactic (PLA) are the typical FDM materials used and both are commercially available [15]. With PLA, additive manufacturing (AM) may produce parts with individual constructional differences. Differences as such can sometimes be directly correlated to the defects in parts. Increase in the degradation rate and reduce the cost of PLA without compromising desired mechanical properties is challenging [51]. PLA has less flexibility when applied in 3D printing.

2.2.2 AM of composites

There are numerous advantages in using composite materials for AM, in which they offer high mechanical strength, high performance for specific functional needs or applications. Composites materials grew to be a major sector in aerospace industry due to the high strength and low weight properties [52].

Composite materials can be used to produce innovative, light weight and complex components in various industries such as aerospace, automotive, marine, nuclear and biomedical industries [49]. Lightweight composites such as metal composites and reinforced polymer composites are typically adopted in manufacturing industries. Fibre reinforced polymers for an example, they contribute to environmental sustainability, components fabrications in 3D printing methods [49]. 3D printing technology, FDM is generally performed on Iron/ABS, Copper/ABS, Polypropylene and other composites [1; 14; 53-55].

2.2.3 AM of NFC

AM with composites materials offer great compatibilities when fabricating parts and the functional needs of different industries were satisfied.

For successful productions, the matrix material and the reinforcing material must be biocompatible with each other; where the mechanical performance and biological interactions were major factors [56].

2.3 Review of non-destructive evaluations (NDE)

A range of non-destructive evaluations (NDE) were used to inspect composite materials, this include; ultrasonic testing (UT), radiographic testing (RT), thermographic testing, electromagnetic testing (ET), speckle shearing interferometry (Shearography), visual testing (VT or VI) and acoustic emission (AE) [52]. Based on the factors to be evaluated, there are two main categories of non-destructive tests, one was the estimation of physical and mechanical properties, the material defects detection in composites, and another was to determine the integrity of structural components manufactured from composites. Within the field of NDE, non-destructive (NDT) refers to the evaluation and inspection processes of samples for characterization and/or detect identifications without altering the properties of samples. These evaluations determine the manufacturability, performance and longevity of the composite materials [52].

Most of the published papers or books inspected on commercially available materials such as carbon, glass fibre reinforced composites or materials [57-66]. The remaining challenges of NDE of FDM are the lack of understanding in AM materials (including defects characterisation), insufficient standards for the mechanical testing and NDE of additively manufactured components. The types and the sizing of defects, sensitivity/detectability of the NDE techniques were investigated in some review papers [67]. NDE techniques such as IRT and ultrasonic testing can be used for in-situ process monitoring [67; 68].

2.3.1 Ultrasonic testing

Ultrasonic testing is commonly used in NDE. High frequency wave propagation was what UT based on. UT generate sound waves that will reflect in predictable ways off of (surface) defects such as cracks [69]. The waves were transmitted through the sample by a transducer. High frequency waves to not propagate through air, a couplant (i.e. water.) was therefore required for UT. Although there are three modes in UT; transmission, reflection and backscattering, transmission and reflection are the two main approaches used, in the case of echo or pulses [52]. There are different ways of receiving the wavefront: with a simple transducer, phased array ultrasonic (PA) or with time of flight diffraction ultrasonic (TOFD) [70]. UT enabled the three-dimensional (3D) mapping of the sample, where delamination or debonding were localised in depth with various colours, depending on the scale used. In pulse echo ultrasonic method for an example, this method detected defects in homogeneous materials. If defect detection location and for imaging purposes, quality control are more the concerns, ultrasonic pulse velocity measurements were then the suitable method [71]. The through transmission ultrasonic method is particularly beneficial when applied to complex geometries that do not permit the traditional transducer and receiver to be in contact with the sample surface [52]. Signal information may provide characteristics such as the location of cracks, defect's size and orientation [72]. It is found that ultrasonic methods enabled the determinations of defect depths/thickness, the presence of an inhomogeneous medium, the elasticity modulus of the sample [70]. Main advantages of UT would be its scanning speed, defect detection capabilities and good resolution in detection and analysis. Main disadvantages of UT would be the difficulty of its set up, required skills and insurance in scanning accuracy and testing. UT is prominent for repeated parts assembly.

2.3.2 Radiography

A varieties of radiography were developed throughout the years; film radiography, computed radiography, computed tomography and digital radiography [52]. Radiographic testing (RT) used x-rays or gamma rays for defects/flaws identifications [73; 74]. This techniques is used in various situations such as in weld quality, castings, structures and composites. Each type of radiographic testing has specific applications. Depending on the parts to be evaluated, conventional radiography is great when parts are not too thick nor too thin, i.e. when detecting large voids, inclusions, trans-laminar cracks, non-uniform fibre distribution and fibre misorientation such as fibre wrinkles (weld lines) [52]. Low voltage radiography is great for thicker components. Gamma rays can be used in low voltage radiography and it can also be employed in small matrix cracks detection and delamination of the sample [75]. A great example to radiography is x-ray computed tomography (XCT), in which the information of 3D geometries and properties of the solid were obtained. XCT can modify the observational scale for reliability; i.e. modified from macroscopic to microscopic [76]. However, the disadvantages of radiography may differ when applications were varied, high risk of radiation hazard, planar flaws (i.e. had to be aligned perpendicularly in relative to the inspection direction) can be missed when sensitive to defect orientation, limitations in thicknesses and fine cracks characterisations [52].

2.3.3 Thermography

Thermography is a common thermal imaging method used for NDE, where thermograms (digital thermal images) were to be produced for defect analysis and evaluations. The concept of thermography is based on the evaluations of thermal conductivity differences of a material when defects are present. Defects or anomalies of materials cause changes/fluctuations in observed thermal radiation, such changes were the focus of NDE. A large surface of a sector can be inspected without couple is the advantage of thermography. The disadvantage was that this method requires expensive instrumentation and possibly the limited depths. Thermography have almost no health risks, cover wider or full inspection field/areas and has the potential to be well suited to inspection of filaments. Therefore thermography is worth of investigating for multi-purposes.

2.3.4 Others

Depending on the types of defects, magnetism, electricity, mechanical vibration, laser optical method (Shearography testing) can be used to inspect materials.

2.4 Thermography

Human eyes are only able to view certain electromagnetic waves, known as visible lights and lights such as infrared and x-ray are therefore invisible to the naked eye. In order to see the displays of non-visible lights and extract information from the samples; specific equipment and sometimes, computational programmes are acquired to see lights that have more energy and shorter wavelengths. This technique is continuously developed to “see the unseen” [77; 78].

2.4.1 Background

In early applications IR detectors were very slow and prohibitively expensive for most industries. Recently IR camera technology has developed quickly, leading to a vast increase in accessibility to cameras [79].

Lower cost detectors have enabled a wider range of applications to be developed Thermal imaging techniques have been developed for industrial uses such as conducting aerial surveys of components, detecting defects in electrical components and medical screening and diagnostics [62; 80].

The use of imaging is advantageous over point measurement when used as an online monitoring technique as each pixel of the image can be used as a measurement point. The high spatial resolution can then be used for locating defects and observing abnormal heating phenomenon during quality assurance processes.

Speed and efficiency of quality assurance can be improved by increasing the rate of data acquisition and improvement of its accuracy. Such improvements were used to assist the ability of controlling and monitoring processes. Quality assurances of polymer composites materials remained challenging in terms of cost-effective and materials-wastage.

Feasibilities of thermography are therefore continuously investigated and studied.

2.4.2 Active Thermography

IR thermography are categorized into two approaches; active thermography and passive thermography. Passive thermography test samples and structures without external thermal excitation [81].

Active IR thermography requires an external heating source to the object of investigation, in which an internal heat transmission; thermal radiation and the transfer of energy by phase changes were to be collected and studied. Examples to active thermography are; pulse thermography (PT), lock-in thermography (LT) and pulsed phase thermography (PPT).

IR thermography's principle is based on Stefan-Boltzmann law. Theoretically, Stefan-Boltzmann law only applies to blackbodies, in which the subject's surfaces absorb all incident heat radiation/excitation. However, the perfect black bodies do not exist in nature and not all radiant energy can be absorbed. Stated by the law, where the total radiant heat power emitted from sample surface is proportional to fourth power of absolute temperature. The relation between the radiant emission and temperatures of interest is governed by Equation (2-2):

$$\mathrm{E} = \varepsilon\sigma T^4 \qquad (2\text{-}2)$$

Where E is the total electromagnetic radiation emitted from a blackbody with unit of W/m^2, ε is the emissivity of the specimen of interest, dimensionless, σ is the Stefan–Boltzmann's constant with units of W/$m^2 \cdot K^2$, and T is the absolute temperature in kelvin, K [82].

Thermal cameras provide visual inspection information in the IR range of the light spectrum [77]. There are two different types of IR detectors that are commonly used in thermography; photon detectors which operate in the mid-wavelength infrared range (wavelengths of 3-5 μm) and microbolometers which operate in the long-wavelength range (wavelengths of 8-14 μ) [83] [78].

Photon detectors have higher sensitivity and faster response time than microbolometers, [84]. This is because the photon detectors convert the incoming photons directly into an electrical signal, whereas the microbolometers are dependent on the conversion of incoming radiation into heat which impacts the electrical resistance [85]. There is then a cooling time required for the microbolometers that limits their recording rate. Thermal sensitivity defines the smallest temperature difference that the camera can detect [86]. However, photon detectors are ten times more expensive than microbolometers due to the materials that the photon detectors uses including semiconductor sensor materials (such as $InSb$)and their requirement of efficient cooling capability. Typically photon detectors have integrated miniature Stirling cooling systems that maintain sensor temperatures of ~ 70 K. [84; 87].

Higher spatial resolution is provided by a larger number of pixels across the same observed area, i.e. field of view (FOV). Each pixel is a reading from an independent sensors within the camera, therefor more pixels means a larger sensor array within the camera. For a fixed FOV, a higher thermal resolution means smaller temperature changes can be resolved. Thermal resolution is dependent on the sensor type.

IRT is commonly used to monitor the damage of the aerospace components. Materials damage can happen at any stage of the component's cycle life, throughout manufacturing, in-service and maintenance operations [88; 89]. Most recent studies recognised the potential of IRT in evaluating elastic deformation and fracture mechanics in nanomaterials [90].

Observations of surface temperatures distribution/fluctuations carried out non-destructively within infrared thermography, in which the local infrared (IR) emission emitted from the surface of material was collected, processed and analysed.

2.4.3 Pulsed Thermography (PT)

Pulsed thermography is a type of active thermography where a short and high-power thermal pulse is applied to the surface of the object under inspection. An infrared camera is then used to monitor the surface of the object.

There are various configurations of pulsed thermography, which are point inspection, line inspection and surface inspection. Point inspection is when a focused light beam is used for heating. Line inspection is when heating stimulus such as air jets, scanning laser, heated wire and line lamps are used. Surface inspection is when heating stimulus such as camera flash is used.

Defects are detected when thermal contrast is revealed due to the thermal conductivity differences. When defects are present, heat conduction can be blocked by subsurface defects, which were parallel to the surface. A reduction in cooling rate of surface occurs and the thermal contrast can then be revealed by IR camera [63]. This is because the heat diffusion process is influenced by depths and irregularities of material. Thermal response can be quantitatively analysed after data collection, where thermal contrast of the response was produced for analysis. The absolute thermal contrast was the surface temperature difference between the defective regions and non-defective regions [91].

Thermal imaging varies in individual cases. Influential factors on the accuracy of digital infrared thermograms (thermal images) can vary due to the mass of the intended specimen, i.e. depth and properties of internal structure of the specimen. Thermal conductivity is depended on the heat flow rate (heat flux), and heat flux is the flow of energy per unit of area per unit of time. The rate of conduction through the sample varies with thickness and composition of the material(s).

$$\mathrm{K} = \frac{Q \times L}{A \times \Delta T} \tag{2-3}$$

Where Q is the amount of heat transferred through the sample samples, L is the thickness of the material, A is the area of thermal conductivity and ΔT is the temperature difference across [92].

In PT, the raw data collected were the digital data (digital level data or DL data) in a sequence of images through time, where a calibration is needed to convert DL readings into thermal data for data evaluations. The data acquisition is fast and allows inspections of larger surfaces [93].

However, PT is only to be considered when applied to near-surface defects and limited by the long established "rule of thumb" that the defect aspect ratio must exceeds two. The defect aspect ratio was varied with the defect diameter and defect depth [63].

Pulsed Phase Thermography (PPT)

PPT is pulse-heated as in PT, it analyses the multiple frequencies that make up square wave heat pulse. These frequencies are processed by performing Fourier transform of temperature evolution over the thermographic camera's field of view [26].

Using FT it is then possible to use the real and imaginary components provided to assess the magnitude and phase data. Within PPT the phase data is of most interest as it revealed deeper subsurface probing (as in modulated thermography) and no need of background knowledge about the position of non-defect points in images, as oppose to PT images [94] [95].

FFT of each vector was used to produce phase, amplitude and average images for the frequency components selected, this was governed by;

$$F_n = \sum_{k=0}^{N-1} T(k) e^{2\pi ikn/N} = Re_n + ilm_n \tag{2-4}$$

Where N is the number of images processed, n is the frequency increment, T(k) is the temperature at two-dimensional (2D) coordinate (x,y), for thermal image k [21].

In order to determine the magnitude of phase data from real and imaginary components of FFT, the following equations were used to determine A_n, the amplitude and φ_n, phase data.

$$A_n = \sqrt{Re^2 + ilm^2} \tag{2-5}$$

$$\varphi_n = tan^{-1}\frac{lm_n}{Re_n} \tag{2-6}$$

The data was converted from temporal evolution of temperature of a single pixel to phase evolution of frequency of a single pixel. FFT was applied on each vector to produce real and imaginary components of the n frequencies. Phase images are the focal point of PPT [21].

Phase values of each pixel at each frequency were calculated for further analysis. Phase images were images that mapped the delay of thermal response (thermal wave that consisted of phase delay data) of the sample, which shows the thermal features that were not visible to eyes. Phase data is commonly analysed due to its better tolerance to non-uniformities and environmental reflections [93]. Energy excitation for PPT is either long pulsed energy or short pulsed energy. Short pulsed energy is preferred in this research project as the greater contrast (between the defect and non-defect areas) can be analysed in a short period of time. Phase contrast is governed by:

$$\Delta\emptyset = \emptyset_d - \emptyset_s \tag{2-7}$$

Where $\emptyset_d$ is the defect area and $\emptyset_s$ is the sound area (non-defect area).

This is ideal when analysing thermal response of object of low conductivity, polymer for an example. The technique is appropriate for detection and imaging of near surface, in-plane, defects such as delamination and adhesion defects between layers of coatings and their substrates [96].

The raw PT data however, is challenging for analysis. This is mainly caused by non-uniform heating. PPT is a data processing methods included in PT. PPT retrieves the phase and amplitude values from PT process, in which it implemented that PPT is a combination of lock-in thermography (LT) and PT [93]. PT is good for near-surface analysis, whereas PPT is better at subsurface analysis. The subsurface discontinuities affect the heat diffusion process and create abnormal temperature patterns at the surface that the IR camera detects [93]. This allows the defect depths to be quantified.

Thermal diffusion length (μ) is used to fit the data analysis and estimate the defect depth (z), which are governed by equation;

$$z = C_1 \sqrt{\frac{\alpha}{\pi \times f_b}} = C_1 \mu \tag{2-8}$$

Where: μ is the thermal diffusion length, α is the thermal diffusivity of the sample, f_b is the blind frequency (the frequency that the defect is distinguishable) and C_1 is the empirical constant observed for specific experiment.

There are various ways of measuring the surface temperature of the samples, infrared photography was used as the surface temperature mapping technique for turbine cooling investigations [97].

Surface temperature profiling can be evaluated with laser ultrasonic method. The laser ultrasonic method is used to measure the surface temperature distributions of the aluminium plate after the plate is single sided heated up to 110 ℃. The temperature value that the metal was heated up to was estimated by the inverse analysis associated with the surface acoustic wave (SAW) measurements. Signal-to-noise (SNR) was also a factor that impacted the small deviation in transit time of the experiment [98].

2.4.4 Heating stimulus

Different types of thermography techniques are recorded to have various types of heating stimulus. Heating stimulus provides sufficient thermal energy to allow the heat propagate through the sample, which was applied onto specimen-material for inspection. The resulted thermal response was then used for defect analysis.

Heating stimuli can be used in pulsed thermography are; halogen lamp, laser and ultrasonic laser. Other types of heating stimulus such as laser ultrasonic method, another method used for measuring the surface temperature distributions [99]. Hot air that constantly provided for samples will not heat up the material instantly but it provides a condition that is uniform heated once the intended temperature is reached [100].

Theoretically, the ideal type of heating stimulus is when heating is uniformly distributed across the surfaces of samples. Preferably quick and sharp excitation without altering samples' properties. Distribution of surface temperature is generally used to examine the structural damage or the behaviour of subsurface. Heating power is therefore selected according to the scale and the type of the experimental setup. Intended samples are biodegradable samples that can melt if the power is higher than its limit.

Heating may be applied by using a single or multiple heat sources depending on the area and amount of thermal stimulus required. Such heat sources include photographic camera flashes [101], halogen lights [93], hot air jets [102]. Photographic camera flashes are the available heating stimuli for this research project.

In order to have heating stimulus that is as uniform as possible. Two or more camera flashes with same power can be used to raise the temperature, which in turn the better thermal contrast or the absolute will theoretically be observed. Transmission and Reflection modes are the two main setups of current thermography. In transmission mode, the heating stimuli and the IR camera are positioned on the opposite sides of the sample, whereas in reflection mode, the two are positioned on the same side of the sample. Transmission is theoretically good for small and single artificial defect.

2.5 Data processing

2.5.1 Introduction

Online inspections aimed to provide benefits to various industry sectors by increasing the efficiency, improving the speed of 3D printing production processes and by reducing the wastage of the samples. Studies and/or researches of signal data processing are therefore and can be highly rewarding as the results.

Online inspection are closely tied to signal data processing methodologies, which is; thermal response was recorded due to the brief external temperature change. Transient regions of the temperature to depth is the focus of thermography. In nature for an example, there are transient disturbances to the temperature-depth profile, which is created when the climatic temperature changes propagate downwards from the ground surface to the subsurface.

Thermal reflection is a common source of issues when interpreting infrared thermal images. Smooth surfaces, wet surfaces, transparent plastics or metals may give rise to reflections of infrared radiation from often unintended influences [103].

2.5.2 Processing Techniques

Different online imaging processing tools are being continuously developed and tested since the beginning of thermography in 1960s. Depending on the type of the images or data involved, several of data processing techniques can be used. Random error such as temporal noise may occur. This was due to the fact that random noises arise independently from image to image, images as in thermograms.

Thermal signal reconstruction (TSR) method is the data processing technique that commonly used for thermal images. Although factors such as the accuracy of temperature profiling of IR camera and the mass of the specimen samples can affect the resulting thermal images or the thermograms (thermal images), computational processing plays an important role in modern thermography techniques.

TSR is an computational program that interprets decomposition of thermograms on a logarithmic polynomial basis, in which the use of the logarithmic derivatives were used to deduce the noise of the raw data and the imaging quality is therefore enhanced in terms of clarity or better thermal contrast [104].

2.6 Thermography applied to NFC samples

Throughout the years, there are different ways of providing heat to the samples intended for experiments. However the heating stimulus is selected depending on the type and the nature of the samples.

Impulse thermography technique can also use halogen lamps as its heating source to detect defects in concrete structural components. These components were not exposed directly to sunlight nor affected significantly by the surrounding wind.

High humidity and ambient temperature enabled the active thermography results with better thermal contrast. In addition, the greater the absolute contrast between the defect and sound (non-defect) areas is caused by the increase in ambient temperature and at a faster rate with large and shallow delamination in comparison to small and deep delamination [105].

Properties of samples that affect the way that the observations, each varies differently and some may not contribute significant changes or fundamental changes to the thermal imaging results and associated signal processing. Thermal properties such as emissivity, diffusivity and conductivity are the main concerns of this project. Diffusivity as an example, rock has low thermal diffusivity and this stores the heat inside its internal body for a little bit longer and laser will burn natural fibre reinforced composites as a result.

Camera flash is therefore one of the commonly used heating stimulus in thermography. Its advantage been that it has just enough power to heat up the natural fibre reinforced composites quickly without changing the material's properties.

Chapter 3

Methodologies

3.1 Introduction

The main goal of this research project was to detect defects and thermal irregularities of samples without damaging or altering the materials' properties. The developed inspection techniques were in hope to be used as a routine inspection in quality control.

In this study, IR thermography was used for this purpose (non-destructive testing). Samples with artificial defects were manufactured with increasing complexity, so defects inspected varied in size, shape, texture and type. Experimental work was ordered by increasing difficulty. The end goal of this project was to inspect 3D printing harakeke reinforced polymers filaments with IR thermography. Sample development is discussed in Section 3.3.

Data was processed and analysed by customised Matlab scripts. Raw data recordings were first collected, providing thermal images (thermograms) and thermal data was then processed into phase data. Both thermal data and phase data are analysed, as discussed in section 3.4.

3.2 Equipment

IR thermography required an external heat source to heat up the sample, an IR camera to record thermal response of the surfaces of samples, a PC with Matlab to collect and process the digital signals recorded, and a mounting frame for equipment positioning.

Infrared (IR) camera:

An Optris IR camera was used for collection of thermal response on the surface of the samples'. The frame rate (or recording frequency) of the IR camera was set at 32Hz. Further camera specification is given in Table 3.1 [106].

Table 3.1 Technical details of Optris Infrared Camera PI 640 [107].

Optris PI 640. Part number: OPTPI640O33T900	Specifications
Optical Resolution	640 x 480 pixel
Spectral Range	$7.5 – 13 \times 10^{-6}$m
Frame Rate	32Hz
Thermal Sensitivity (NETD) / Thermal Resolution	75×10^{-3}K
Operational humidity range	20 – 80%, non-condensing
Accuracy	± 2 degrees
Optic	33° x 25° lens, f = 0.0178 m
Operational temperature range	up to 1173.2K, 3 field selectable ranges

Heat source:

Cannon 430EX III flashes were used as the external heating source. Dimensions of a camera flash were 70.5 x 113.8 x 98.2 mm [108]. Each camera flash had an auto power off feature which turned off feature which turned off the flash, at an interval of approximately 90 seconds. This function saved battery power. Two remotes were wirelessly paired with the camera flashes and manually controlled to turn camera flashes on and off simultaneously. Four AA/LR6 alkaline batteries were used for each camera flash.

A receiver was paired with each flash. . The receiver was used to connect with a Viltrox FC-240 TX wireless flash trigger (remote). Two camera flashes were used in reflection mode and one camera flash was used in transmission mode.

3.3 Samples and sample preparations

Preliminary tests on samples with artificial defects of various sizes and types was carried out. The samples tested were ordered by increasing complexity, progressing from single to multiple materials and reducing severity of defect. The samples were tested in order of: Poly (methyl methacrylate) (PMMA) plate with flat bottom holes, notched PLA filaments, PLA filaments mixed with NaCl particles, PLA filaments mixed with untreated harakeke fibres and PLA or PP filaments reinforced by treated harakeke fibres.

All samples were spray-painted matt black before IR data collection to provide high and uniform emissivity.

The main matrix material used was polylactic acid (PLA, Natureworks, Ingeo™ 2003D grade) purchased from Clariant New Zealand Limited. PLA pallets were heated and hot extruded into filaments. By order of defect-detection difficulty, different samples were inspected (Table 3.2).

Table 3.2. List of samples with various defects

Order Number	Matrix Material	Defect Type	Approximate defect size (m)	Defect Depth range (m)
1	**PMMA**	**Artificial-Flat-bottom cylindrical holes**	$\mathbf{5.00 \times 10^{-3}}$	$\mathbf{0.50 \times 10^{-3}}$– $\mathbf{2.00 \times 10^{-3}}$
2	**PLA**	**Square notched defect on non-flat surface**	$\mathbf{2.50 \times 10^{-3}}$	$\mathbf{1.15 \times 10^{-3}}$ – $\mathbf{1.75 \times 10^{-3}}$
3	**PLA**	**Large NaCl particle defects within filaments**	$\mathbf{10.66 \times 10^{-3}}$ - $\mathbf{32.44 \times 10^{-3}}$	$\mathbf{0.00 \times 10^{-3}}$ – $\mathbf{1.90 \times 10^{-3}}$
4	**PLA**	**Coarse and unpulped Harakeke fibres**	$\mathbf{200 \times 10^{-6}}$	$\mathbf{0.00 \times 10^{-3}}$ – $\mathbf{2.00 \times 10^{-3}}$
5	**PLA**	**Treated and processed fine Harakeke fibres [25]**	$\mathbf{12.3 \times 10^{-6}}$	$\mathbf{0.00 \times 10^{-3}}$ – $\mathbf{2.90 \times 10^{-3}}$
6	**PP**	**Treated and processed fine Harakeke fibres [15]**	**Fibre bundle length:** $\mathbf{0.2 \times 10^{-3}}$, **with maximum length of 8** $\mathbf{\times 10^{-3}}$	$\mathbf{0.00 \times 10^{-3}}$ – $\mathbf{2.90 \times 10^{-3}}$

All samples were manufactured in the engineering workshop of University of Waikato.

The easiest defects to detect were flat-surface-defects milled on a PMMA plate [26]. This sample was developed for initial development and validation of the data collection and processing procedures [59].

Pure PLA filaments were made by hot extruding pure PLA A single notch was milled into a series of cut PLA filaments had for defect depth evaluation, , these samples are known as ‘Single Notched PLA filaments’. Notched filaments were used to inspect the defect depth detection limit of the developed IR thermography technique.

All samples were kept dry in sealed bag between data collection to prevent moisture causing inconsistencies in the result.

The next set of samples to be inspected was the NaCl (salt) particles mixed PLA filaments. With salt particles varied in size, large particles that were visible to the naked eye and easy to detect.

The next type of samples were coarse harakeke fibres mixed with PLA filaments. A small and controlled amount of Harakeke fibres were added into pure PLA to check if these larger distinct fibres would be detectable. . Those coarse and unpulped harakeke fibres were and to PLA at 0.125wt% and 0.500wt%. These samples were inspected with the coarse being of similar size to potential detects which could cause problems with 3D printing, e.g. fibre bundles, bunching, or clumps , fibre rich/fibre poor regions and other defective regions. The collected results were to be used as thermally representative materials (with larger defects) to the most challenging samples of this study.

PLA reinforced with 10wt% treated harakeke fibres and PP reinforced with 30wt% treated harakeke were the final set of samples to be inspected. These filaments were provided from a previous project [15; 25]. Defect detection and inspection in polymers reinforced by treated harakeke fibres were most challenging. This was because the size of the treated harakeke fibres were at least ten times smaller than the untreated harakeke fibres. PLA filaments reinforced with 10 wt% harakeke fibres and PP with 30 wt% Harakeke fibres were the material of interest, used for 3D printing.

Microscopic imaging of samples and defects:

Scanning electronic microscope (SEM, model: Hitachi S-4700 scanning electron microscope) and optical microscope (model: Olympus Microscope BX53) were used. SEM images were collected to visualise the physical appearances of a single fibre, fibre bundle, possible voids and other possible defects.

The cross-sectional areas of the samples were fractured with liquid nitrogen and kept dry. The samples were then attached with carbon tape to the cylindrical sample holder for images collection with SEM.

3.3.1 Polymethyl methacrylate (PMMA) plate

Fabrication of Material:

PMMA plate had overall dimensions of 210x297x6mm. PMMA plate was custom-made in the engineering workshop, where seven defects consisted of defect depths of 0.50, 0.75, 1.00, 1.25, 1.50, 1.75, 2.00 mm were milled on respectively. Each of these artificial defects had diameter of 5.00 mm and custom-made with Bridgeport milling machine. The thinnest defect depth attempted was 0.25mm and this can either be too thin to stay attached to the rest of the material or it will distort the material itself.

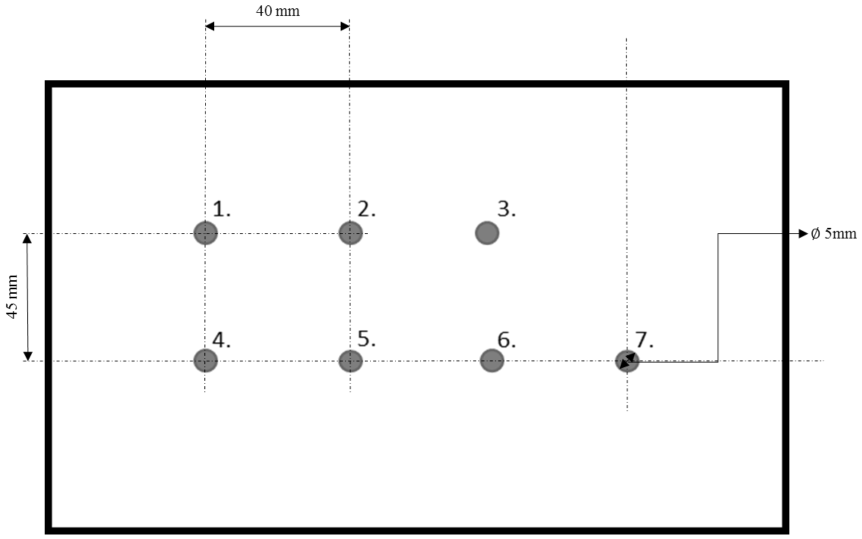

Figure 3.1. Diagram of PMMA plate with seven defects of various defect depths.

PMMA plate and the base plate were clamped on and levelled prior to milling. CNC milling machine was used to mill the FBH, which was controlled by a pre-programmed Solid-works. CNC machine was cooled with water that was mixed with water soluble oil. This helped to lubricate throughout the milling process and prevented the machine from rusting.

This was the most accurate set of the defects, where; variables that affect the finishing surfaces of the flat bottom defects were reduced to the minimum. The accuracy of the defect depths were measured and operated robotically from the programme.

3.3.2 Notched PLA filaments

Fabrication of material:

Controlled defects were made onto the flat surfaces of the PMMA in part I. For the aim of detecting smaller defects in filaments the curved surfaces were more challenging for IR analysis. Filaments as such were more true to end-goal samples, as the Harakeke reinforced PLA were in curved shape.

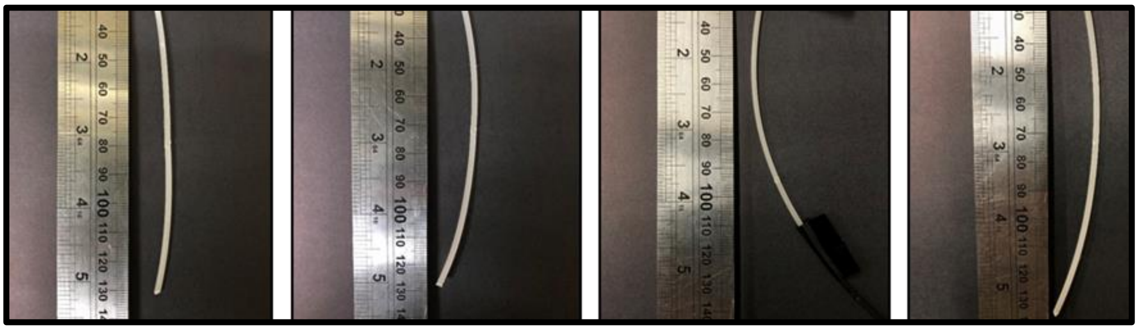

Figure 3.2. Transparent (original) filaments with a single notch on each, where A had defect depth of 1.15mm, B had defect depth of 1.35 mm, C had defect depth of 1.55mm and D had defect depth of 1.75mm.

The notch was milled onto each filament, each notch had the same length but different depths. The locations and depths of defects were controlled through the operation of Bridgeport milling machine. Filaments notched by Bridgeport milling machine were manually controlled in two dimensions, along x and y axes. A profile diagram of defect depth, width and thickness is shown (Figure 3.3).

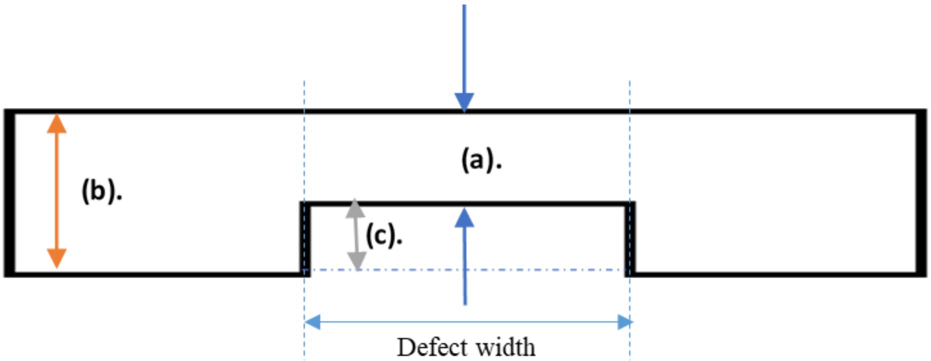

Figure 3.3. Profile diagram of a notched PLA filament. (a). Defect depth, (b). Sample thickness, (c). The notch depth.

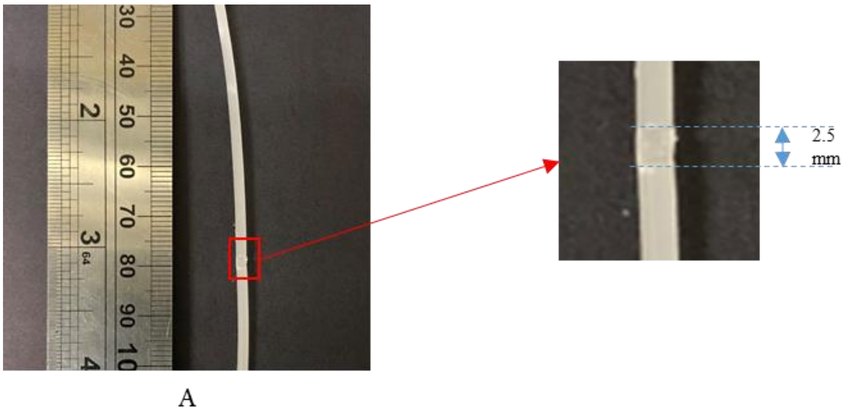

Figure 3.4. A close up of the notched section in sample A, with defect depth of 1.15 mm and width of 2.5 mm.

Notches consisted of different depths while each had the same width (2.5 mm). Four different pure PLA filaments were inspected and analysed. The notches were milled onto filaments, where defect depths were; 1.15 mm, 1.35 mm, 1.55 mm and 1.75 mm respectively. In addition, filaments selected for notching were a group of pure PLA filaments with similar diameters, where the average diameter of filaments was 2.5 ± 0.6 mm.

Each filament had one notch milled onto its surface. Matt black spray paint was applied to the filaments before IR inspection and data was processed as will be described in section 3.5.

3.3.3 PLA filaments mixed with NaCl (salt) particles

Fabrication of samples:

Different weight percentages of NaCl particles were mixed within pure PLA. The mixtures were hot extruded into filaments, where the same PLA pallets were used for the extrusion process: Ingeo Biopolymer 2003D PLA pellets and 2wt% and 5wt% of NaCl particles were mixed and extruded into filaments. PLA filaments with Sodium Chloride particles were examined to determine if defects of their size could be detected with this technique.

IR thermography and signal data processing of 2wt% NaCl mixed PLA filament were carried out prior to the size verification of salt particles.

An indication of the size range of the NaCl particles was determined by using a Stimulating Thermal Analysis (STA) instrument (PerkinElmer, STA8000) to burn off the PLA from around the salt particles. A filament sample was measured to be approximately 64 mg and combusted to 700℃ with a ramp rate of 15℃ per minute. The filament was then held at 700℃ for 30 minutes under a flow of air at rate of 40 ml per minute. The particles were then observed under an optical microscope. The lengths and widths of the salt particles ranged from 10.66 to 32.44 μm, as shown in Figure 3.5.

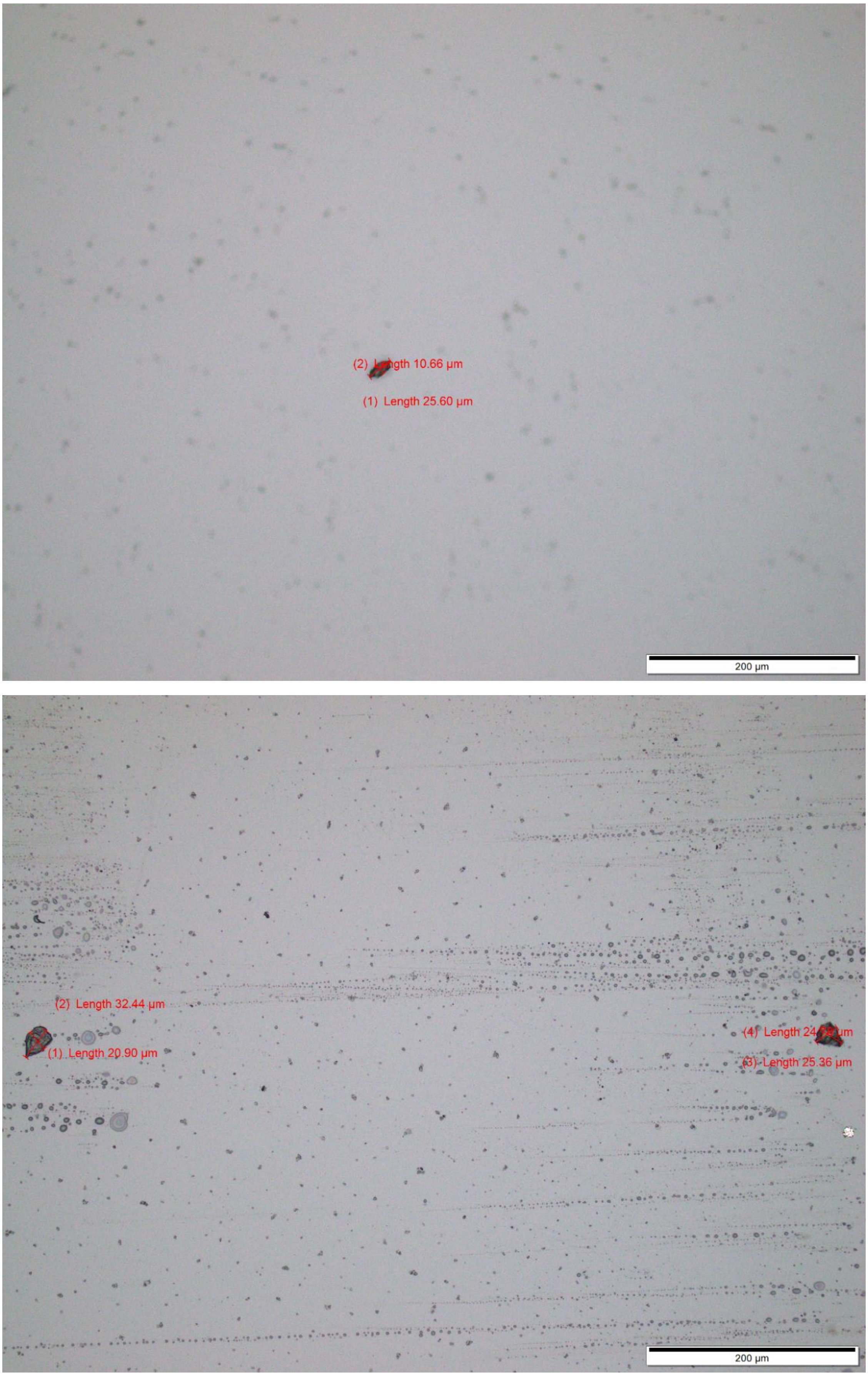

Figure 3.5. NaCl (salt) particles in different sizes, observed under optical microscope.

3.3.4 PLA mixed with coarse harakeke fibres

Fabrication of samples:

Fibres were stripped and srutched from harakeke, obtained from the Foxton Flax Stripping Museum. Prior to the compounding and extrusion processes, the coarse fibres were granulated and oven dried at 95℃ for > 16 hours. After granulation, coarse fibres were mixed with PLA pellets (Natureworks, Ingeo™ 2003D grade, purchased from Clariant New Zealand Limited). The mixture was then ready for hot extrusion. Small amount of course (non-pulped) natural fibre added into the hot-extruded pure PLA to simulate defects.

Extrusion of the mixture into filament was performed on a Labtech LTE20 Scientific 20 mm co-rotating twin screw extruder with all the heating zones set to 180 °C, except the feed zone set to 45 °Cand the die end set to 90 °C. A screw speed of 40 rpm was used and the filament was drawn from 3mm dies to an average diameter of approximately 2 mm.

The coarse and unpulped harakeke fibres were added at 0.125wt% and 0.500wt% to PLA and hot extruded into filaments. These were used in the experiment to see if IR thermography can be used to distinguish fibres from the PLA matrix. Coarse unpulped fibres were used as they have a larger diameter than pulped fibres, and also coarse fibres were of a similar size to fibre clumps which are the ultimate defect of interest as they cause blockages in 3D printer nozzles.

Untreated fibres were observed under scanning electron microscope (SEM), as shown in Figure 3.6, Figure 3.7 and Figure 3.8.

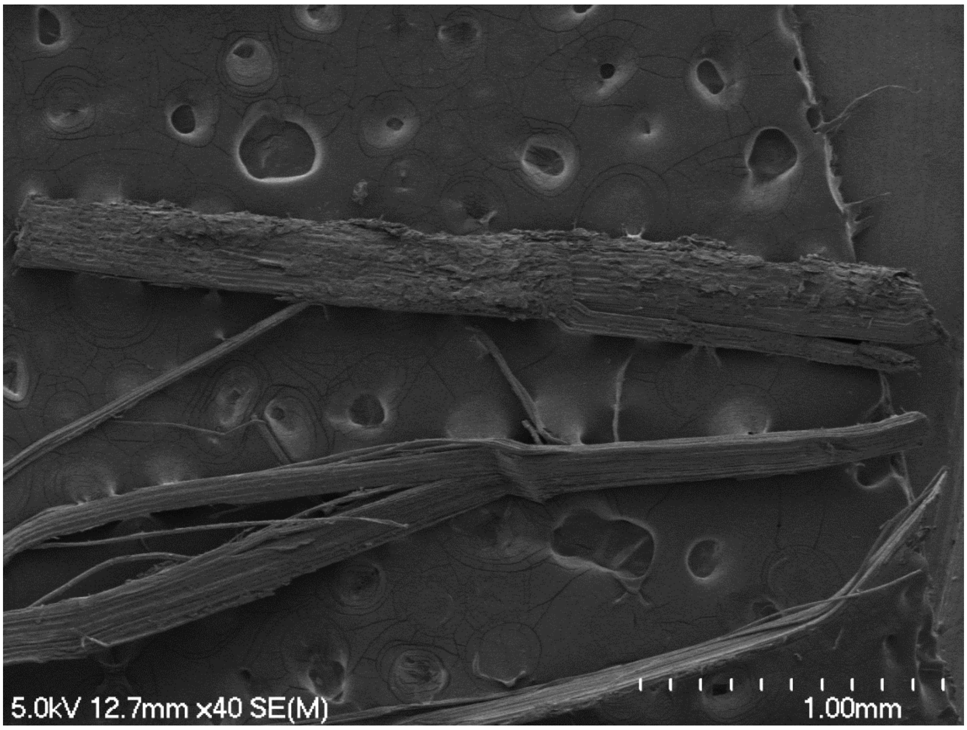

Figure 3.6. SEM image of the untreated harakeke fibres, under magnification of 40x.

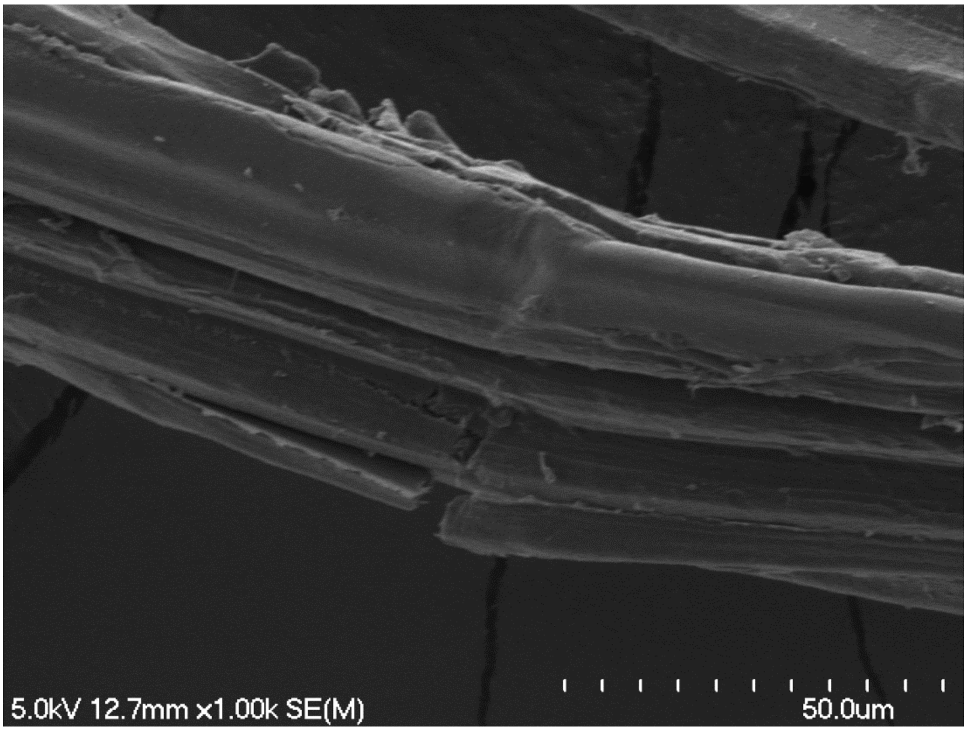

Figure 3.7. SEM image of the untreated harakeke fibres, under magnification of 1000x.

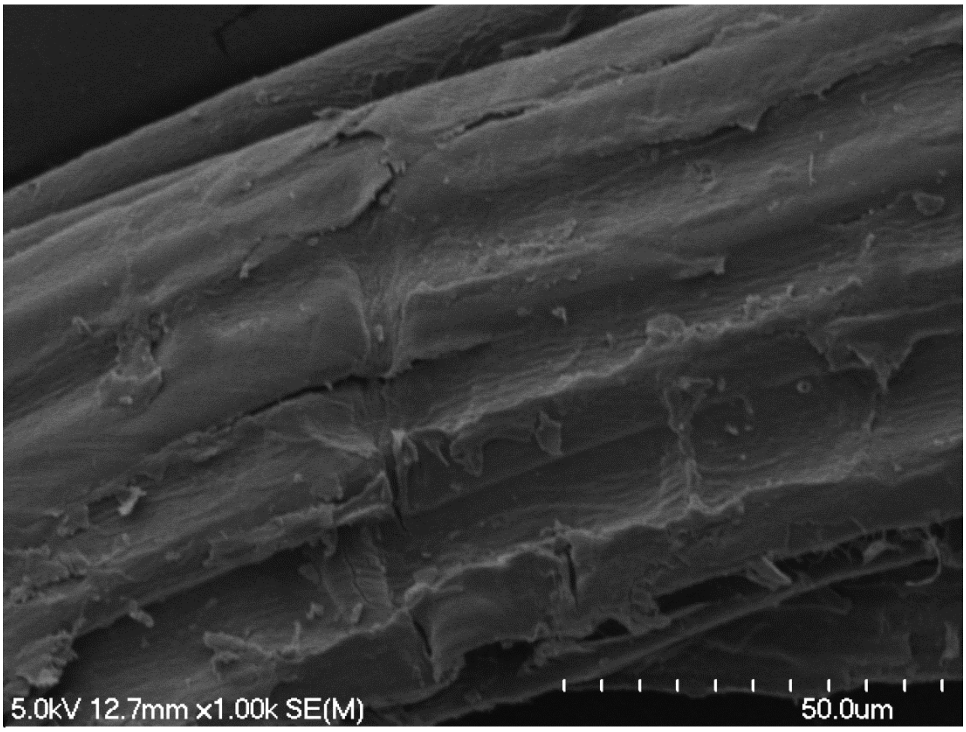

Figure 3.8. SEM image of the untreated harakeke fibres, under magnification of 1000x.

Untreated harakeke fibres inspected in SEM had diameters of up to 300 microns across. These represent defects which would be similar in size to fibre bunches/clumps are expected to cause nozzle blockage issues on 3D printer.

3.3.5 Polymers reinforced by harakeke fibres

Fabrication of samples:

10wt% harakeke reinforced PLA and 30wt% Harakeke reinforced PP filaments were produced in a previous project and provided by the School of Engineering [15; 25].

The full fabrication details can be found in reference papers [15; 25]. Harakeke fibres were mechanically separated, air dried and supplied in bundle by the Templeton Flax Mill (Riverton, New Zealand) in 2014. Fibres were chopped and fed into a Castin laboratory scale granulator using an eight mm sieve. Treatment solution used for harakeke fibres were 5% NaOH and 2% sodium sulphite. The steel canister was then held in the laboratory scale digester at 170°C for 40 minutes. Fibres were later removed from canister once digestion was completed. The fibres were then washed thoroughly with cool tap water before oven (air) dried at 103°C for 48 h. The average diameter was measured to be $12.3 \pm 1.7\ \mu$m. PLA3052D powder supplied by Nature Works LLC (Minnetonka, MN, USA) was used kept in an oven at 85°C for 48 hours prior to its use in composites. An intensive mixer was then used to mix the matrix material (PLA) and the treated fibres, the mixture was mixed in small batches at 185°C. The composites were solidified prior to its granulation. The granules were then hot extruded by ThermoPrism TSE-16-TC twin screw extruder with a 3-mm diameter die. Barrel temperatures of 183, 180, 174, 152 and 159 °C were maintained from outlet to inlet. The filaments were then consistently produced with assistance of an electric spooling machine [25].

The production process of 30wt% Harakeke reinforced PP had few differences to10wt% harakeke reinforced PLA. Solution to fibre ratio, matrix material and oven dried at 105°C for > 24 h. A Granulator was used to separate the dried fibre clusters prior to the composite fabrication [15].

SEM images were to confirm the distribution of harakeke fibres within the polymers, as shown in Figure 3.9 and Figure 3.10.

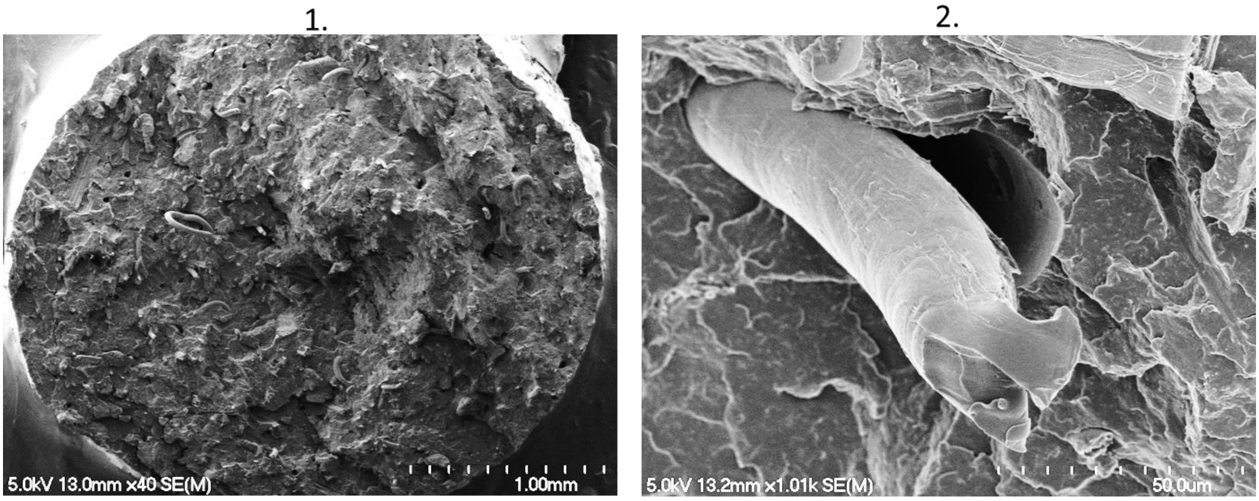

Figure 3.9. 10wt% Harakeke mixed with PLA: 1. an overview of the cross-sectional area of the filament, 2. a magnified image of a treated harakeke fibres.

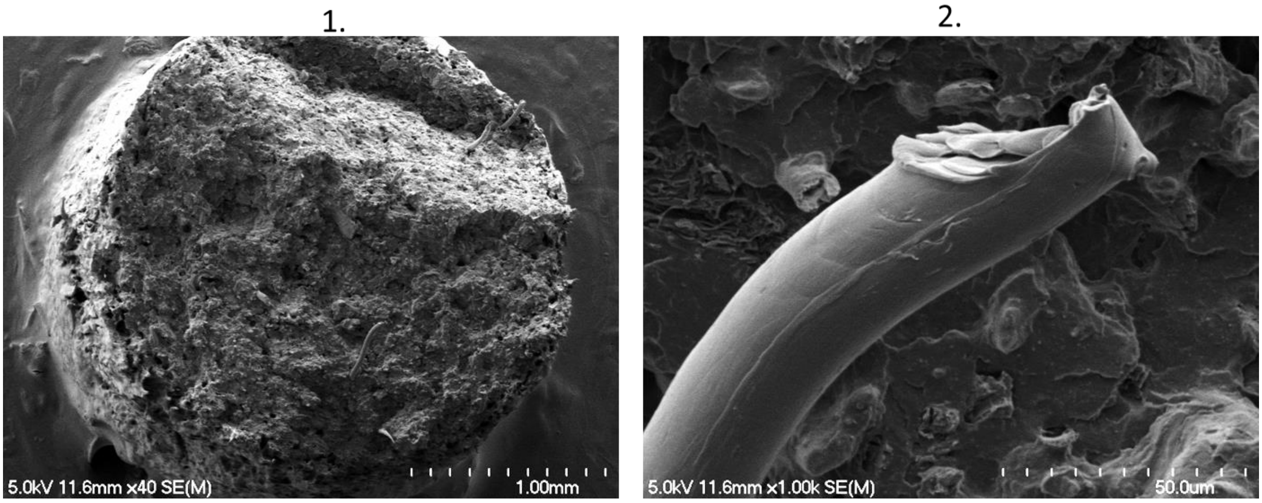

Figure 3.10. 30wt% Harakeke mixed with PLA: 1. an overview of the cross-sectional area of the filament, 2. a magnified image of a treated harakeke fibres.

3.4 Experimental setup

3.4.1 General setup

In thermal imaging, uniformity of the heating distribution was the main concern of the experiments. Increased post-processing due to unintentional noise can influence the observational quality.

Overall, in reflection mode, two camera flashes were used as the heating stimulus, which were positioned at left and right hand sides of the IR camera. Each camera flash was positioned as close as possible and at an angle of 45° to the table of setup, as shown in Figure 3.11. camera flashes and the IR camera were aligned with each other to ensure that both flash light were equally emitted from 45° and intersected at the intended field of view (FOV).

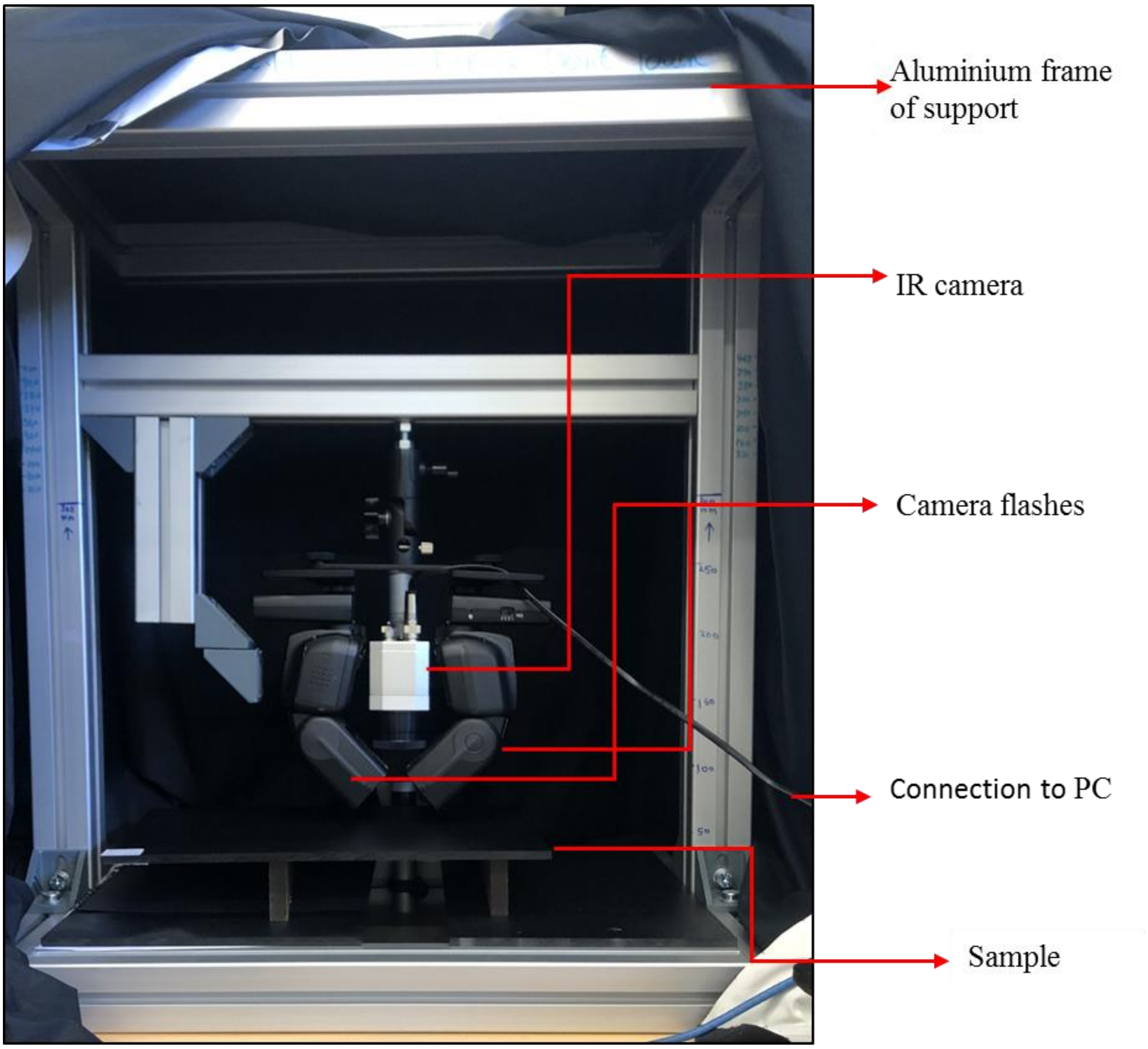

Figure 3.11. Experimental setup for pulsed phase thermographic inspections, in reflection mode.

The setup consisted of a custom made aluminium frame, an IR camera, a camera flash, sample and a PC. The custom made aluminium frame was used to support the setup, camera stands and the matt black fabric cover. Observations and data collections were carried out in a dark and enclosed environment. This was to prevent the visible light (or other radiations) from interfering with the infrared wavelengths collections.

This setup was improved as the camera flashes and the IR camera were held at a fixated position while levelled on the horizontal plane.

When changing between different samples, the heights of the IR camera and camera flashes were adjusted with improved flexibilities. Curved samples such as filaments were held onto a sample holder. The sample holder was custom made and it secured filament and aligned the filament linearly, keeping it levelled and was more stable.

Spatial resolution is the geometric size on the surface of the sample that each pixel represents. Stand-off distance measures the distance between the IR camera and the sample observed. Stand-off distance may be varied based on the size of the sample of interest. Pixel resolution was calculated for each set-up. As a demonstration; for a standoff distance of 98.5mm, 300 pixels images a length of 21 mm on the sample, hence 1 pixel is 20/300 = 0.0667mm in this direction. This method was used for approximating the size of features seen throughout the results.

Inspections of the same sample were conducted in both transmission and reflection mode, which were different in terms of the number of the camera flashes use, the position of the camera flash and the processing difference introduced in section 3.5.

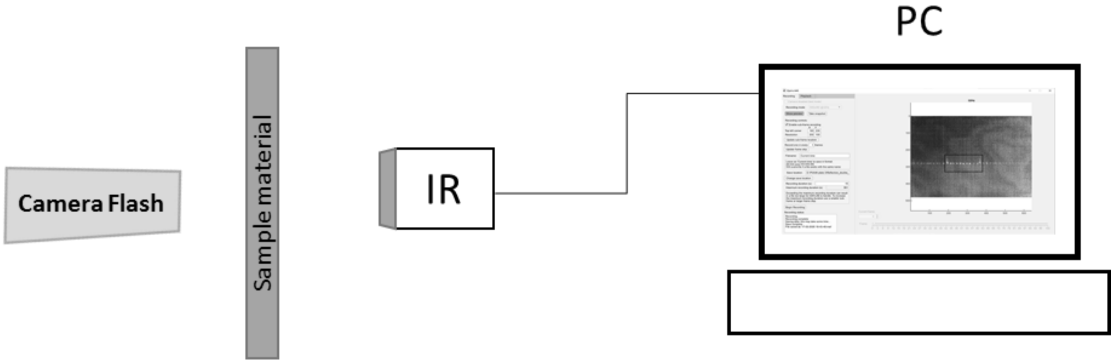

Figure 3.12. Schematic diagram of setup in transmission mode.

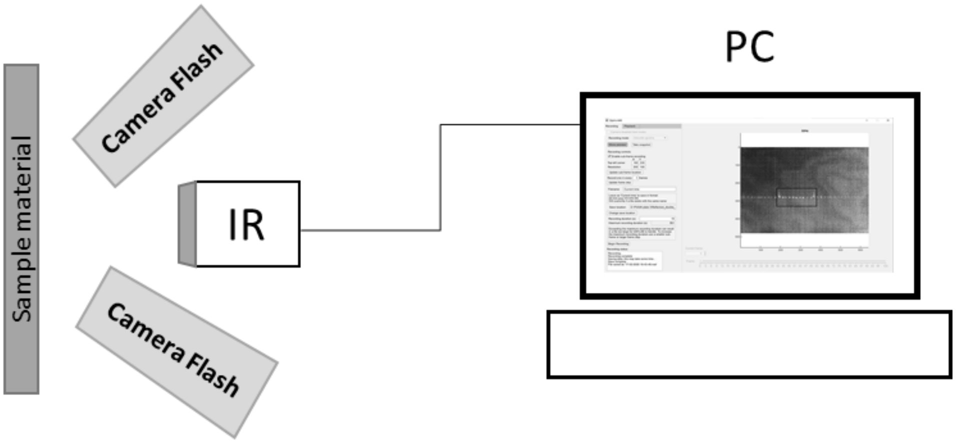

Figure 3.13. Schematic diagram of setup in reflection mode.

Depending on the time periods selected for recording, if the recording time period was too short, it may not capture the entire thermal decay back to room temperature, which led to a reduction in phase contrast [21].

3.4.2 FBH on PMMA plate

Equipment and experimental setups:

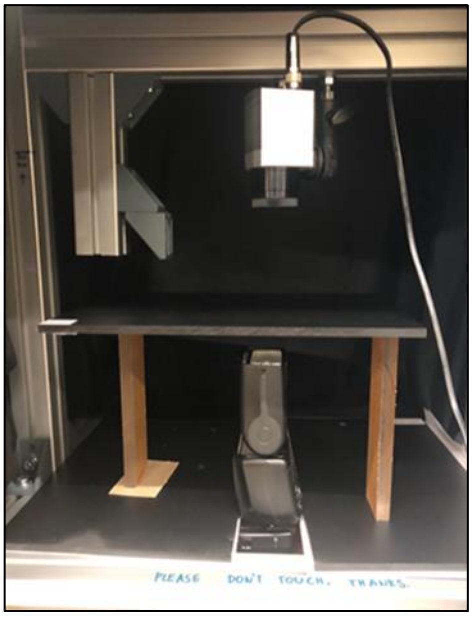

Figure 3.14. Setup of PMMA plate in transmission mode.

Transmission Mode: on the left-hand side, it is the overall set-up without the matt black fabric and on the right-hand side, the fabric cover is on top of the Al-metal-frame, where partial fabric was lifted up for pictures-taking.

The same fabric cover and metal frame were also similarly used in setup of reflection mode.

Reflection Mode: Two camera flashes were used, which were each positioned on the left and right hand sides of the IR camera. Both camera flashes were tilted at an angle (45° to the horizontal plane) for covering as much sample surface areas as possible. For each sample, the setup was adjusted to assure the observed sample region was at the centre of the field of view (Figure 3.15).

Figure 3.15. Setup for analyses of PMMA plate in reflection mode.

The setup of the filament-samples were slightly different, which were to be demonstrated in the following section. This was because the filaments were much smaller than the PMMA plate and they all needed to be fixated at a position for IR data collections.

3.4.3 Notched PLA filaments and the rest of filaments

An optimum set up would enable a full defect to be included in the FOV. This would maximise pixels contained within the defect while also including surrounding non-defect areas.

1. Setup in transmission mode.

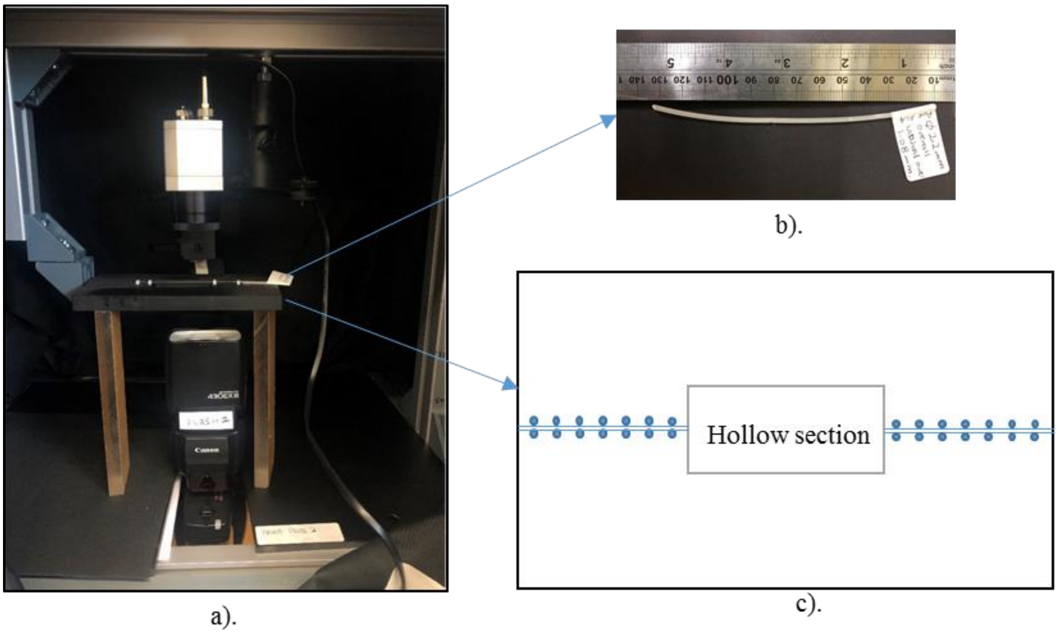

a). b). c).

Figure 3.16. Setup of filaments in transmission mode.

Where a). the setup in transmission mode, b), the original appearance of the sample, which was later sprayed into matt black for data collection and zip tied (into straight and fixed position) onto the sample holder c). The sample holder had a hollow section cut out; 40x50x6 mm. The holder was used to keep curved filament straight at a fixed position. Any small movement of the filament would result in an unclear thermal image, an example to that was blurry sections in frames of recorded data videos.

2. Setup in reflection mode

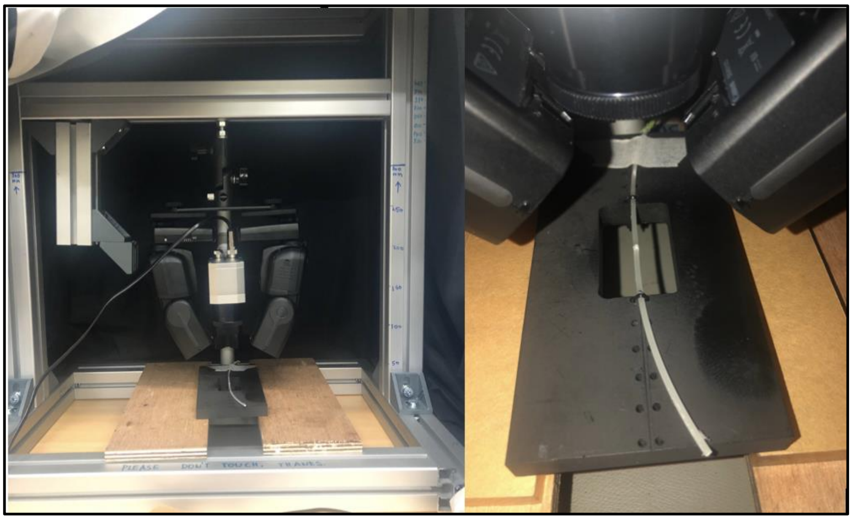

Figure 3.17. Setup of pure PLA filament in reflection mode.

Filaments were either positioned horizontally or vertically, which were positioned according to the convenience of the observations. A demonstration is shown in Figure 3.18.

Depending on the clarification and the light distribution of the recordings, the orientation of filaments orientation under IR camera was adjusted accordingly.

1. The orientation of filaments

Data recordings of filaments were collected in both transmission and reflection modes. Filaments were either positioned vertically or horizontally to prevent the field of view from being obstructed. This was because when in reflection mode, camera flashes were closely positioned besides the IR camera, where the camera flash heads can block or obstruct the FOV. This would result in blurred regions along the FOV. Data collected under this condition were therefore difficult to process. The processed results would in turn have an increased amount of noise signals; causing non-sample artefacts, losing significant amount of signals and misleading image information. Samples were therefore rotated accordingly.

By rotating the orientation of samples, imaging quality was improved without losing significant data information. The processed results were therefore able to provide images with better clarity and details.

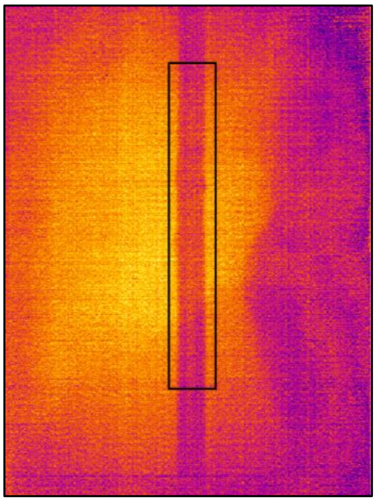

Figure 3.18. Screenshot of the recording window from Viewer, filament's orientation on screen.

Various sizes of sub-frame window were tested and compared during experiments. This was to ensure the sample appeared in FOV region had no edges cutting out nor obstructed by the equipment. The digital signal values have not been converted to thermal data at this stage.

Challenging defects are defects of deeper depths, smaller or less thermal conductivity contrast under IR camera.

PLA mixed salt particles, coarse harakeke fibres mixed PLA filaments

Setup in transmission mode was similarly conducted as in Figure 3.16. Setup in reflection mode was similarly conducted as in Figure 3.17.

Treated harakeke fibres reinforced polymers

The setups in transmission and reflection modes were the same as in Single Notched Pure PLA filaments. An example to that would be in Figure 3.19, where the data recordings were conducted in transmission mode.

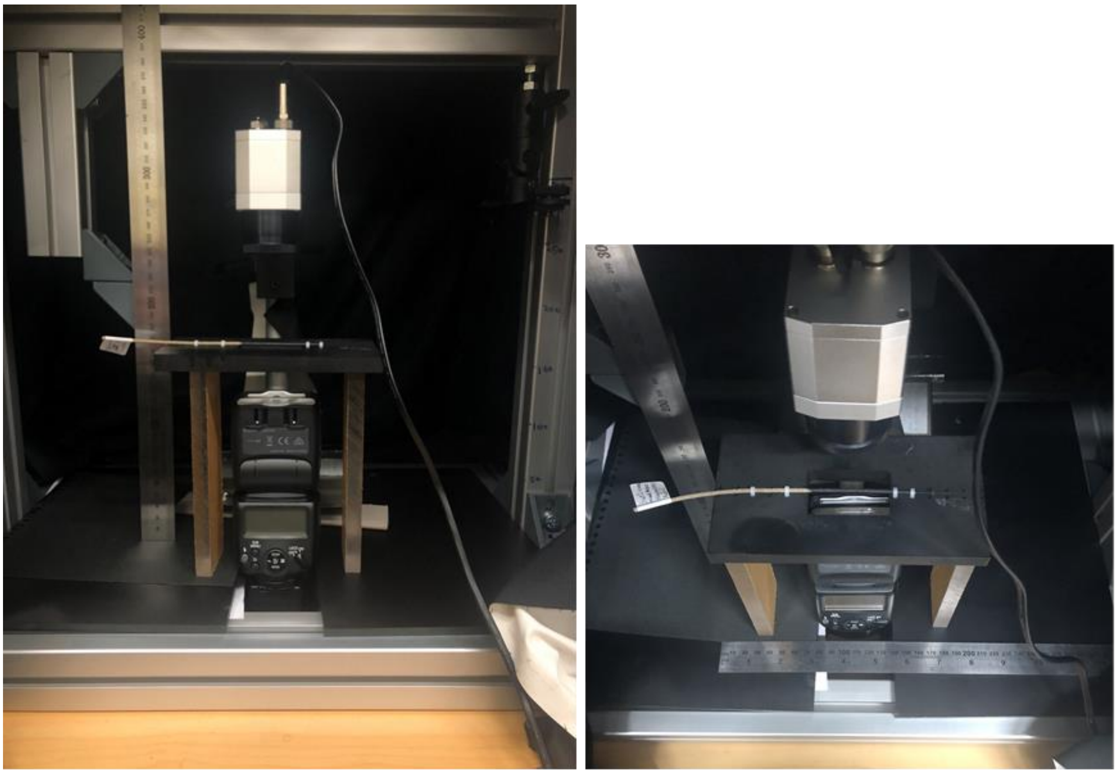

1. 2.

Figure 3.19. Setup of harakeke reinforced PLA in transmission mode.

In Figure 3.19, the entire setup in transmission mode and 2. Image on the right hand side was the close-up of how the filament was zip tied onto its holder and where the heat was propagating through.

3.4.4 Local environment

Environmental elements such as room temperature and humidity were considered. Ambient temperature is an important factor when considering creating a temperature contrast as in IRT. Ambient temperature affects the data collection externally [105]. A range of preliminary test were therefore conducted to observe the impact. In order to minimise the impact level of influential factors, raw data recordings were collected on the same day for the same sample.

The humidity percentages were recorded according to the local weather report. Although humidity was not expected to have a significant impact over such short ranges of distances, i.e. distance between the sample and camera, humidity was always recorded in the case of any spurious data.

The laboratory temperature were diurnal. Room temperatures were recorded between experiments, using a digital thermometer positioned nearby.

The internal temperatures of equipment can also vary. The IR camera can heat up internally throughout operations and this affect the quality of (thermal) data recordings. Microbolometer as the sensor, sensitive to surrounding temperatures and emission of infrared energy from samples. The IR camera was therefore turned off and allowed to cool at every hour.

Sources of infrared energy in the local environment included the PC screen, laboratory room light and daylight. By covering the entire setup apart from PC with a thick and matt black fabric sheet, the entire experimental setup was shielded, minimising the impact of external sources. While this blocked out external sources, the IR camera itself heats up and therefor is an unavoidable source.

3.4.5 Field of view (FOV)

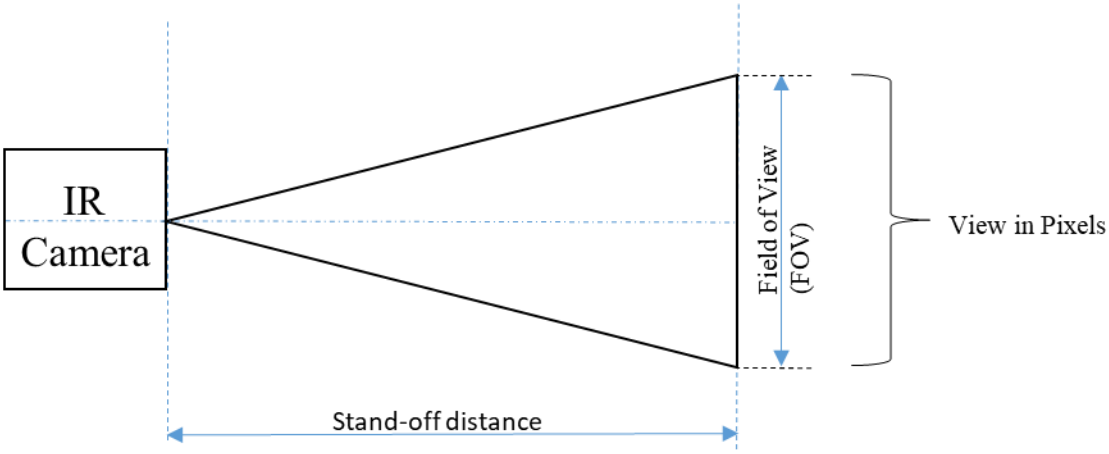

Figure 3.20. A schematic diagram of FOV.

FOV was also influenced by whether the IR camera and the sample were normal to each other. If they were not normal, distortion occurs where pixels at one side of the image represent a different physical length to the other side. To prevent this the IR camera was mounted onto a frame that was levelled. This was done prior to the start of each data recording. The metal frame helped to fix the stand-off distance, hence the FOV, and created a repeatable set up between experiments.

There were different ways in determining the FOV:

Depending on the measurements demonstrated above, i.e. stand-off distance, an official website link that contains a specified calculator is available from the company of the Optris IR camera [109]: The Optics Calculator helps to detect the best possible position of Optris PI thermal imaging camera, in which it provides the section of the lens that is used for experiments, then enter the determined/measured distance between the lens and the surface material. The calculator will then calculate the FOV at object surface along with width (HFOV), height (VFOV), diagonal (DFOV), pixel size (IFOV) and 3 x 3 pixel (MFOV) distances/values [110]. The effective aperture at lens position and the effective aperture at front end of device indicated the ending result of Optics Calculator (Figure 3.21).

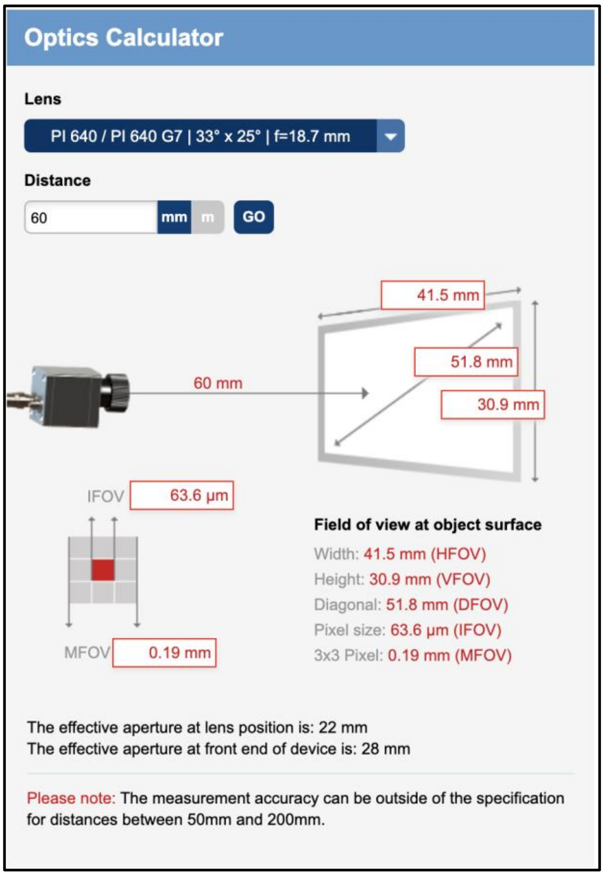

Optics Calculator

Lens: PI 640 / PI 640 G7 | 33° x 25° | f=18.7 mm

Distance: 60 mm

Field of view at object surface

Width: 41.5 mm (HFOV)
Height: 30.9 mm (VFOV)
Diagonal: 51.8 mm (DFOV)
Pixel size: 63.6 µm (IFOV)
3x3 Pixel: 0.19 mm (MFOV)

The effective aperture at lens position is: 22 mm
The effective aperture at front end of device is: 28 mm

Please note: The measurement accuracy can be outside of the specification for distances between 50mm and 200mm.

Figure 3.21. Online Optics calculator [109].

Alternatively, the physical measurement of FOV can be manually measured. A reflective paper ruler was used measure the actual length of the FOV for each set of data collection. This was positioned right next to the sample at the same surface level.

Pixels were converted into its actual physical sizes in mm, this was to calibrate the captured image. Imaging pixels observed on the computational screen need to be converted into actual sizes in mm and this can be carried out through simple ratio [111]:

$$\frac{x}{y} = \frac{a}{b} \tag{3-1}$$

where a is the length recorded in sub-frame window in Matlab, b is the actual length of filament/material recorded in millimetres, x is the width recorded in sub-frame window in Matlab and y is the actual width of filament/material recorded in millimetres.

The IR camera and the sample were both levelled, this was to ensure the entire FOV remained in focus. This is significant because the focus of microbolometer lens varies in response to different distances set between the lens and the specimen. All dimensions were measured in millimetres. Any slight movement of the setup or sample can be displayed in the field of view on PC screen. It was therefore important to avoid any surface level deviations during data collection. If the sample was not seen or positioned at the centre of the field of view, thermal recordings of such would be disregarded.

3.5 Data processing

It is acknowledged that thermography data contains a high level of noise; therefore, when defects are deeper or smaller, i.e. harder to detect, the data processing steps implemented are key to defect identification.

Data processing was carried out in Matlab. Established thermography processing techniques were performed and compared for each sample, in both transmission and reflection modes. The established routines implemented include; Thermal Signal Reconstruction (TSR) and Pulsed Phase Thermography (PPT). Alongside TSR and PPT spatial denoising in the form of wavelet denoising applied in two dimensions (2D) was used.

The data processing approach used for reflection data was presented in section 3.5.1, where the purpose of specific processing scripts is included. The minor alterations to this process required for transmission data sets are then covered in section 3.5.2.

The purpose of processing procedures was to identify the largest contrast. The general procedure demonstrated by Figure 3.22. It was applied to all sample materials.

3.5.1 Reflection data processing procedure

A flow chart was used to illustrate the overall procedure, as shown in Figure 3.22. Once raw data was collected in reflection mode, the first stage of processing was to remove frames in the recording that are before the flash frame. Flash frame was detected by determining the maximum value of the digital data. The purpose of including these frames in the recordings was to have a record of the pre-flash data as a baseline to refer to in case of any spurious datasets. The next stage of analysis was to find the maximum contrast frame.

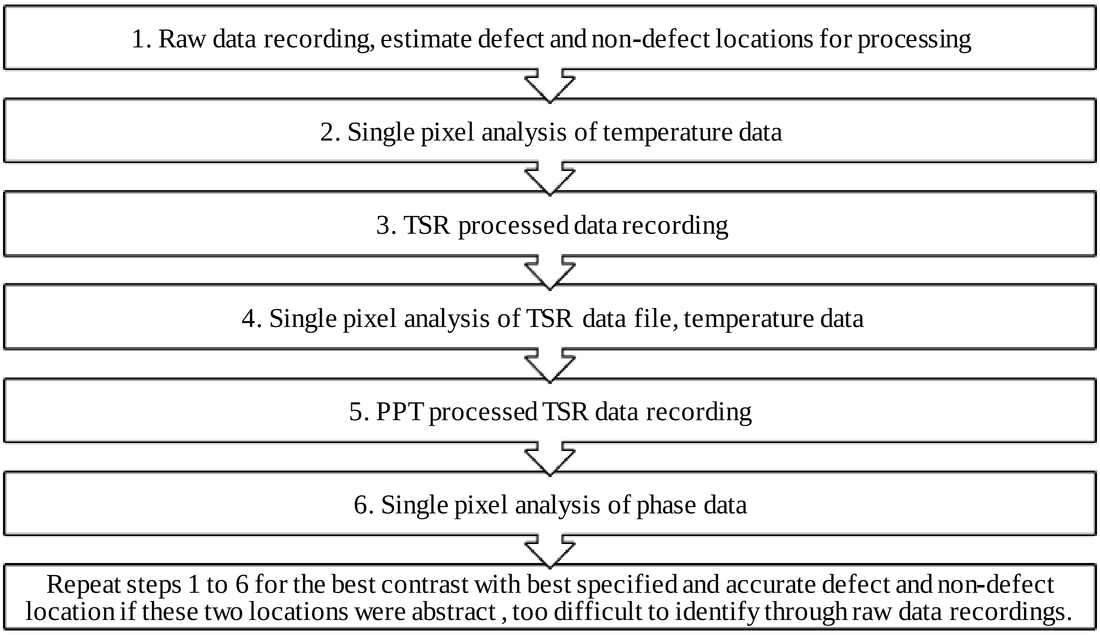

Figure 3.22. Defect detection data process procedures

Maximum thermal contrast identifies the maximum difference between temperatures of defect and non-defect (sound) areas. These areas each consisted of four by four (4x4) pixels. This was because in general, the total flow of heat entropy (heat diffusion) of a system is difficult to measure, but the measure of changes in heat entropy can be fairly easy [112]. Therefore the thermal response of the sample was to be measured and the corresponding images of thermal contrast were to be collected and processed digitally.

The frame of maximum contrast in thermal data was determined during wavelet denoising. The frame of maximum contrast was identified differently when the defect is evidently seen, and when the defect is not apparent in the raw data. When the defect is clear to visualise, the frame of maximum contrast could be identified directly by watching the raw data recording. For each set of data collection, the plotted thermal images were produced and used in the final procedure. The processing of each raw data were kept consistent. When the defect was not clear to visualise, two regions were selected as an initial processing position. From these regions, thermal contrast was determined through time, as shown in Figure 3.23. The frame containing the maximum thermal contrast was then identified.

Once the frame of maximum contrast in the raw data is identified, this frame was then spatially denoised using wavelet denoising.

Noise-deducing tools are vital when collected raw data does not provide meaningful information. Noise-reducing tools such as wavelet denoising was applied to the raw data throughout imaging analysis.

Wavelet denoising was used to reduce the high-frequency spatial noise across the field of view that is caused by noise inherent to IR camera.

Wavelet denoising denoises the data in two-dimensional direction by using an empirical Bayesian method with a Cauchy prior (Lorentz distribution). Wavelet transform localised features of images and signal into few of large-magnitude wavelet coefficients and applied through both x and y directions of the maximum contrast frame. Wavelet coefficient values are significantly smaller than others, they can be “shrank” or removed without changing the properties of the raw data collected. Decimated wavelet transform (DWT) implemented from the Matlab Signal Processing Toolbox was used, and the associated results were plotted alongside the original frame [113].

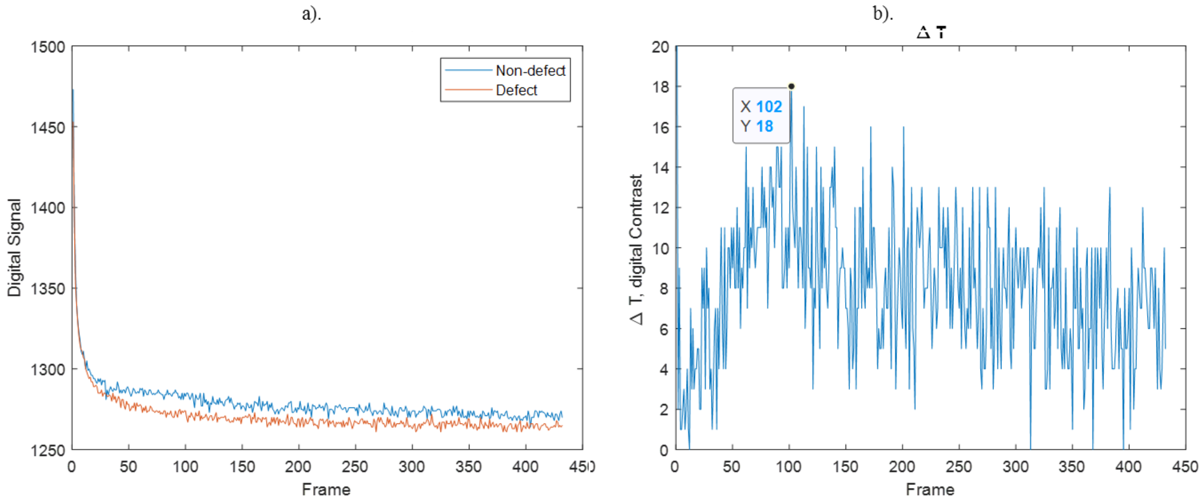

Figure 3.23. Raw data results: a). single pixel plot (wavelet denoised raw data) of the selected defect and non-defect locations, b). Maximum thermal contrast between the defective and non-defective regions. Shallowest defect depth of 0.50mm, PMMA plate. Raw data.

Figures of raw digital signals versus frame numbers were plotted for each set of experiment. The frame of maximum thermal contrast was identified from the x-axis value, as shown in Figure 3.23. Digital signals of defective region was compared alongside the digital signals of non-defective region, these were plotted in a). Thermal contrast shown in b) was the subtracted result of defect and non-defect signals.

The next stage of processing was to apply thermal signal reconstruction (TSR) to the raw data, per pixel through time. TSR, a method used for non-destructive, reference-free thermography detection of subsurface defects. For each pixel through time a thermal decay was recorded. In TSR this decay was converted into a logarithmic timescale, where a least squares fit (line of best fit) was applied to the data for generation of a polynomial expression. This polynomial expression was then transformed into the original linear timescale with improved signal-to-noise characteristics [114].

In order to see the impact of TSR on raw data, figures of TSR processed digital signals were plotted, as shown in Figure 3.24.

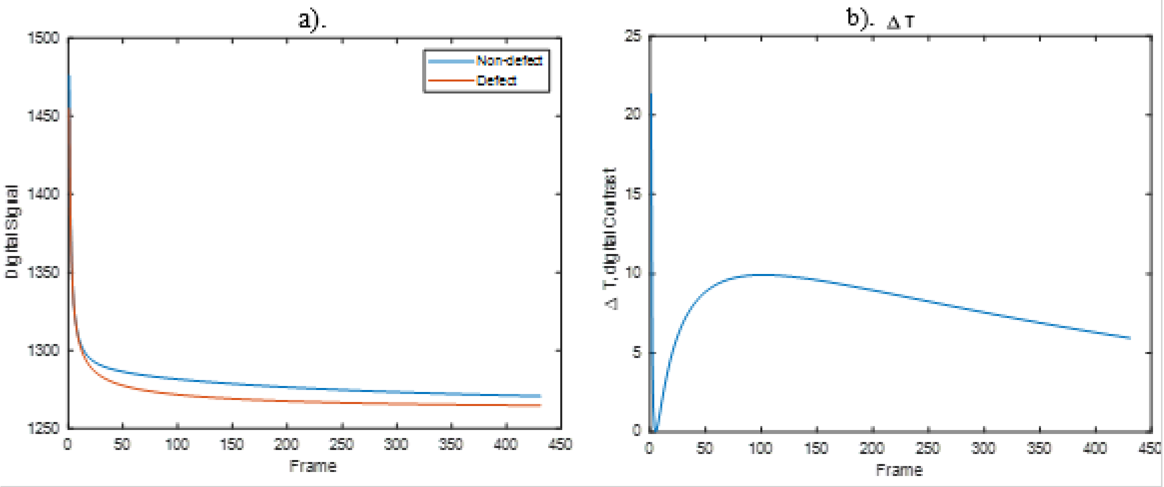

Figure 3.24. TSR processed results: a). single pixel plot of the selected defect and non-defect locations, b). Maximum thermal contrast between the defect and non-defect locations. Shallowest defect depth of 0.50mm, PMMA plate. TSR processed raw data; TSR data.

Great amount of signal noise was reduced, as shown in Figure 3.24. This was due to the noise removal of the TSR process. This was shown in Figure 3.24 a), where the thermal differences appeared after the flash heat was emitted. The emission of flash heat resulted as the peak in figures, in which below the 50th frame, the thermal differences appeared. The thermal difference was then gradually reduced with time.

In b), the peak (exclude intersection of y-axis) of the figure was an indication of maximum thermal contrast. Thermal images produced after TSR processing were expected to have better defined defect and more surface/subsurface details. Wavelet denoising was also applied to TSR processed data.

Pulsed phase thermography (PPT) processing was then the undertaken on the TSR dataset. PPT processing applied a fast Fourier transform (FFT) through time per pixel of the TSR dataset. The application of FFT had been shown to be less affected by experimental conditions such as uneven surface heating [115]. FFT produced real and imaginary components prior to the phase calculation of each pixel, which was governed by;

$$\varphi(f) = tan^{-1}\frac{I(f)}{R(f)} \tag{3-2}$$

Where, $\varphi(f)$ was the phase as a function of frequency, $I(f)$ and $R(f)$ were the imaginary and real components of phase data. This was the result of application of FFT [59]. The phase angles $\varphi(f)$ per pixel were determined and used for constructing phase images of an individual frequency.

Subsurface defects were then detected by determining the maximum phase contrast (difference) between the defected and non-defected locations. Similarly to that used in TSR processing, each of these locations were selected from four by four (4x4) pixels.

The results of this processing were sets of phase data, in which the temperature-time data was transformed into phase-frequency domain. Phase value of each pixel at a particular frequency was calculated. A set of phase images were produced as a result.

An individual frequency was selected by plotting phase images at different frequencies. As part of the final set of results, phase images of best clarity alongside colour bars of most extensive range were selected. These images were known as the maximum phase contrast. For this process, the frequency was not always the same throughout the data processing.

Once the frequency of best phase contrast was determined, 2D wavelet denoising was applied to PPT (phase) data. At this stage, six results images were produced.

If the defect location was visibly presented by the raw data and enabled defect and non-defect regions to be selected in step six; single pixel analysis of PPT data, then the processing was stopped here.

However, if the defect was not visible in the raw data, phase data may have revealed previously unidentifiable defects. The phase data can now be manually assessed to update the defect and non-defect areas selected, and the maximum contrast frames displayed for raw and TSR data re-evaluated based on this.

Furthermore, colorbar of phase and thermal images can be modified at the end. Defects-visual appearance and manual edge definition can be improved by modifying the colorbar ranges.

3.5.2 Processing amendments for transmission data

There was only a difference between reflection and transmission data processing and that was the identification of the flash frame. In transmission mode, where the flash was behind the ample relative to the camera, a flash frame was not always clear.

For recordings that the flash frame was not visible, the recording was not cropped in transmission mode.

Chapter 4

Results and Discussion

4.1 Introduction

In this chapter, digital images from raw and TSR processed data are presented. While 2D spatial information is presented, it is noted that all data is derived from three-dimensional data, i.e. collection through time. Raw and TSR data results presented are both thermal data. Phase data results presented are phase angle at particular frequencies, which were produced using PPT.

4.2 Evaluation of the limit detection with depth

Experimental results are presented according to the complexity of the samples, in terms of defect detection and realism. Flat bottom holes (FBH) of the PMMA plate were the first set of artificial defects to be tested. The next set of experiments were notched PLA filaments. This set of filaments had a consistent diameter, and square notches of the same width were milled to different depths into the PLA filaments. Once the detection limits of the thermography setup according to the defect depth was investigated, various types and sizes of subsurface defects were introduced in the following experimental stages. The next most challenging defects were NaCl (salt) particles, which were at least 100 times smaller than FBH and notches.

Filaments containing salt particles and coarse/untreated Harakeke fibres were investigated. The remaining experimental stage was to investigate materials used to produce 3D-printed objects; polymer filaments reinforced by treated Harakeke fibres.

Each sample was inspected in both transmission and reflection modes of IRT inspections. The data presented for each defect or sample are as follows:

A) Maximum thermal contrast - raw data.
B) Wavelet denoised maximum thermal contrast data from A).
C) TSR maximum thermal contrast data.
D) Wavelet denoised TSR maximum thermal contrast data from C).
E) Maximum phase contrast data.
F) Wavelet denoised maximum phase contrast data from E).

4.2.1 Polymethyl methacrylate (PMMA) plate

FBH defects in the PMMA plate are inspected and results presented in order of transmission inspection then reflection inspection. Within each inspection set up defects inspected increased in difficulty for the inspection, hence in the case of the PMMA plate in order of increasing depth.

Transmission Mode:

Samples were thermally excited, and the thermal response of the surface on the oppose side to heating was observed. In all thermal data (raw and TSR), warmer colours (yellow) correspond to the higher temperatures and cooler (blue) colours correspond to lower temperatures.

The first defect to be inspected was the 0.5 mm deep FBH where the results are presented in Figure 4.1. In Figure 4.1, in both raw (Figure 4.1A) and TSR processed data (Figure 4.1D), defect-edge had great definition even before spatial denoising. Corresponding spatially denoised images are presented in Figure 4.1B and D respectively. TSR processed digital images were expected to have improved detection of defects and/or enhanced edge clarity when compared to the raw data results [104], however for such shallow and clearly detectable defects the advantages of TSR are minimal.

Variation of readings (colours) across the FOV (aside from the defect) in thermal and TSR data were mainly caused by non-uniform flash emission and different amount of heat propagating through the sample. The largest amount of the heat energy was emitted from the centre region of the camera flash which causes hotter temperatures in the central region of the FOV. This was an unavoidable feature as the flash-heat distribution was restricted by the physical setup which had limited options for adjustments. This gradient was not caused by lens distortion as the data viewed is only central subset of the FOV and lens distortion would not be dominant in this region.

Defect	**0.50 mm in defect depth Flat bottom cylinder hole on PMMA plate**	**Transmission Mode**
Data Type	**Maximum Δ T:**	**Wavelet Denoised maximum Δ T:**
Raw data	**A** 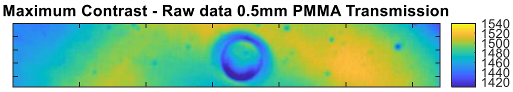 	**B** 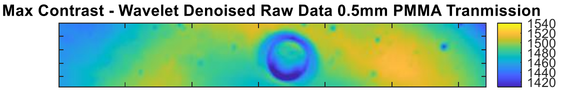
TSR data	**C** 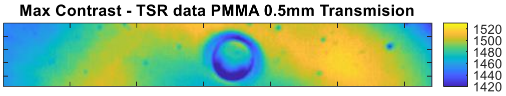 	**D** 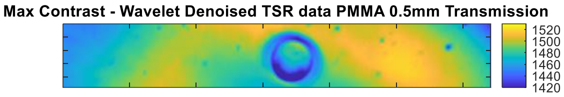
Data Type	**Maximum $\Delta\phi$:**	**Wavelet Denoised Maximum $\Delta\phi$:**
PPT data	**E** 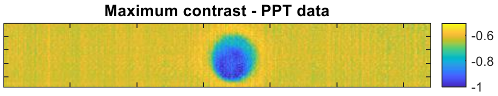 	**F** 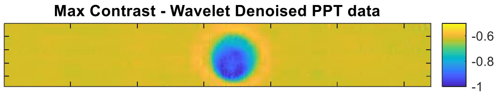

Figure 4.1. Thermal and phase images of the PMMA plate conducted in transmission mode.

Phase images E and F presented in Figure 4.1 resulted from PPT processing (E) and 2D wavelet denoising applied to the phase data (F). The PPT results, the images represented the maximum phase contrast of a single frame. Images displayed were selected by choosing images with a significant amount of phase contrast information, where the defect had the clearest edge definition determined visually. Phase contrast is of interest between the defect and non-defect regions rather than absolute phase values as this gives information about the relative different of the heat paths between the two regions. The wavelet denoising procedure was used to aid PPT processing.

The defect became clearly visible at a certain frequency, and this was known as the blind frequency. PPT had a considerable amount of noise contents, particularly at higher frequencies, higher than the third or fourth frame for example. When at higher frequencies, more white noises appeared in the phase data results, as shown in Figure 4.2.

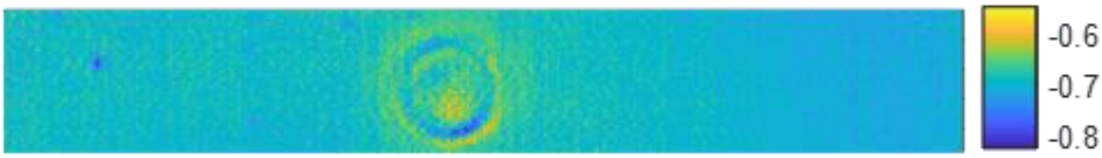

Figure 4.2. PPT processed phase image, plotted at frequency frame 5.

The next defect analysed was the FBH defect of 0.75 mm in depth. As the defect gets deeper, the processed images were expected to have less edge definition and image clarity.

The thermal gradient of defective and the non-defective regions was less distinguishable in thermal images. Thermal differences were reduced when inspecting deeper defects. This was because the heat transfer was dependant on amount of the sample it propagated through [112].

Defect:	**0.75 mm in defect depth Flat bottom cylinder hole on PMMA plate**	**Transmission Mode**
Data Type	**Maximum Δ T:**	**Wavelet Denoised maximum Δ T:**
Raw data	**A** 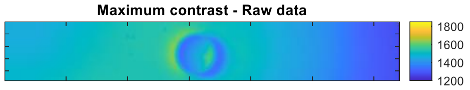	**B** 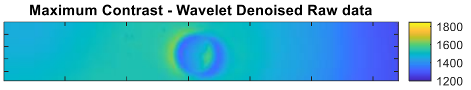
TSR data	**C** 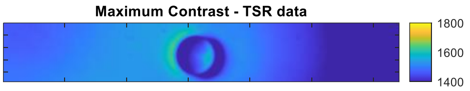	**D** 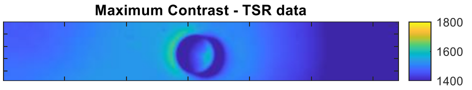
Data Type	**Maximum $\Delta\phi$:**	**Wavelet Denoised Maximum $\Delta\phi$:**
PPT data	**E** 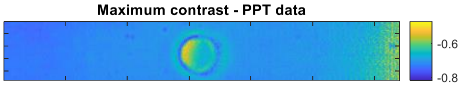	**F** 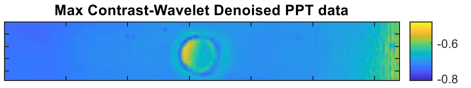

Figure 4.3. Thermal and phase images of the PMMA plate conducted in transmission mode, defect depth of 0.75mm.

Figure 4.3A, B, C and D were thermal data, A and B were plotted from raw data where B is the denoised version of A, C and D were plotted from TSR processed data, where D is the denoised version of C. The non-uniform heating discussed previously remained evident in figures A-D. The thermal gradient was more apparent in images C and D when compared to images A and B due to the different colour bar used on the presented data.

After PPT processing, the defect was visible in images E and F, as shown in Figure 4.4. Wavelet denoised PPT data, where image F was smoothened overall when compared to image E. Phase contrast of the defective and non-defected regions were still visible.

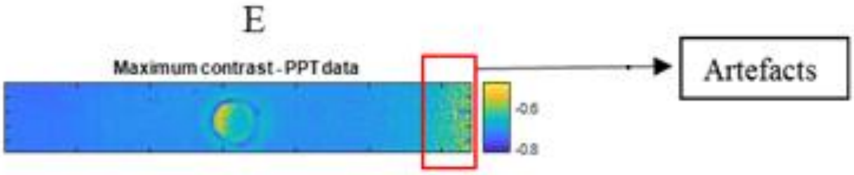

Figure 4.4. PPT processed image from defect depth of 0.75mm

There were few artefacts appeared on the right hand corner of the image, as shown in Figure 4.4. These artefacts may be the random errors resulted from the IR camera. . This is likely due to phase wrapping, where phase wrapping is found where the difference in heat paths is sufficient to cause a phase range that exceeds the range ±180°. In Figure 4.4 this is caused by the non-uniform heating.

Defect:	**1.00 mm in defect depth** **Flat bottom cylinder hole on PMMA plate**	**Transmission Mode**
Data Type	**Maximum Δ T:**	**Wavelet Denoised maximum Δ T:**
Raw data	**A** 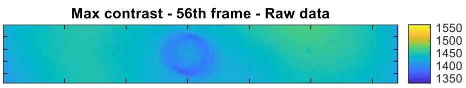	**B** 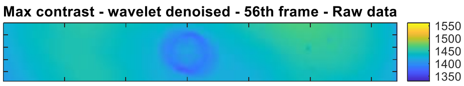
TSR data	**C** 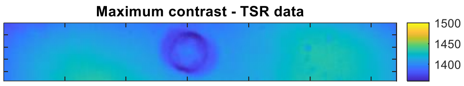	**D** 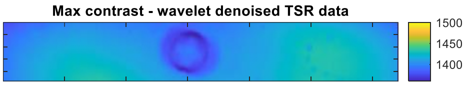
Data Type	**Maximum Δϕ:**	**Wavelet Denoised Maximum Δ ϕ:**
PPT data	**E** 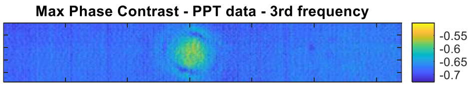	**F** 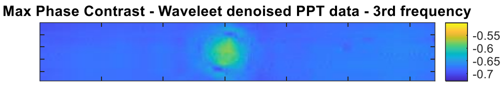

Figure 4.5. Thermal and phase images of the PMMA plate conducted in transmission mode, defect depth of 1.00mm.

In comparison to the shallower defects, thermal contrast for defects of a depth of 1.00mm was reduced however defects were still clearly identifiable in both thermal and phase images, as shown in Figure 4.5.

When comparing the phase images of different defect depths, identification of defects were less distinguishable for deeper defects with reduced edge definition. Up to defect depth of 1.0mm, the defect was still identified in both original and wavelet denoised images. The artefacts discussed in defect depth of 0.75mm were not visible at deeper defects of PMMA plate.

Defect:	**1.25 mm in defect depth Flat bottom cylinder hole on PMMA plate**	**Transmission Mode**
Data Type	**Maximum Δ T:**	**Wavelet Denoised maximum Δ T:**
Raw data	**A** 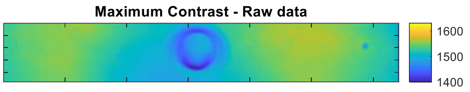 	**B** 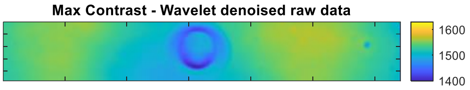
TSR data	**C** 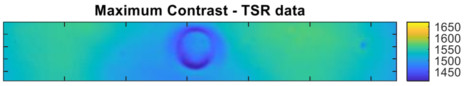 	**D** 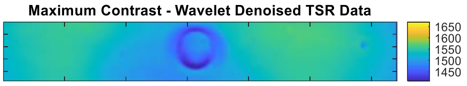
Data Type	**Maximum $\Delta\phi$:**	**Wavelet Denoised Maximum $\Delta\phi$:**
PPT data	**E** 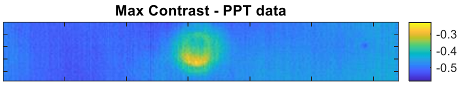 	**F** 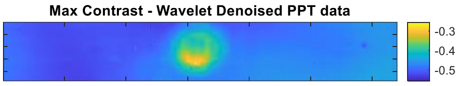

Figure 4.6. Thermal and phase images of the PMMA plate conducted in transmission mode, defect depth of 1.25mm.

Thermal data (A-D) presented in Figure 4.6 for defect with depth 1.25 mm had higher contrast when compared to the thermal data (A-D) in Figure 4.5. This is not as expected and highlights a problem with the 1.00 mm data set which would require further investigation.

The non-uniform heating discussed for the shallower defects was also present in thermal images A-D in Figure 4.6. When comparing thermal images A-B to TSR processed images C-D, the defect edge definition was not greatly improved after TSR processing as the defect was already clear in the raw data as discussed previously.

The contrast between the defect and non-defect was evidently presented in images A-F (Figure 4.6), although the ‘phase hotspot’ appeared at the bottom of the defect region, this was indicated by phase images E and F, as shown in Figure 4.6.

After the wavelet denoising, the defect edge definition of image F was much improved from the original, image E. This indicated that the 2D wavelet denoising was more effective when applied to deeper defects where signal to noise ratio is higher.

Defect:	**1.50 mm in defect depth Flat bottom cylinder hole on PMMA plate**	**Transmission Mode**
Data Type	**Maximum Δ T:**	**Wavelet Denoised maximum Δ T:**
Raw data	**A** 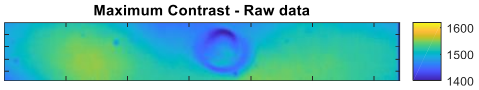 	**B** 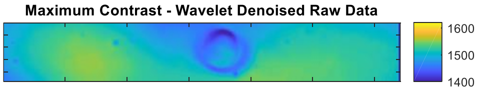
TSR data	**C** 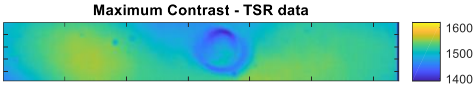 	**D** 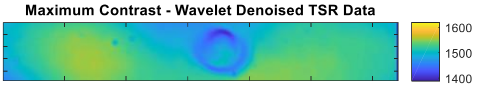
Data Type	**Maximum $\Delta\phi$:**	**Wavelet Denoised Maximum $\Delta\phi$:**
PPT data	**E** 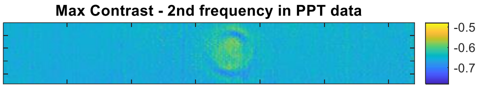 	**F** 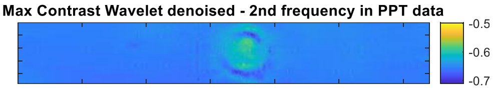

Figure 4.7. Thermal and phase images of the PMMA plate conducted in transmission mode, defect depth of 1.50mm.

Similarly, the defect of 1.50 mm defect depth data showed the thermal gradient caused by the non-uniform heating, as shown in in Figure 4.6. The thermal gradient appeared reduced at defect depth of 1.50 mm when compared to defect depth of 1.25 mm however this is just due to the figure plotting. The defect edge definition of 1.50 mm was however more distinguishable than the defect depth of 1.25 mm which highlights a more robust method of edge detection could be introduced.

Beyond the (defect) depth of 1.00 mm, edge definition of the defects were expected to have lower contrast and less clarity when compared to Figure 4.1 and Figure 4.3. The impact of thermal conduction was detected overall.

The greater defect of depth of 1.75 mm was the following defect to be inspected, as shown in Figure 4.8.

Defect:	**1.75 mm in defect depth Flat bottom cylinder hole on PMMA plate**	**Transmission Mode**
Data Type	**Maximum Δ T:**	**Wavelet Denoised maximum Δ T:**
Raw data	**A** Maximum contrast - Raw data -45th frame 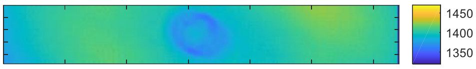 	**B** Maximum contrast - Wavelet Denoised - Raw data -45th frame 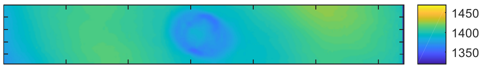
TSR data	**C** Maximum Contrast - TSR data 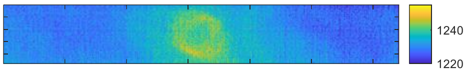 	**D** Maximum Contrast - Wavelet Denoised TSR Data 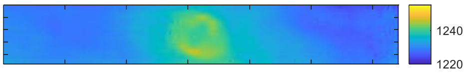
Data Type	**Maximum $\Delta\phi$:**	**Wavelet Denoised Maximum $\Delta\phi$:**
PPT data	**E** Maximum contrast - PPT data - 4th frequency 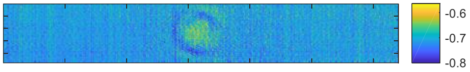 	**F** Max Contrast-Wavelet Denoised PPT data- 4th frequency 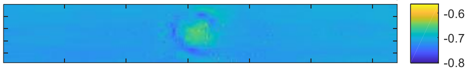

Figure 4.8. Thermal and phase images of the PMMA plate conducted in transmission mode, defect depth of 1.75 mm.

Thermal data images A-D of Figure 4.8 had less defined edge definition when compared to shallower defects as expected.

For materials with low through-thickness thermal diffusivity, the inspections can be limited to materials of certain depths, where the near surface features create the clearest signals [65].

In phase images E and F, the defect edge was well still able to be defined, particularly in the denoised data for this deeper defect depth, 1.75 mm in transmission mode, as shown in Figure 4.8.

Defect:	**2.00 mm in defect depth Flat bottom cylinder hole on PMMA plate**	**Transmission Mode**
Data Type	**Maximum Δ T:**	**Wavelet Denoised maximum Δ T:**
Raw data	**A** 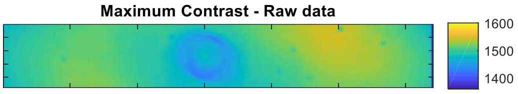	**B** 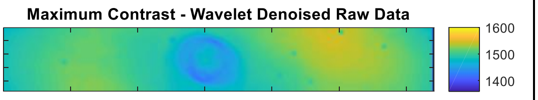
TSR data	C 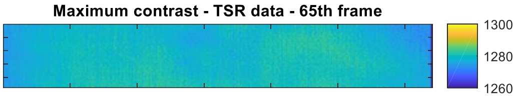	D 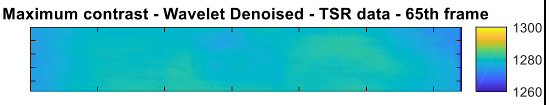
Data Type	**Maximum Δϕ:**	**Wavelet Denoised Maximum Δ ϕ:**
PPT data	**E** 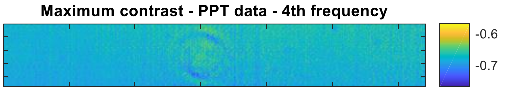	**F** 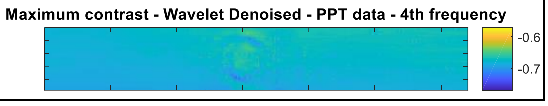

Figure 4.9. Thermal and phase images of the PMMA plate conducted in transmission mode, defect depth of 2.00mm.

The results in Figure 4.9 are for the maximum depth of 2.00mm in the PMMA plate. The edge definition of the defect was not defined as clear as in TSR processed images (C and D) as in the raw data (A and B) which suggests an issue with this TSR data selected which would need further investigation. The gradual change of phase values were visible in phase images, E and F. Although the defect was blurred in raw thermal images A and B and it was not visible in TSR images C and D, the deepest defect was still identifiable in the phase images.

With increasing defect depth particularly beyond 1.5 mm (Figure 4.8), it became more difficult to identify FBH defects, as shown in Figure 4.7, Figure 4.8, and Figure 4.9.

Advantages in spatially denoising data was revealed particularly where signal to noise ratios are reduced.

Overall, by evaluating the thermal and phase images of the PMMA plate, its deepest defect was the defect depth of 2.00 mm and it remained identifiable using the current setup in transmission mode processing procedures.

Reflection Mode:

Similarly with results collected in transmission mode, in reflection mode the thermal and phase contrast of defect and non-defect regions were also expected to be less distinguishable at deeper defects.

The defect-edge definition was also expected to decrease as defects gets deeper.

Defect:	**0.50 mm in defect depth Flat bottom cylinder hole on PMMA plate**	**Reflection Mode**
Data Type	**Maximum Δ T:**	**Wavelet Denoised maximum Δ T:**
Raw data	**A** 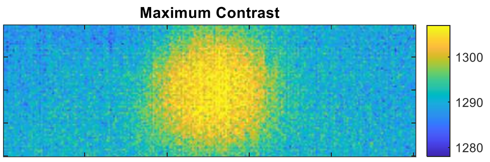	**B** 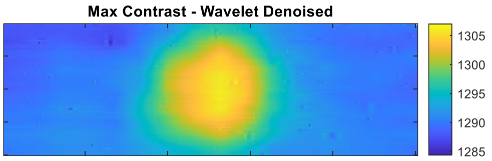
TSR data	**C** 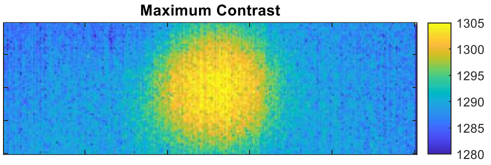	**D** 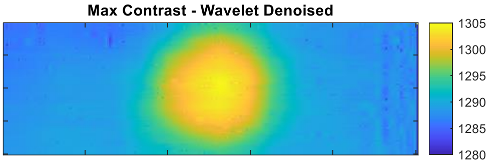
Data Type	**Maximum $\Delta\phi$:**	**Wavelet Denoised Maximum $\Delta\phi$:**
PPT data	**E** 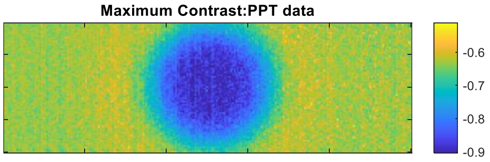	**F** 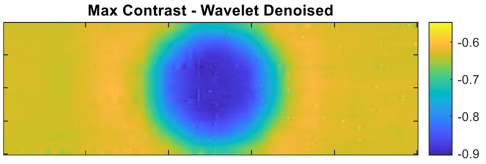

Figure 4.10. Thermal and phase images of the PMMA plate conducted in reflection mode, defect depth of 0.50mm

The shallowest defect (defect depth of 0.5 mm) was easily distinguished in all thermal and phase images in reflection mode, as shown in Figure 4.10.

The heat is conducted through the defect region where there is less material compared to the surrounding material. The propagation of the heat through this region is then slowed as it reaches the defect. This creates a hotspot as shown in Figure 4.10 A-D.

Wavelet-denoising process was applied along the x and y direction of thermal and phase data independently. The higher frequency spatial noise found in the thermal reflection data was largely removed, as demonstrated by comparing images A, C and E to B, D and F, respectively in Figure 4.10.

Wavelet - denoising can cause artefacts that are not actually in or on the sample material itself. However, artefacts created by the denoising process were easily distinguishable from the defect of interest. An example of these artefacts is labelled A in Figure 4.11.

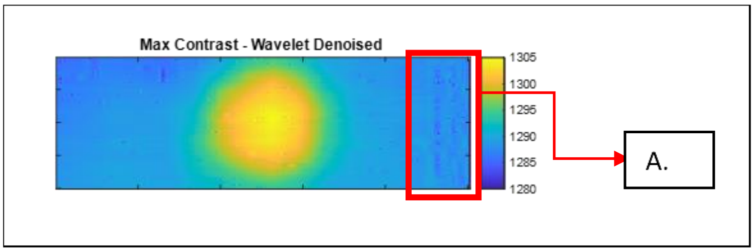

Figure 4.11. A. artefacts formed after wavelet-denoising process.

The phase data, is shown in Figure 4.10 E and F. The wavelet denoised phase data had good contrast and edge definition clarity. In this particular set of result, the defect size is seemly enlarged in phase data results than in thermal data results. This may due to the fact that the thermal gradient became more distinguishable to the eye with the colour of defect and surrounding reversed. It is noted that artefacts introduced in the thermal data by spatial denoising were less evident in the phase data.

The FOV was used to determine the overall width of the recording sub-window, which was 300 pixels in the image and 20mm in its physical size. The size of the defect could be determined by using the conversion of pixels to mm, which would be calculated based on the ratio of:

$$\frac{x}{y} = \frac{a}{b}; \frac{300}{75} = \frac{20}{b}, b = 5mm,$$

The diameter of the defect was therefore 5.0mm for 0.5mm depth of FBH on PMMA plate. The physical size was measured by a reflective paper ruler under IR. The number of pixels was determined from Matlab recording setup.

Defect:	**0.75 mm in defect depth Flat bottom cylinder hole on PMMA plate**	**Reflection Mode**
Data Type	**Maximum Δ T:**	**Wavelet Denoised maximum Δ T:**
Raw data	**A** 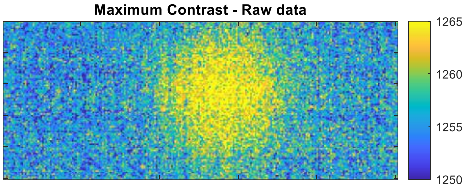 	**B** 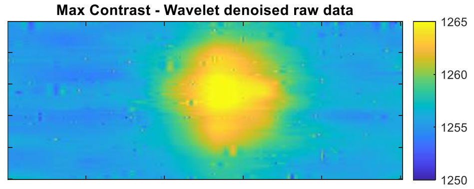
TSR data	**C** 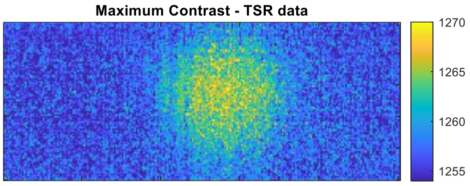 	**D** 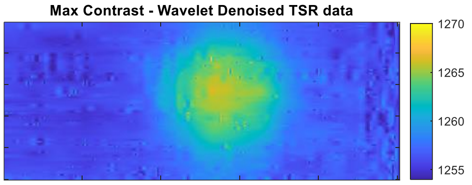
Data Type	**Maximum $\Delta\phi$:**	**Wavelet Denoised Maximum $\Delta\phi$:**
PPT data	**E** 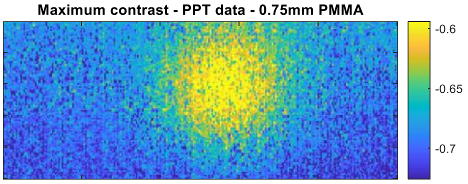 	**F** 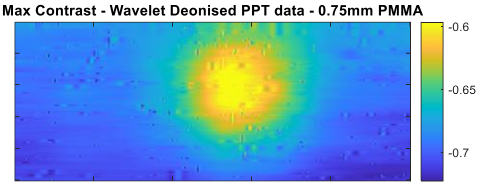

Figure 4.12. Thermal and phase images of the PMMA plate conducted in reflection mode, defect depth of 0.75mm.

In Figure 4.12, original thermal and phase data images (A, C, and E) had a great amount of noise which was reduced in the wavelet denoised images (B, D and F) and improved definition of the defect. The wavelet –denoising artefacts appeared more abundant when compared to shallower defects, as shown in Figure 4.10 and Figure 4.12. The clarity of the images was reduced when compared to the results presented in defect depth of 0.5mm, Figure 4.10. The reason for this is due to two factors, firstly the reflection process relies on the effects at the defect boundary being significant enough to cause an effect on the surface. Secondly, although there is double the energy used in the set up to provide heating, i.e. two flashes rather than one, so they do not appear in the FOV of the camera they are positioned further away from the sample surface and angled so not as much heat per flash is applied to the front surface in reflection mode as the rear surface in transmission mode. Similarly with the results of transmission mode, significant changes appear in the results beyond 1.00 mm deep.

Defect:	**1.00 mm in defect depth Flat bottom cylinder hole on PMMA plate**	**Reflection Mode**
Data Type	**Maximum Δ T:**	**Wavelet Denoised maximum Δ T:**
Raw data	**A** 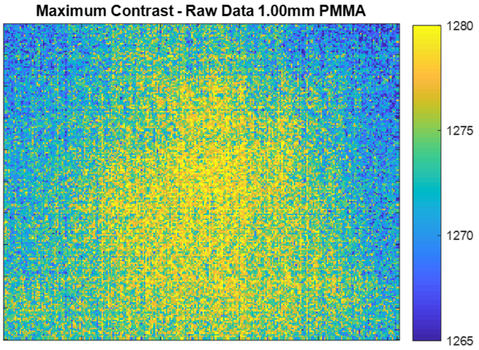 Maximum Contrast - Raw Data 1.00mm PMMA 	**B** 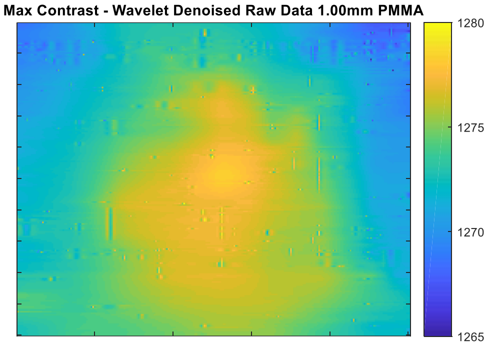 Max Contrast - Wavelet Denoised Raw Data 1.00mm PMMA
TSR data	**C** 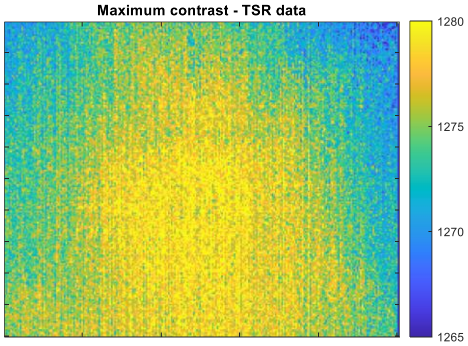 Maximum contrast - TSR data 	**D** 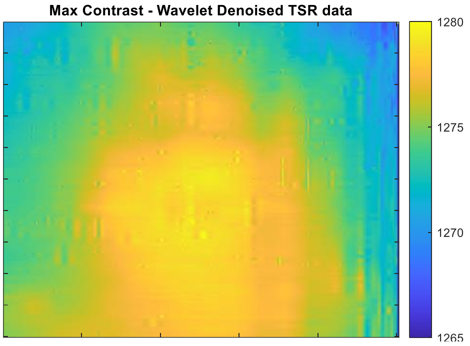 Max Contrast - Wavelet Denoised TSR data
Data Type	**Maximum Δϕ:**	**Wavelet Denoised Maximum Δ ϕ:**
PPT data	**E** 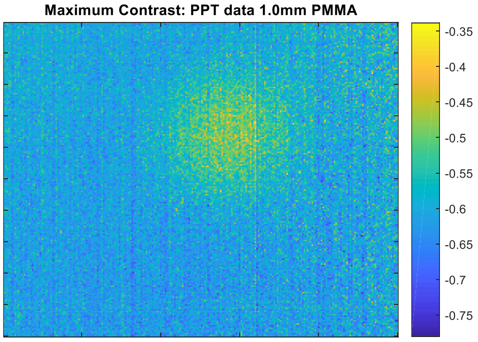 Maximum Contrast: PPT data 1.0mm PMMA 	**F** 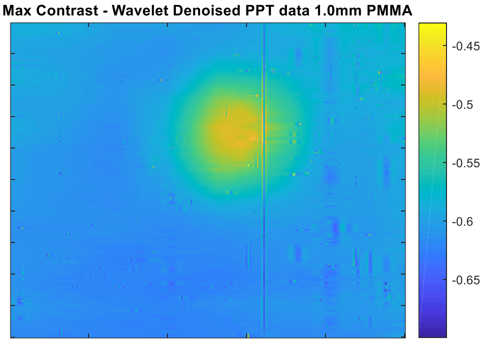 Max Contrast - Wavelet Denoised PPT data 1.0mm PMMA

Figure 4.13. Thermal and phase images of the PMMA plate conducted in reflection mode, defect depth of 1.00mm.

From 1.00 mm defect depth results onwards, the defect was not able to be distinguished in both raw and TSR data results as shown in Figure 4.13. The recording window was recorded at larger sub-window in this case to observe a larger area. This allows the non-uniform heating that is inevitable in reflection mode to be seen as in Figure 4.13A-D.

PPT processed phase data results are shown in Figure 4.13E and F. These results indicated that the PPT processing was able to probe the defect depth of polymer composites, which was at subsurface level. The defect is clearly identified in the phase data. In denoised phase data, the artefacts caused by the denoising are visible. Also visible in both the phase but more clearly in the denoised data is a clear vertical line, highlighted in Figure 4.14. Although not initially noticed in the thermal data, once identified in the phase data it is found in the raw thermal data also. This line is caused by the camera during the data capture and should not be considered a feature of the material of the processing.

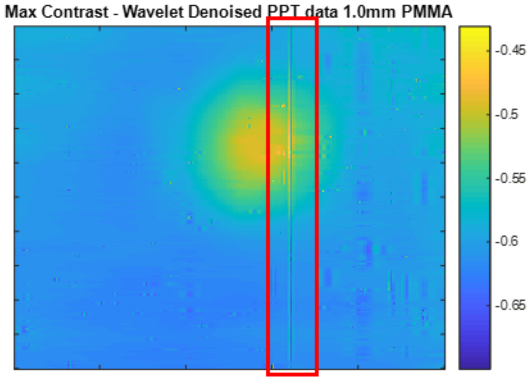

Figure 4.14. Phase image; figure F of Figure 4.13.

Using reflection mode for defects with depths of 1.00mm and deeper the defect is only identified in the PPT phase data. The next deeper defect had 1.25 mm in depth.

Defect:	**1.25 mm in defect depth** **Flat bottom cylinder hole on PMMA plate**	**Reflection Mode**
Data Type	**Maximum Δ T:**	**Wavelet Denoised maximum Δ T:**
Raw data	**A** 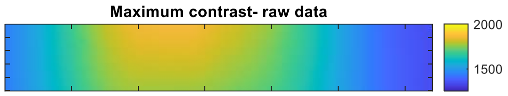	**B** 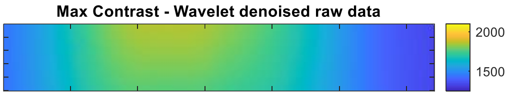
TSR data	**C** 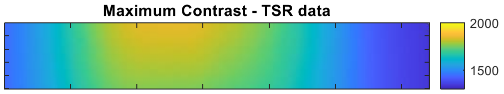	**D** 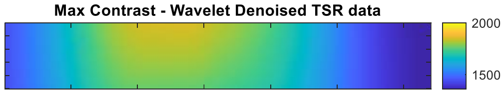
Data Type	**Maximum Δϕ:**	**Wavelet Denoised Maximum Δϕ:**
PPT data	**E** 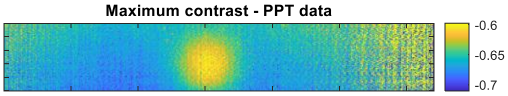	**F** 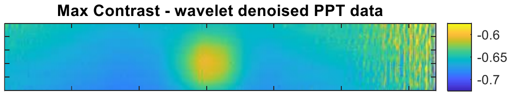

Figure 4.15. Thermal and phase images of the PMMA plate conducted in reflection mode, defect depth of 1.25mm.

Thermal images (A-D) of defect depth of 1.25 mm, as shown in Figure 4.15 did not reveal the defect.

Within the phase data results, the discussed artefacts associated with phase wrapping are visible, as shown in Figure 4.15E. These yellow artefacts are highlighted in the denoised data however the defect is also clearly identified.

Defect:	**1.50 mm in defect depth Flat bottom cylinder hole on PMMA plate**	**Reflection Mode**
Data Type	**Maximum Δ T:**	**Wavelet Denoised maximum Δ T:**
Raw data	**A** 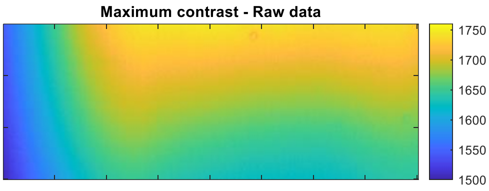	**B** 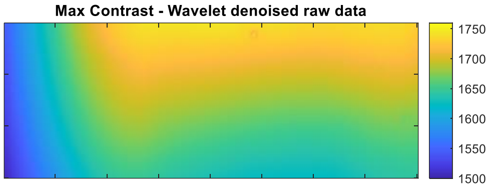
TSR data	**C** 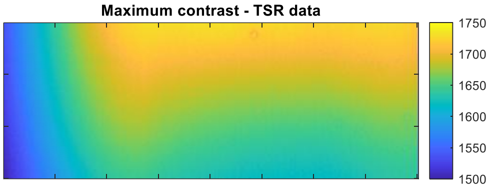	**D** 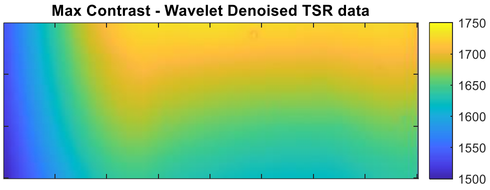
Data Type	**Maximum Δϕ:**	**Wavelet Denoised Maximum Δ ϕ:**
PPT data	**E** 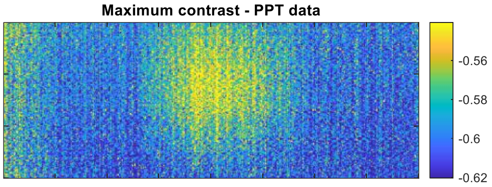	**F** 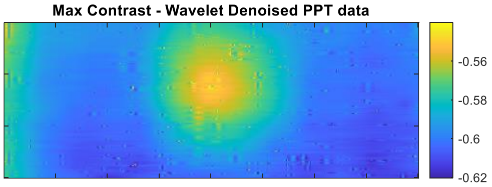

Figure 4.16. Thermal and phase images of the PMMA plate conducted in reflection mode, defect depth of 1.50mm.

Similarly with defect depth of 1.25 mm, the defect depth of 1.50 mm displayed similar results as shown in Figure 4.16. PPT processing was able to clearly detect the defect. As previously artefacts are introduced by the denoising process.

The following defects were at depths of 1.75 mm and 2.00 mm. Signal to noise ratio (SNR) decreases as defect depth increases and this is evident in the phase data.

Defect:	**1.75 mm in defect depth Flat bottom cylinder hole on PMMA plate**	**Reflection Mode**
Data Type	**Maximum Δ T:**	**Wavelet Denoised maximum Δ T:**
Raw data	**A** 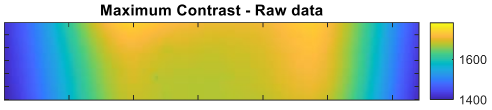 	**B** 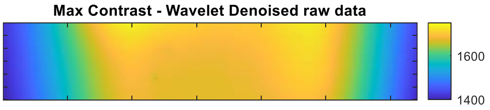
TSR data	**C** 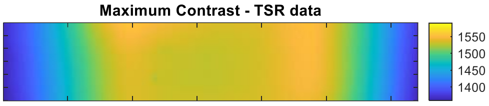 	**D** 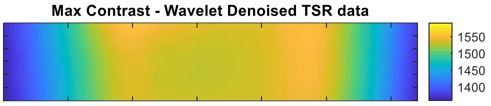
Data Type	**Maximum $\Delta\phi$:**	**Wavelet Denoised Maximum $\Delta\phi$:**
PPT data	**E** 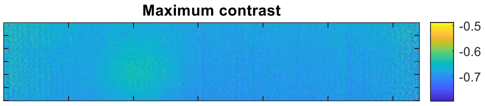 	**F** 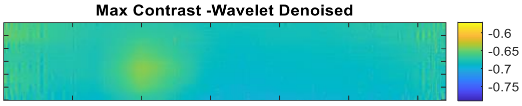

Figure 4.17. Thermal and phase images of the PMMA plate conducted in reflection mode, defect depth of 1.75mm.

The FBH defect at 1.75 mm was identifiable in reflection mode in the phase data as shown in Figure 4.17E and highlighted further in the denoised data in Figure 4.17F. However, due to the increasingly small SNR, the defect appeared with reduced contrast and less defined edges.

The deepest defect of PMMA was at defect depth of 2.00 mm, which was also detected in the phase data, as shown in Figure 4.18E and F. In Figure 4.18A-D, the defect remained undetectable in the thermal data.

Defect:	2.00 mm in defect depth Flat bottom cylinder hole on PMMA plate	Reflection Mode
Data Type	**Maximum Δ T:**	**Wavelet Denoised maximum Δ T:**
Raw data	**A** 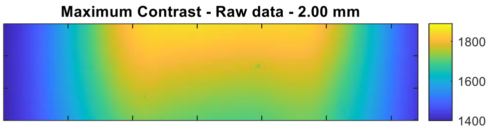 	**B** 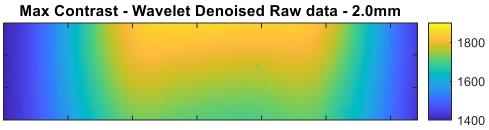
TSR data	**C** 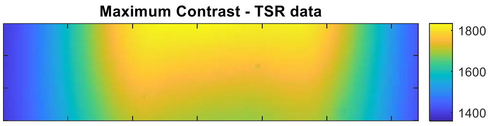 	**D** 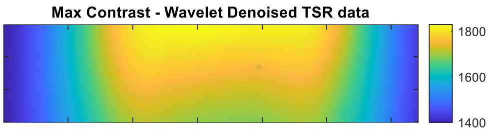
Data Type	**Maximum $\Delta\phi$:**	**Wavelet Denoised Maximum $\Delta\phi$:**
PPT data	**E** 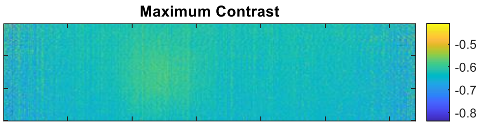 	**F** 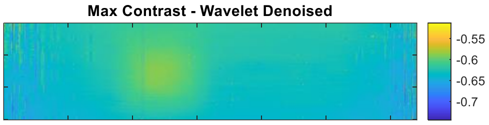

Figure 4.18. Thermal and phase images of the PMMA plate conducted in reflection mode, defect depth of 2.00mm.

The defect depth of 2.00 mm was however distinguished in phase data results. As seen in image E and F (Figure 4.17) the wavelet denoising improved the image of the defect.

Beyond 1.00 mm defect depth, it is more difficult to see clear definition of the defect in both raw and TSR data but the defects are clearly identified down to the maximum defect depth of 2.00 mm in the PPT data. Although the phase contrast is reduced for deeper defects, PPT processing was still able to be used to identify the defects. The vertical line occurred due to the camera reappeared in the set of results of defect depth of 2.00 mm, as seen in Figure 4.19.

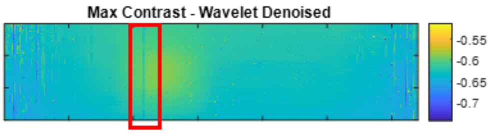

Figure 4.19. Phase image; figure F of Figure 4.18.

As for the shallower defects, both raw and TSR data results clearly identified the defects. There were no advantages in further processing into PPT data. But for deeper defects although raw and TSR data were not visibly different TSR must be carried out as a step prior to PPT processing. The contrast of defects in PPT would be reduced without the TSR process. PPT processing made significant differences in defect identification..

When comparing the same defect in both transmission and reflection mode, results of transmission typically had clearer defect identification, particularly in the thermal data. PPT revealed the defects for all depths in both transmission and reflection modes. PPT revealed the defects for all depths in both transmission and reflection modes.

Thermal data results presented had few significant differences within their images. These differences which may have resulted from various factors. Factors such as the difference in heat distributions, difference in defects' depths which affects the conduction path and power of camera flash. For an example, although the two flashes were aimed to be switched on simultaneously in reflection mode, they were not accurately synchronised in time. There is also an expected variation between the two off the shelf flashes where they may of had different intensity flash emission.

Although the developed processing steps were able to detect all defects of PMMA plate to a defect depth of 2.00 mm, in both transmission and reflection modes, the impact of temporal noise and thermal non-uniformity still effected the results.

4.2.2 Pure PLA filaments, square notches as defects

When recording thermal data, factors such as the focus of the field of view, the level of the support and the position of the camera flash (es) and/or IR camera could all influence the data collection and its analysis. These factors influenced the collected thermal images and phase images, which were used to differentiate the defective and the non-defective regions. These findings were discussed in FBH of PMMA plate and they may differ when inspecting smaller defects on curved rather than flat samples. The notched pure PLA filament samples were the first filament samples inspected.. The 1.15mm, 1.35mm, 1.55mm and 1.75mm defects were selected was because theses defect depths were all detected on PMMA plate and therefore comparable as the successive challenging set of defects. Notches will always be described according to defect depth, i.e. depth of material remaining rather than material removed.

Transmission Mode:

In Figure 4.20, the thermal and phase data obtained from the 1.15 mm notched sample is presented. This revealed that the thermal non-uniformity is less evident on filaments when compared to FBH of PMMA in transmission mode.

Defect:	**1.15 mm in defect depth Square notched defect on PLA filament**	**Transmission Mode**
Data Type	**Maximum Δ T:**	**Wavelet Denoised maximum Δ T:**
Raw data	**A** 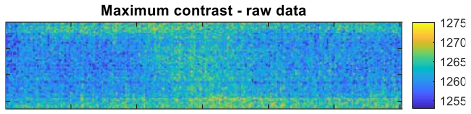 Maximum contrast - raw data	**B** 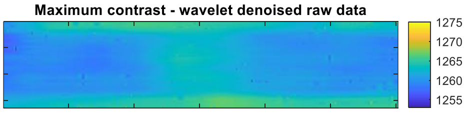 Maximum contrast - wavelet denoised raw data
TSR data	**C** 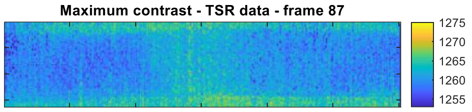 Maximum contrast - TSR data - frame 87	**D** 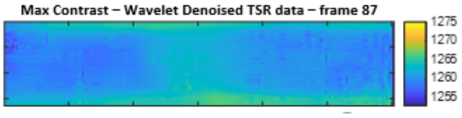 Max Contrast – Wavelet Denoised TSR data – frame 87
Data Type	**Maximum Δϕ:**	**Wavelet Denoised Maximum Δ ϕ:**
PPT data	**E** 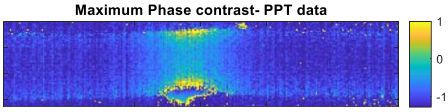 Maximum Phase contrast- PPT data	**F** 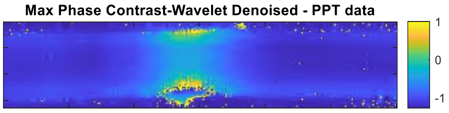 Max Phase Contrast-Wavelet Denoised - PPT data

Figure 4.20. Thermal and phase images of the single notched PLA filament, conducted in transmission mode, defect depth of 1.15mm.

The notch was distinguishable in both thermal and phase data images where is shows as a square hotspot in the middle section of the images. TSR removed a small amount of temporal noise from the raw data producing a denoised version of the data, as shown in Figure 4.20C. Spatial denoising applied to the TSR data further decreased the noise. Phase data result had the best contrast between the defect and non-defect regions. The edges of the filament are also improved in clarity, as shown in Figure 4.20E. When comparing images E and F, the wavelet denoising removed significant amount of noise.

Artefacts discussed earlier, in the previous experimental stage also reappeared, but it mostly appeared in wavelet denoised raw thermal and TSR result denoised data, B and D, but less so in the phase data, F.

The bright yellow spots appeared along the top and the bottom edges of the filament in the phase data were formed due to the tiny slivers of PLA, from the notch cutting process. These slivers of PLA were thin and heat conduction occurred at a very different rate to the remainder of the sample and so appears out of phase and presents as bright yellow spots in E and F.

Defect:	**1.35 mm in defect depth Square notched defect on PLA filament**	**Transmission Mode**
Data Type	**Maximum Δ T:**	**Wavelet Denoised maximum Δ T:**
Raw data	**A** 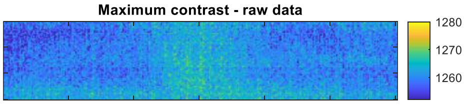 Maximum contrast - raw data 	**B** 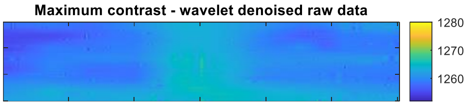 Maximum contrast - wavelet denoised raw data
TSR data	**C** 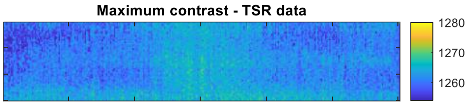 Maximum contrast - TSR data 	**D** 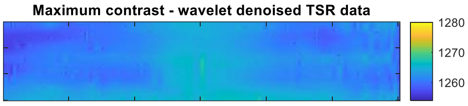 Maximum contrast - wavelet denoised TSR data
Data Type	**Maximum $\Delta\phi$:**	**Wavelet Denoised Maximum $\Delta\phi$:**
PPT data	**E** 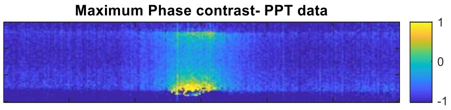 Maximum Phase contrast- PPT data 	**F** 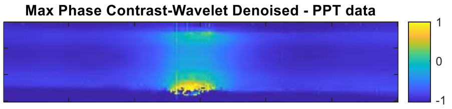 Max Phase Contrast-Wavelet Denoised - PPT data

Figure 4.21. Thermal and phase images of the single notched PLA filament, conducted in transmission mode, defect depth of 1.35mm.

For defect depths of 1.15mm and 1.35 mm, thermal images of raw and TSR data showed the same behaviours.

Defect:	**1.55 mm in defect depth Square notched defect on PLA filament**	**Transmission Mode**
Data Type	**Maximum Δ T:**	**Wavelet Denoised maximum Δ T:**
Raw data	**A** 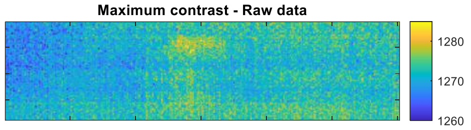 Maximum contrast - Raw data 	**B** 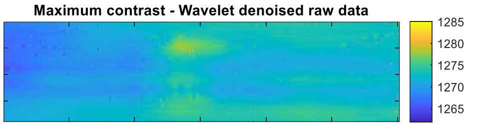 Maximum contrast - Wavelet denoised raw data
TSR data	**C** 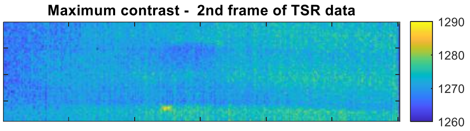 Maximum contrast - 2nd frame of TSR data 	**D** 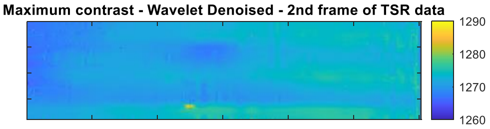 Maximum contrast - Wavelet Denoised - 2nd frame of TSR data
Data Type	**Maximum $\Delta\phi$:**	**Wavelet Denoised Maximum $\Delta\phi$:**
PPT data	**E** 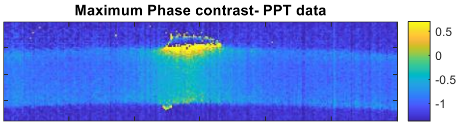 Maximum Phase contrast- PPT data 	**F** 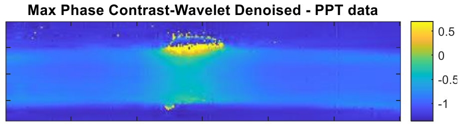 Max Phase Contrast-Wavelet Denoised - PPT data

Figure 4.22. Thermal and phase images of the single notched PLA filament, conducted in transmission mode, defect depth of 1.55mm.

Similarly with the TSR data results of defect depth of 1.35mm, the defect was identified in both thermal and phase data. Thermal images produced by TSR processing had a significant amount of improvement in terms of noise in comparison to the raw data. The phase data, images E and F were selected based on the best phase contrast, edge definition and clarity of the notch (defect). A lower contrast was recorded as is expected for deeper defects, however the notch was still well defined. The next challenging defect to be inspected was the defect with depth of 1.75mm, the deepest defect.

Defect:	**1.75 mm in defect depth Square notched defect on PLA filament**	**Transmission Mode**
Data Type	**Maximum Δ T:**	**Wavelet Denoised maximum Δ T:**
Raw data	**A** Maximum contrast - Raw data 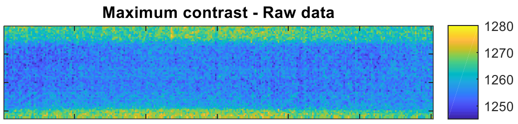 	**B** Max Contrast-Wavelet Denoised - Raw data 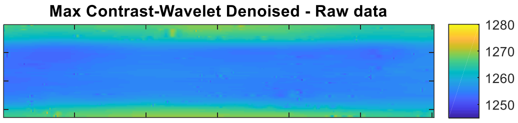
TSR data	**C** Maximum Contrast - TSR data 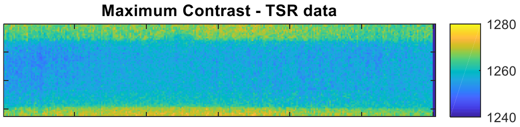 	**D** Maximum Contrast - Wavelet Denoised TSR Data 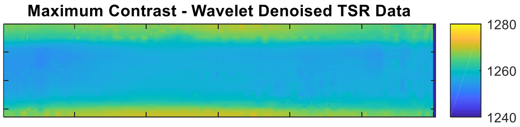
Data Type	**Maximum $\Delta\phi$:**	**Wavelet Denoised Maximum $\Delta\phi$:**
PPT data	**E** Max Phase Contrast-Wavelet Denoised - PPT data 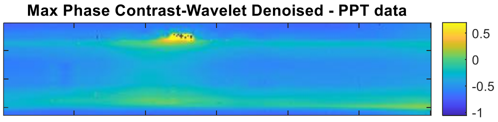 	**F** Max Phase Contrast-Wavelet Denoised - PPT data 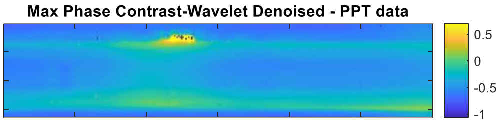

Figure 4.23. Thermal and phase images of the single notched PLA filament, conducted in transmission mode, defect depth of 1.75mm.

The notch of the defect depth of 1.75mm was not as clearly identified in the results compared to the shallower defects. This depth was therefore possibly the detection limit for a single notched filament in transmission mode.

The defective region was therefore difficult to identify (Figure 4.23). This is because the filament was only 2.00 mm thick and this defect was at 1.75 mm, therefore the difference between the defect and non-defect heat paths in minimal. A big contrast was therefore not expected in this case.

Reflection Mode:

Defect:	**1.15 mm in defect depth Square notched defect on PLA filament**	**Reflection Mode**
Data Type	**Maximum Δ T:**	**Wavelet Denoised maximum Δ T:**
Raw data	**A** 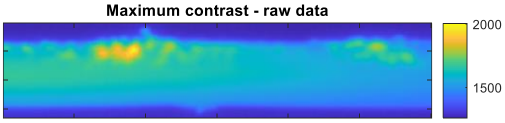	**B** 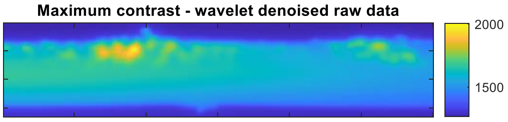
TSR data	**C** 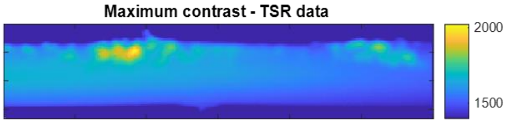	**D** 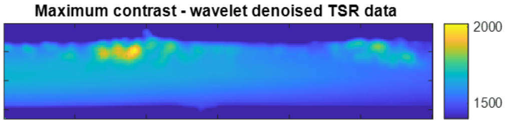
Data Type	**Maximum $\Delta\phi$:**	**Wavelet Denoised Maximum $\Delta\phi$:**
PPT data	**E** 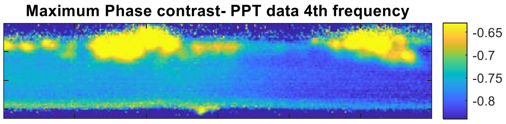	**F** 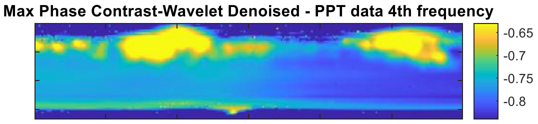

Figure 4.24. Thermal and phase images of the single notched PLA filament, conducted in reflection mode, defect depth of 1.15mm.

Among the thermal images, Figure 4.24.A-D, the impact of processing the raw data (A) using TSR to produce D was not very obvious Surface features were visible along the top edge of the filament, this may due to the accumulated spray paint spots. When matt black spray paint was sprayed onto the filament, filament surface was not completely smooth, therefore droplets of paint may have accumulated with each other and/or formed uneven paint. These features made the scaling of images more challenging to clearly reveal the defect.

Among phase images, Figure 4.24E and F, the paint effect was emphasised, seen as bright yellow regions. Results from this samples are inconclusive due to this.

Deeper defects were then assessed using reflection mode as shown in Figure 4.25, Figure 4.26 and Figure 4.27.

Defect:	**1.35 mm in defect depth Square notched defect on PLA filament**	**Reflection Mode**
Data Type	**Maximum Δ T:**	**Wavelet Denoised maximum Δ T:**
Raw data	**A** 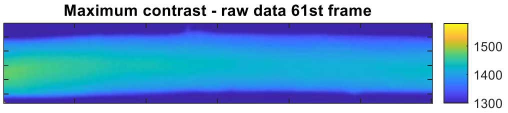 Maximum contrast - raw data 61st frame 	**B** 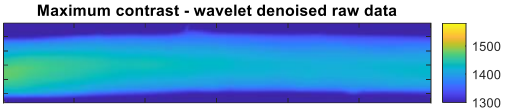 Maximum contrast - wavelet denoised raw data
TSR data	**C** 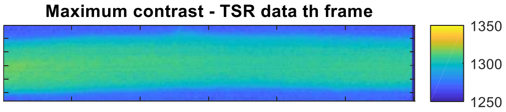 Maximum contrast - TSR data th frame 	**D** 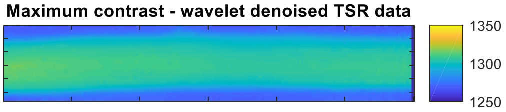 Maximum contrast - wavelet denoised TSR data
Data Type	**Maximum $\Delta\phi$:**	**Wavelet Denoised Maximum $\Delta\phi$:**
PPT data	**E** 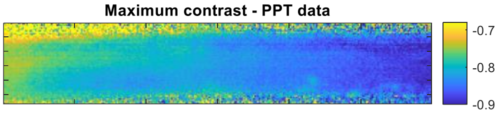 Maximum contrast - PPT data 	**F** 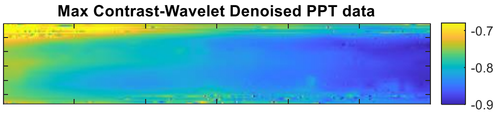 Max Contrast-Wavelet Denoised PPT data

Figure 4.25. Thermal and phase images of the single notched PLA filament, conducted in reflection mode, defect depth of 1.35mm.

Defect:	**1.55 mm in defect depth Square notched defect on PLA filament**	**Reflection Mode**
Data Type	**Maximum Δ T:**	**Wavelet Denoised maximum Δ T:**
Raw data	**A** 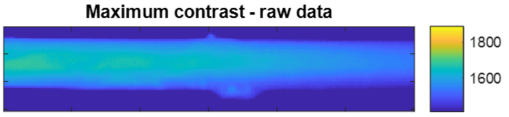 Maximum contrast - raw data 	**B** 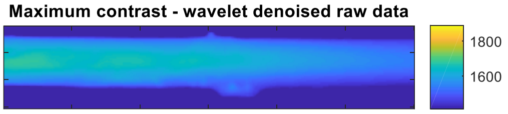 Maximum contrast - wavelet denoised raw data
TSR data	**C** 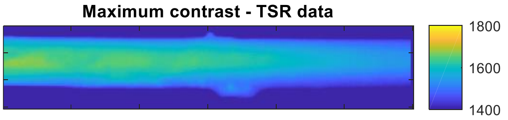 Maximum contrast - TSR data 	**D** 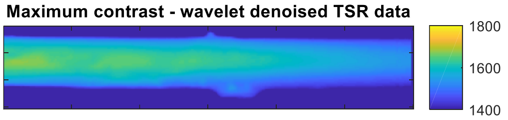 Maximum contrast - wavelet denoised TSR data
Data Type	**Maximum $\Delta\phi$:**	**Wavelet Denoised Maximum $\Delta\phi$:**
PPT data	**E** 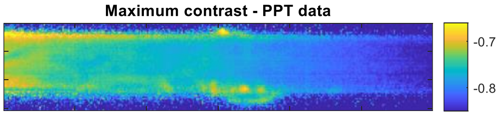 Maximum contrast - PPT data 	**F** 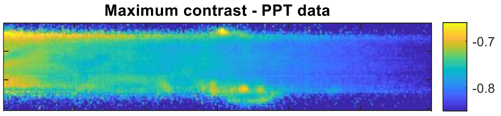 Maximum contrast - PPT data

Figure 4.26. Thermal and phase images of the single notched PLA filament, conducted in reflection mode, defect depth of 1.55mm.

Defect:	**1.75 mm in defect depth Square notched defect on PLA filament**	**Reflection Mode**
Data Type	**Maximum Δ T:**	**Wavelet Denoised maximum Δ T:**
Raw data	**A** 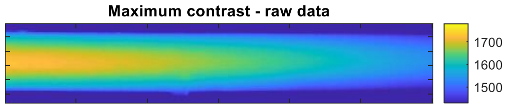 Maximum contrast - raw data 	**B** 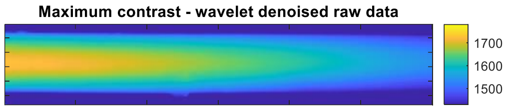 Maximum contrast - wavelet denoised raw data
TSR data	**C** 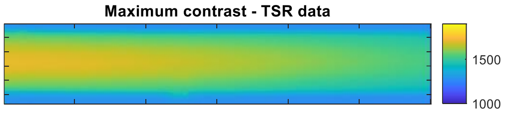 Maximum contrast - TSR data 	**D** 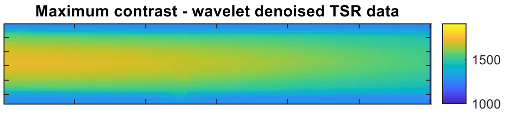 Maximum contrast - wavelet denoised TSR data
Data Type	**Maximum Δϕ:**	**Wavelet Denoised Maximum Δ ϕ:**
PPT data	**E** 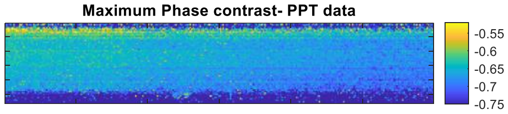 Maximum Phase contrast- PPT data 	**F** 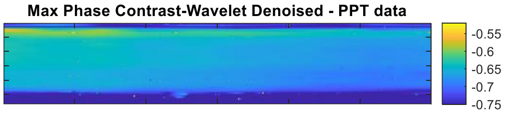 Max Phase Contrast-Wavelet Denoised - PPT data

Figure 4.27. Thermal and phase images of the single notched PLA filament, conducted in reflection mode, defect depth of 1.75mm.

In Figure 4.25, Figure 4.26, and Figure 4.27, notches were not distinguishable in raw, TSR and nor PPT data results. Although the wavelet denoise worked well for PPT data results, in which the images were clearly smoothened, notches were not seen and surface features shown in the 1.55 mm sample heavily influence results, as shown in Figure 4.26. Therefore, the notches were not detectable with the current setup in reflection mode. This is due to the distance between the heat source and the sample surface was increased due to the setup's restrictions therefor insufficient heat was applied to the sample. However, reflection mode will still be used on subsequent samples as it is likely to detect near surface samples more clearly than transmission.

4.2.3 PLA filaments with NaCl (salt) particles

PLA filaments were manufactured containing 2wt% and 5wt% of NaCl were to be discussed in this section. The NaCl crystals provided defects that were smaller than the notches and distributed at random throughout the filaments. The salt particles provided a defect of intermediate difficulty when compared to Harakeke reinforced polymer composites filaments that this project had the goal of.

Transmission Mode:

Samples were first inspected in transmission mode. The intended defects are the salt particles. The first sample tested was the 2wt% sample shown in Figure 4.28.

Defect:	**2wt% NaCl mixed with PLA NaCl particles- defect within PLA filament**	**Transmission Mode**
Data Type	**Maximum Δ T:**	**Wavelet Denoised maximum Δ T:**
Raw data	**A** 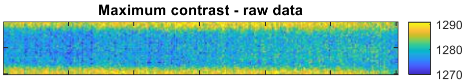 	**B** 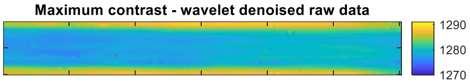
TSR data	**C** 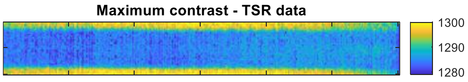 	**D** 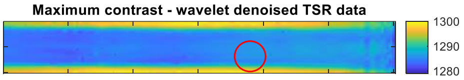
Data Type	**Maximum $\Delta\phi$:**	**Wavelet Denoised Maximum $\Delta\phi$:**
PPT data	**E** 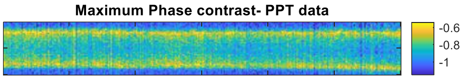 	**F** 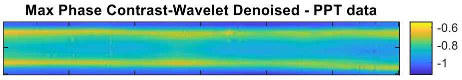

Figure 4.28. Thermal and phase images of the single notched PLA filament, conducted in transmission mode, 2wt% NaCl particles as defects.

Among raw, TSR and phase data, as shown in Figure 4.28A, C and E, it was not possible to identify the NaCl particles. However, spatially denoised versions of these data (B, D and F) had great amount of high frequency noise reduced by wavelet denoising. In the denoised data there were few visible dark and white spots shown on in images B, D and F, but it cannot currently be said with certainty whether these spots were salt particles or not. Further investigation would be needed.

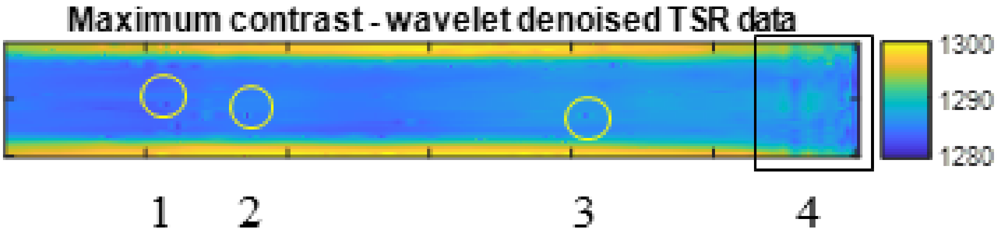

Figure 4.29. Enlarged version of Figure 4.28D, Wavelet denoised TSR data result. Defect: 2.0wt% NaCl mixed with PLA filament.

An enlarged version of Figure 4.28D is provided in Figure 4.29. In this particular thermal image, labels 1, 2, and 3 also highlight features of interest. In the current work it is not clear is the highlighted features are salt or are artefacts formed to due to wavelet denoising as discussed previously. The feature marked with 4, as was present in both pre and post denoised data is an artefact of the camera and requires further investigation.

The edges of the filaments had brighter yellow strips in PPT phase data results, the same effect is seen by the edges of the filament being lights (hotter) in the thermal data. Please see the illustration in Figure 4.30. This diagram illustrated how heat propagated through the cross-sectional area of filament, which was used to accompany the bright edges effect in Figure 4.29. The heat propagated through less material at the edges of filament when compared to its centre. This was mostly driven by thermal conduction of the material and different heat paths were therefore dependent on the thickness. Brighter and warmer colours were therefore mapped at the top and bottom edges of phase images, see in E, F of Figure 4.31, where the filament was thinner.

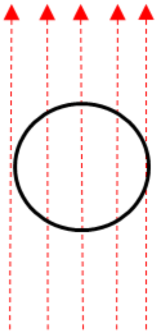

Figure 4.30. Cross sectional area of a filament with arrows indicating heat flow.

Defect:	**5wt% NaCl mixed with PLA NaCl particles- defect within PLA filament**	**Transmission Mode**
Data Type	**Maximum Δ T:**	**Wavelet Denoised maximum Δ T:**
Raw data	**A** 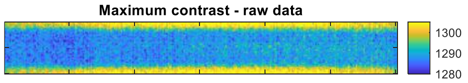	**B** 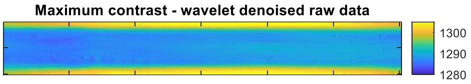
TSR data	**C** 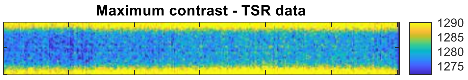	**D** 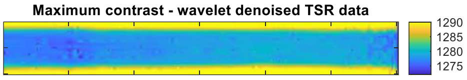
Data Type	**Maximum $\Delta\phi$:**	**Wavelet Denoised Maximum $\Delta\phi$:**
PPT data	**E** 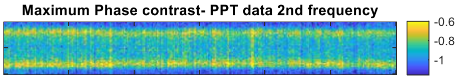	**F** 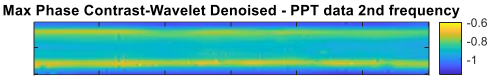

Figure 4.31. Thermal and phase images of the single notched PLA filament, conducted in transmission mode, 5wt% NaCl particles as defects.

Similarly with the results of 2wt% NaCl mixed PLA, no salt particle was distinguished in the 5wt% as shown in Figure 4.31. It was not possible to detect the salt particles clearly in transmission mode. The qualitative collection of imaging results require further image enhancement, noise reconstruction to reveal the salt particles.

Reflection Mode:

The 2wt% NaCl sample was then inspected in reflection mode as shown in Figure 4.32.

Defect:	**2wt% NaCl mixed with PLA NaCl particles- defect within PLA filament**	**Reflection Mode**
Data Type	**Maximum Δ T:**	**Wavelet Denoised maximum Δ T:**
Raw data	**A** 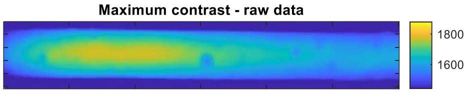	**B** 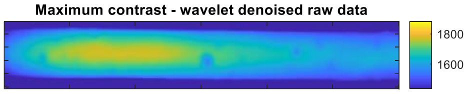
TSR data	**C** 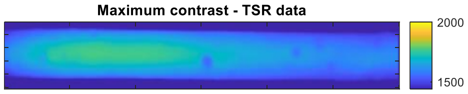	**D** 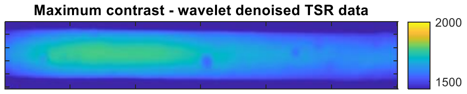
Data Type	**Maximum $\Delta\phi$:**	**Wavelet Denoised Maximum $\Delta\phi$:**
PPT data	**E** 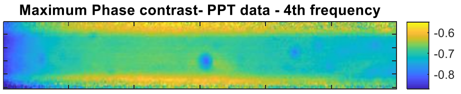	**F** 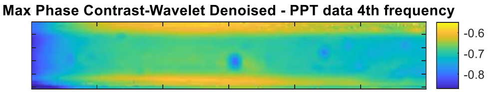

Figure 4.32. Thermal and phase images of the single notched PLA filament, conducted in reflection mode, 2wt% NaCl particles as defects.

In Figure 4.32, A, B, C and D were the thermal images resulted from raw and TSR data. Salt particles were identified, in the raw data shown in Figure 4.32 A as highlighted in Figure 4.33.

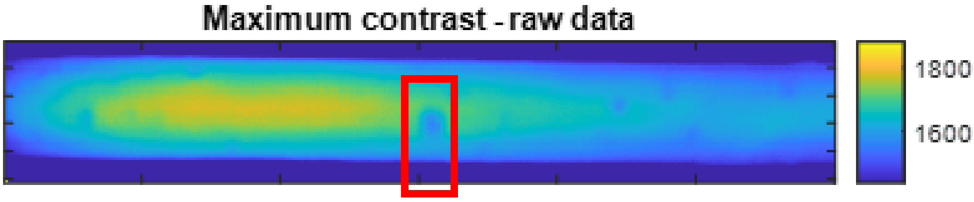

Figure 4.33. Enlarged Figure 4.32A, raw thermal image.

There were clear features seen in reflection mode, represented by the several dark spots scattered in Figure 4.32. In addition to that, these dark spots were present in both thermal and phase images, A-F (Figure 4.32). It is likely as these features are seen in the raw thermal data that they are near surface, however the exact depth of the identified salt particles would need further investigation.

Among raw images of Figure 4.32, A and B, thermal non-uniformity was obvious. Although the setup was systematically set up, the height and the positioning of two independently separated camera flashes would not be precisely the same and this was obvious in this case. In addition, the IR camera was collecting data in units of microns, a slightest movement may influence the visualisation of the defect inspections.

Although the level of setup was kept level some filaments had more of a curvature which was not entirely eliminated by the sample holder. This may have also fed into the non-uniform heating.

Defect:	**5wt% NaCl mixed with PLA NaCl particles- defect within PLA filament**	**Reflection Mode**
Data Type	**Maximum Δ T:**	**Wavelet Denoised maximum Δ T:**
Raw data	**A** 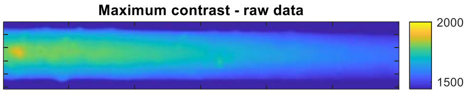 Maximum contrast - raw data 	**B** 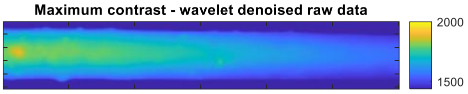 Maximum contrast - wavelet denoised raw data
TSR data	**C** 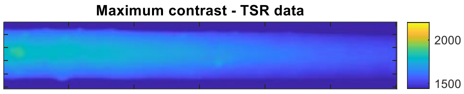 Maximum contrast - TSR data 	**D** 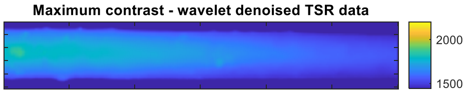 Maximum contrast - wavelet denoised TSR data
Data Type	**Maximum $\Delta\phi$:**	**Wavelet Denoised Maximum $\Delta\phi$:**
PPT data	**E** 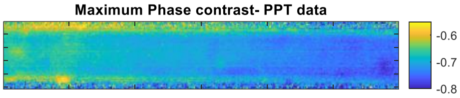 Maximum Phase contrast- PPT data 	**F** 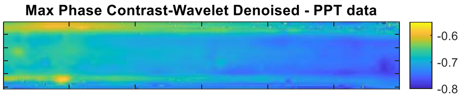 Max Phase Contrast-Wavelet Denoised - PPT data

Figure 4.34. Thermal and phase images of the single notched PLA filament, conducted in reflection mode, 5wt% NaCl particles as defects.

The definition of salt particles were much less defined in 5wt% than in 2wt% data results although some features are still present in both raw and denoised thermal data as well as other datasets. In this group of results, thermal data A-D also displayed effects of non-uniform heating this made it more difficult to positively identify the defects. The impact of non-uniform heating is reduced in the phase data Figure 4.34E and F and show better edge definition and more surface details. Wavelet denoising continued to reduce high frequency noise in the phase data.

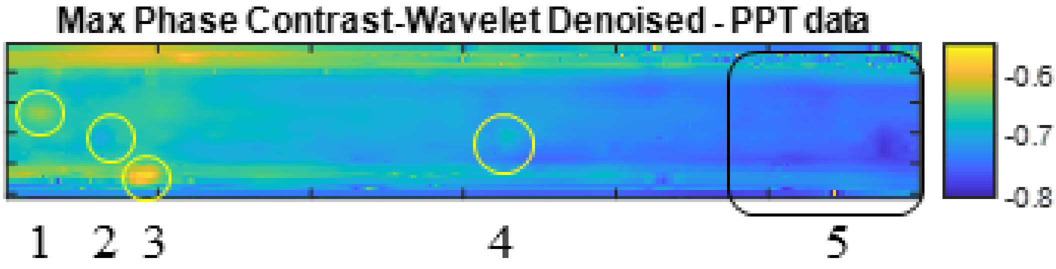
Max Phase Contrast-Wavelet Denoised - PPT data

Figure 4.35. Wavelet denoised PPT image, phase data. Image F of Figure 4.34. Features are numbered 1 to 5.

In Figure 4.35, Feature 1 is noted as the marker used for alignment, Features 2 to 4 could be subsurface details as they were not seen in images A-D. Features (1-5) could be surface defects or sub-surface defects, which appeared in either darker or lighter spots. The types of defects were not clearly identified at this stage.

NaCl particles of transmission mode were not as distinguishable as in reflection mode, which is expected when considering the total impact of passing through a small defect will have compared to the total thickness of the samples. However, the non-uniformity in filaments may also contributed to the results, i.e. 5wt% NaCl mixed PLA filament had diameters that were less uniform when compared to 2wt% NaCl mixed PLA filament.

Reflection mode was a good setup for detecting the surface and near-surface textures/features. At this stage it would require further investigation to confirm exactly how deep salt particles could be detected.

4.2.4 PLA mixed with coarse harakeke fibres

Coarse and unpulped harakeke fires were untreated and larger when compared to treated harakeke fibres, these fibres were therefore selected to mix with PLA as large fibre defects for inspection experiments. Untreated fibres are fibre bundles, which are approximately 200 microns in width were investigated and shown in Figure 4.36.

Transmission Mode:

Defect:	**0.125wt% Harakeke mixed with PLA Fibre - defect within PLA filament**	**Transmission Mode**
Data Type	**Maximum Δ T:**	**Wavelet Denoised maximum Δ T:**
Raw data	**A** 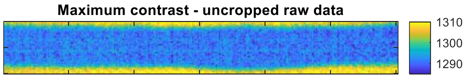 Maximum contrast - uncropped raw data	**B** 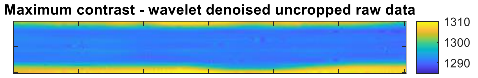 Maximum contrast - wavelet denoised uncropped raw data
TSR data	**C** 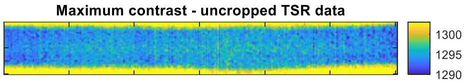 Maximum contrast - uncropped TSR data	**D** 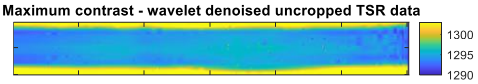 Maximum contrast - wavelet denoised uncropped TSR data
Data Type	**Maximum $\Delta\phi$:**	**Wavelet Denoised Maximum $\Delta\phi$:**
PPT data	**E** 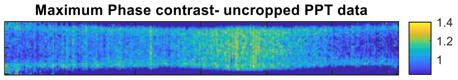 Maximum Phase contrast- uncropped PPT data	**F** 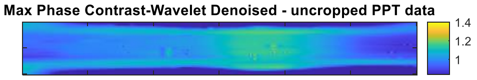 Max Phase Contrast-Wavelet Denoised - uncropped PPT data

Figure 4.36. Thermal and phase images of the single notched PLA filament, conducted in transmission mode, 0.125wt% Harakeke mixed with PLA.

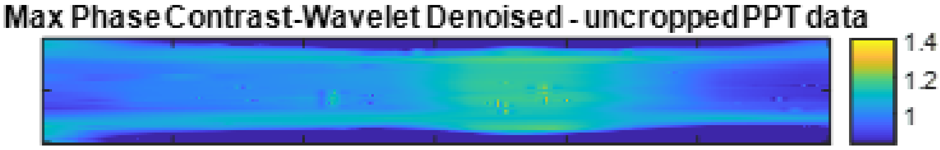

Figure 4.37. Image F of Figure 4.36.

The bulged region appeared in thermal and phase images were the intended defective region, as shown in Figure 4.37. The wavelet denoised phase result later confirmed the overall shape and size of the defective region. The shape and structure might be due an air bubbled formed during hot extrusion of filaments or the flow of polymer around the fibres being restricted. Adding a small amount of coarse harakeke fibres into PLA appeared to cause an increase in diameter variability and harakeke fibres appeared to preferentially be located at the filament surface. This was not idea for this experiment. The identification of the defective region was confirmed by comparing the photographic images, which were taken before spray painted the filament. Prior to painting the filament for infrared thermography (IRT), a section of FOV was photographed for references:

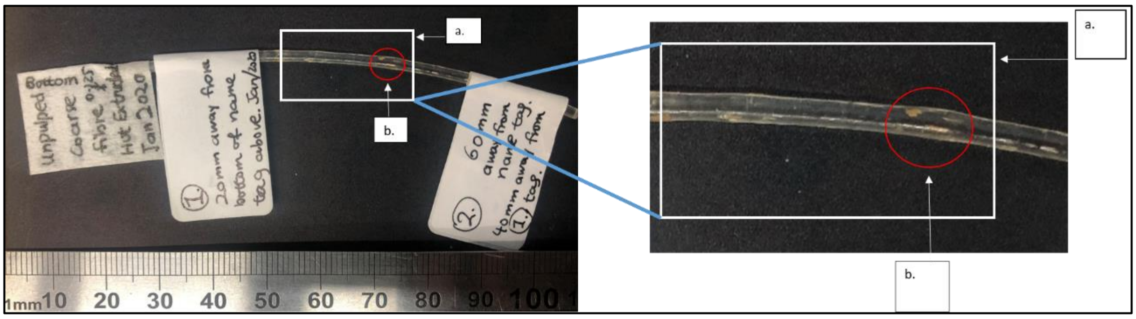

Figure 4.38. Hot extruded PLA filament mixed with 0.125wt% coarse and unpulped Harakeke fibre. a. the section of inspection, b. the intended defective region.

Figure 4.38 was used as a reference to aid the defect-inspection of 0.125wt% untreated Harakeke mixed PLA. The field of view (FOV) section was noted by a. The location of a coarse bundle was noted by b., which was visible within the original transparent filament. The defective region b. was confirmed by the infrared thermography inspections, which indicated thermography could identify coarse fibre at its current depth. Sample's edges were always the first to be detected, but it could be misled. This was because the filaments were not completely straight, smooth and in diameters. As discussed in earlier experimental stage, the surface and near-surface features were easy to detect but from the current sample deeper defects were not available.

Figure 4.39 presents the results from the transmission mode inspection for the 0.5wt% coarse Harakeke sample.

Defect:	**0.50wt% Harakeke mixed with PLA** **Fibre - defect within PLA filament**	**Transmission Mode**
Data Type	**Maximum Δ T:**	**Wavelet Denoised maximum Δ T:**
Raw data	**A** 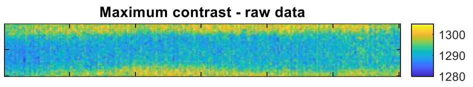 	**B** 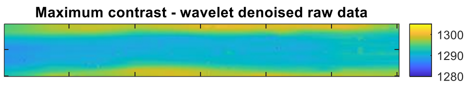
TSR data	**C** 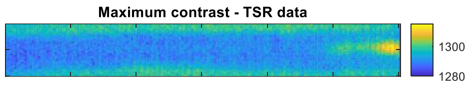 	**D** 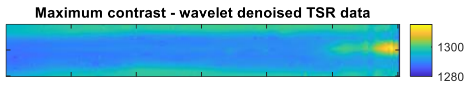
Data Type	**Maximum Δϕ:**	**Wavelet Denoised Maximum Δ ϕ:**
PPT data	**E** 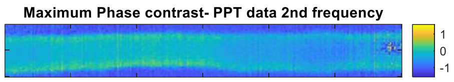 	**F** 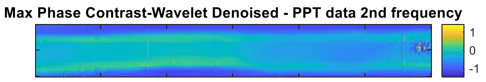

Figure 4.39. Thermal and phase images of 0.50wt% Harakeke mixed PLA, collected in transmission mode.

In the raw thermal data of 0.5wt% coarse harakeke mixed PLA, Figure 4.39A and B, the overall shape of filament was evident, however no visible defects or features were identified. Within the TSR processed data, results C and D, a bright yellow patch appeared at the right-hand side of the filament. The yellow patch was caused by missing paint, which made this particular region of the filament more reflective compared to the rest of the filament. The yellow patch decreased when processed into phase data, as shown in E and F. This suggested that the variation of emissivity across the surface will hinder the defect inspections in IRT if not corrected for. Further work would be needed to quantify the impact of emissivity variations on filament samples.

Reflection Mode:

0.125wt% coarse fibre filament was then inspected in reflection mode and results are presented in Figure 4.40.

Defect:	**0.125wt % Harakeke mixed with PLA Fibre - defect within PLA filament**	**Reflection Mode**
Data Type	**Maximum Δ T:**	**Wavelet Denoised maximum Δ T:**
Raw data	**A** 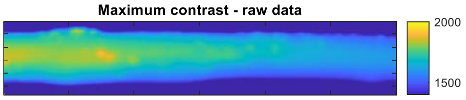 	**B** 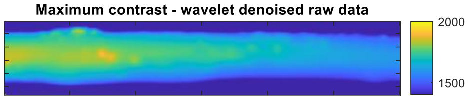
TSR data	**C** 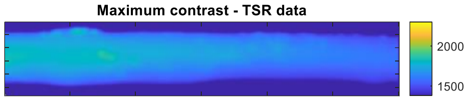 	**D** 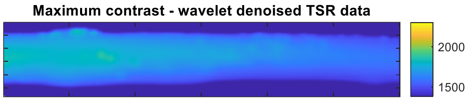
Data Type	**Maximum $\Delta\phi$:**	**Wavelet Denoised Maximum $\Delta\phi$:**
PPT data	**E** 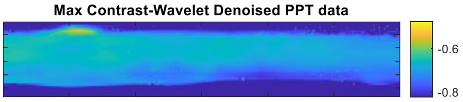 	**F** 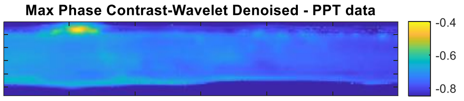

Figure 4.40. Thermal and phase images of the single notched PLA filament, conducted in reflection mode, 0.125wt% Harakeke mixed with PLA.

As previously discussed, alignment of the sample was not 100% and the left hand side of the filament was slightly closer to the heat source, it was therefore brighter compared to the right hand side of the filament. In Figure 4.40, the bulge region containing defects was detected towards the left of the FOV however this is due to the change in geometry of the specimen, not the thermal detection. . Figure 4.40C and D show the camera noise was improved through noise reduction of TSR processing.

Phase data in Figure 4.40E was processed into wavelet denoised data shown in Figure 4.40F. In image F, the left hand side of the filament was seemly brighter than the left and this might be due to the experimental set up. Similar reasoning was given in transmission mode (Figure 4.36). Within Figure 4.40 there are some local variations along the filament however it was not interrogated further to be able to conclusively identify these features.

The 0.5wt% coarse fibre sample was next investigated in reflection mode as shown in Figure 4.41. As with the transmission data for this sample, no clear defects were identified in either thermal or phase data.

Defect:	0.5wt % Harakeke mixed with PLA Fibre - defect within PLA filament	Reflection Mode
Data Type	**Maximum Δ T:**	**Wavelet Denoised maximum Δ T:**
Raw data	**A** 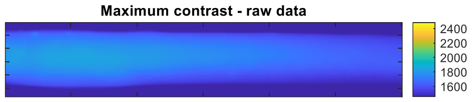 	**B** 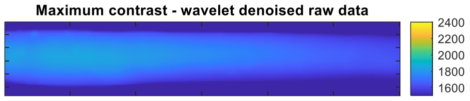
TSR data	**C** 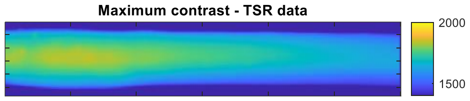 	**D** 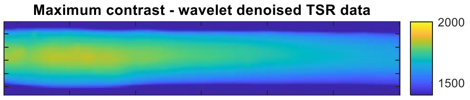
Data Type	**Maximum $\Delta\phi$:**	**Wavelet Denoised Maximum $\Delta\phi$:**
PPT data	**E** 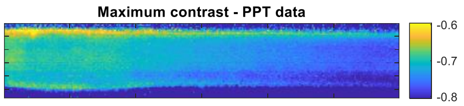 	**F** 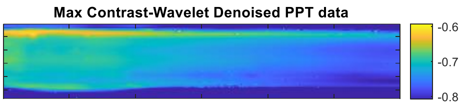

Figure 4.41. Thermal and phase images of the single notched PLA filament, conducted in reflection mode, 0.5wt% Harakeke mixed with PLA.

4.2.5 Polymers with fine harakeke fibres

Harakeke (fine) fibres reinforced polymers were the last two samples to be inspected; 10wt% harakeke fibre reinforced PLA and 30wt% harakeke fibre reinforced PP.

Harakeke fires were treated prior reinforcing the matrix material PLA or PP. For 10wt% harakeke fibre reinforced PLA, fibre's diameter was recorded to be $12.3 \pm 1.7\ \mu$m, which was the measurement taken after treating fibres [25]. For 30wt% harakeke fibre reinforced PP, the diameter of treated fibre was not recorded [116]. Fibre bundles or air bubbles were anticipated defects in these samples.

Within the data collected 300 pixels were recorded to view 20mm in filament length. This meant that one pixel was 70 micrometres, which was more than five times larger than a fibre. This conversion implemented that it was impossible to detect a single fibre at this stage of the research project. In this section regions of change of thermal properties are of interest, rather than individual fibres.

Defects of interest to 3D printing would be air bubbles or voids, the change in diameters and fibre bundles (local regions of change of thermal properties) that were much larger than 13 micrometres.

Transmission Mode:

The 10wt% Harakeke sample was the first to be inspected, shown in Figure 4.42.

Defect:	**10wt% Harakeke mixed with PLA Fibre - defect within PLA filament**	**Transmission Mode**
Data Type	**Maximum Δ T:**	**Wavelet Denoised maximum Δ T:**
Raw data	**A** 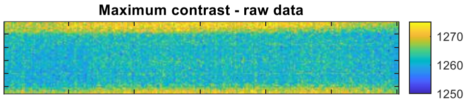	**B** 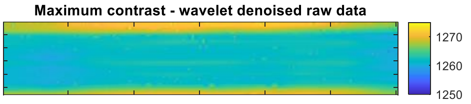
TSR data	**C** 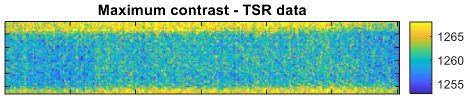	**D** 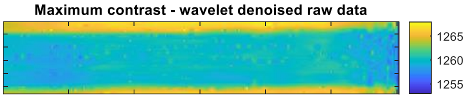
Data Type	**Maximum $\Delta\phi$:**	**Wavelet Denoised Maximum $\Delta\phi$:**
PPT data	**E** 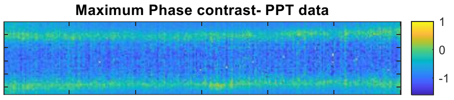	**F** 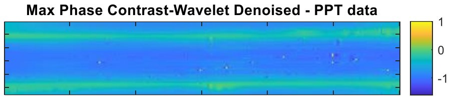

Figure 4.42. Thermal and phase images of treated harakeke fibre reinforced PLA, conducted in transmission mode, 10wt% Harakeke.

In Figure 4.42, raw thermal data in A and B did not reveal any features. TSR data presented in C and D began to show some ‘texture’ in the image but nothing conclusive was identified.

Phase data in E and F had the two bands reappeared along the top and bottom edges of the filament, as discussed for Figure 4.28, 2wt% NaCl mixed PLA in transmission. This effect was explained by Figure 4.30, which illustrated that the heat conducting path and thermal conduction of the material were depended on the thickness of the materials. The small amount of texture was visible in the phase data also, although again conclusive identification of the cause of this would require further work.

The higher weight percent sample was then inspected in transmission mode as shown in Figure 4.43.

Defect:	30wt% Harakeke mixed with PLA Fibre - defect within PP filament	Transmission Mode
Data Type	**Maximum Δ T:**	**Wavelet Denoised maximum Δ T:**
Raw data	**A** 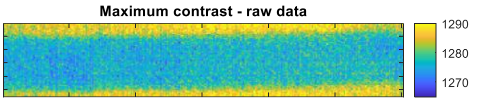	**B** 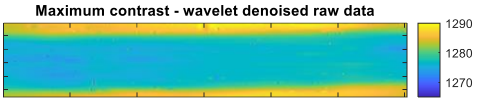
TSR data	**C** 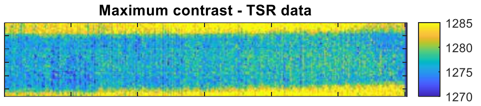	**D** 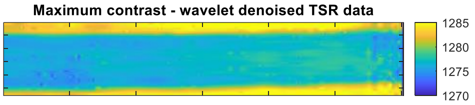
Data Type	**Maximum $\Delta\phi$:**	**Wavelet Denoised Maximum $\Delta\phi$:**
PPT data	**E** 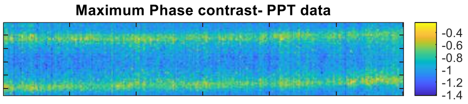	**F** 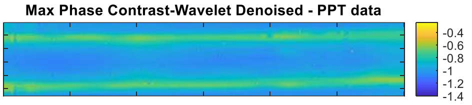

Figure 4.43. Thermal and phase images of treated harakeke fibre reinforced PP, conducted in transmission mode, 30wt% Harakeke.

Raw data results did differ from those collected in Figure 4.42. No significant features were highlighted using the transmission mode on the fine Harakeke reinforced filaments. TSR data sets across the two samples as in Figure 4.44.

Defect comparison:	10wt% and 30wt% Harakeke mixed with PLA and PP	Transmission Mode
Data Type	**Maximum Δ T:**	**Wavelet Denoised maximum Δ T:**
TSR data of 10wt%	**C** 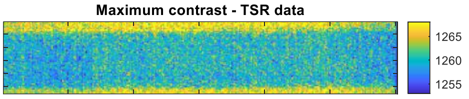	**D** 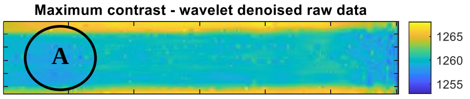
TSR data of 30wt%	**C** 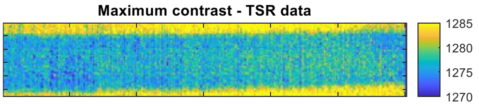	**D** 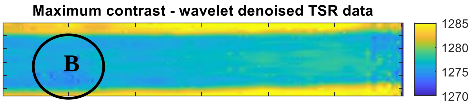

Figure 4.44. Thermal (TSR) images of treated harakeke fibre reinforced PLA, conducted in transmission mode, 10wt% Harakeke.

A, B regions labelled in Figure 4.44 were TSR thermal images of 10wt% harakeke reinforced PLA and 30wt% harakeke reinforced PP respectively. The two regions labelled A and B were found to have a similar pattern, although they were not the same samples. This indicated that some of features in these datasets were introduced due to the data collection process and equipment rather than the samples. It is noted that the range plotted on the filament transmission samples is very small, so these introduced features are very small. This also means that any feature caused by features of the sample are approaching the noise level of this setup. Further work could explore methods of reducing this noise level to quantify the limits of detection in transmission mode using the present setup.

Reflection Mode:

The fine fibre samples were then inspected in reflection mode. The 10wt% sample is shown in Figure 4.45.

Defect:	**10wt% Harakeke mixed with PLA**	**Reflection Mode**
Data Type	**Maximum Δ T:**	**Wavelet Denoised maximum Δ T:**
Raw data	**A** 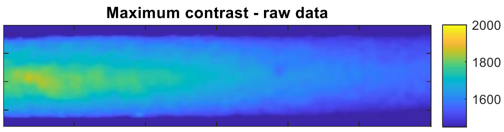	**B** 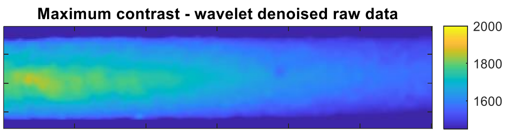
TSR data	**E** 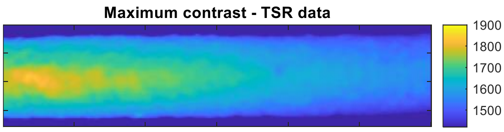	**D** 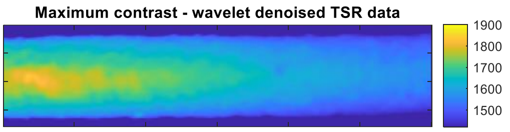
Data Type	**Maximum $\Delta\phi$:**	**Wavelet Denoised Maximum $\Delta\phi$:**
PPT data	**E** 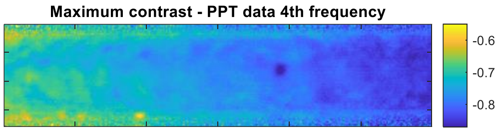	**F** 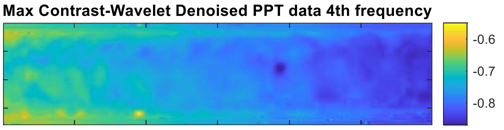

Figure 4.45. Thermal and phase images of treated harakeke fibre reinforced PLA, conducted in reflection mode, 10wt% Harakeke.

This filament had rough texture, which was detected, as shown in Figure 4.45 in both thermal and phase data. In thermal data, Figure 4.45A-D, it is unclear which features are surface information and which provide subsurface information. However, by assessing multiple frequencies in the phase data it is possible to provide confidence that some of this information is from the subsurface, where phase data from different frequencies is able to interrogate different depths. Examples of phase images correlating to different frequencies are given in Figure 4.46.

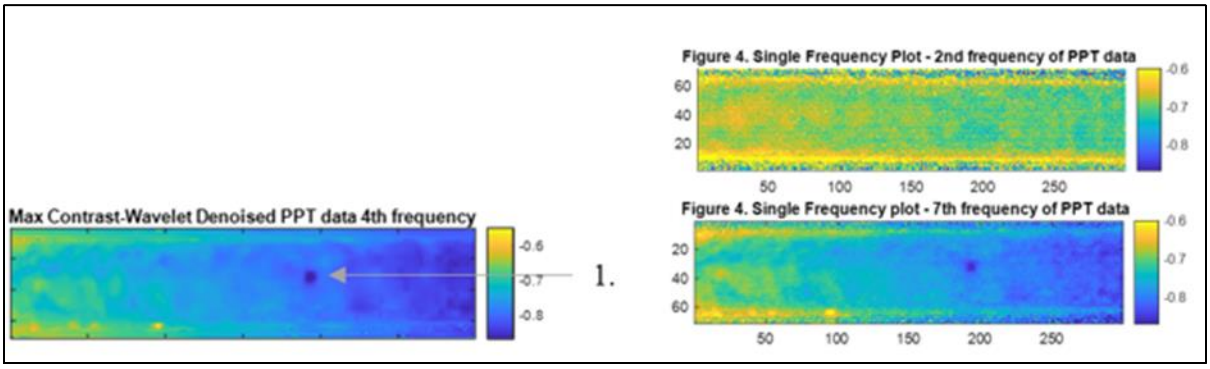

Figure 4.46. Phase image: image F of Figure 4.45. Feature 1, the dark spot, plotted at different frequencies; from left to right, the 4th, the 2nd and the 7th frequency orders.

The dark spot highlighted as feature 1 in Figure 4.46 was most likely to be a void because it was not seen on material's surface and it has a strong thermal contrast so is easily detected in the thermal data in Figure 4.45 also the sizing was only very approximate (about 6 pixels, which were about 0.4 mm) as the depth was unknown. Other inspection method or destructive testing could be used to confirm the depth of this void.

The final sample inspected was the 30wt% Harakeke reinforced filament as shown in Figure 4.47.

Defect:	**30wt% Harakeke mixed with PP Fibre - defect within PLA filament**	**Reflection Mode**
Data Type	**Maximum Δ T:**	**Wavelet Denoised maximum Δ T:**
Raw data	**A** 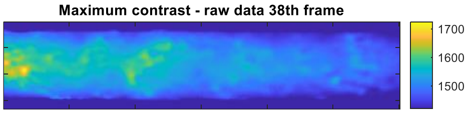	**B** 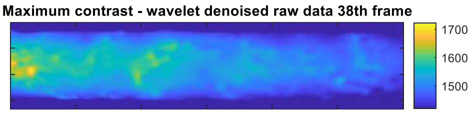
TSR data	**C** 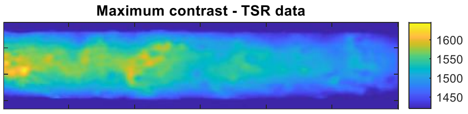	**D** 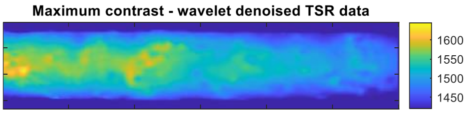
Data Type	**Maximum Δϕ:**	**Wavelet Denoised Maximum Δ ϕ:**
PPT data	**E** 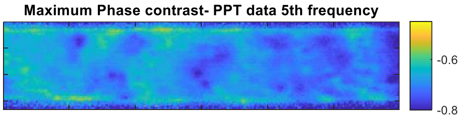	**F** 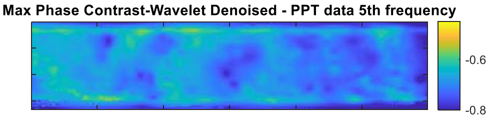

Figure 4.47. Thermal and phase images of treated harakeke fibre reinforced PP, conducted in reflection mode, 30wt% Harakeke.

The texture in the thermal and phase images was again clearly shown in Figure 4.47. Image F had some indication of defects, which was plotted from PPT phase data at 5th frequency, enlarged in Figure 4.48. Similarly to the 10wt% filament by assessing the phase data at multiple frequencies it is possible to confirm that these feature are caused by surface and subsurface information.

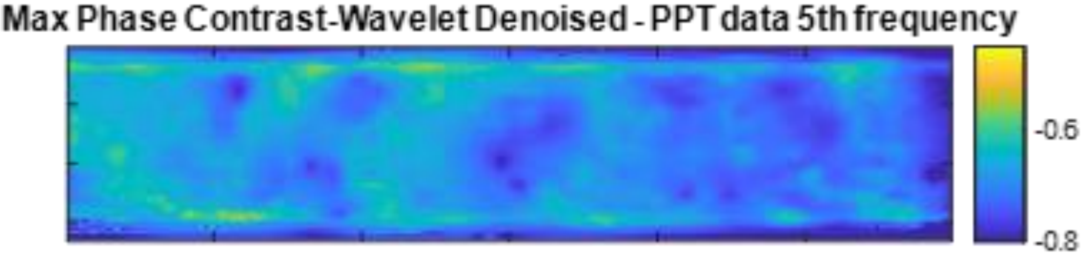

Figure 4.48. Phase image F, from Figure 4.47.

Comparing between the samples the amount of texture increases with the amount of reinforcement, however further research is required to identify the sensitivity of this and to confirm if this could enable a small-scale increased weight percent (i.e. a fibre bundle) to be detected.

Chapter 5

Conclusion

5.1 Evaluation of the defects

Various samples were analysed using IR thermography. The associated phenomena observed in both transmission and reflection modes were obtained and evaluated in either the time domain or the frequency domain.

The defects were distinguishable due to different heat propagations through defective and non-defective regions. Thermal and phase contrast images were plotted for visualisation. The thermal contrast peak decayed as the defect depth increased, this was as expected because the thermal front weakens due to the diffusion effect.

In certain situations, the defect was identifiable in the raw thermal data. This was typically with very shallow defects. Corrections were made to address noise such as temporal noise and systematic errors such as different flash power in reflection mode of the experimental stage. Repetitions of data collection and control of the stability of experimental setup were significant factors impacting the reliability of data. The quality of recordings was as consistent as possible. The setup was constantly controlled for each sample, this was to minimise the sources of error. The heat should ideally be evenly distributed across the sample, but according the results, this was not always achieved in the current research.

Wavelet denoising reduced the high frequency spatial noise. TSR was applied through time per pixel, which reduced the temporal noise in the data. TSR was used as the input for PPT processing. Both raw data and TSR processed data produced thermal images. PPT has been shown to greatly remove features such as non-uniform heating. PPT was shown to reveal deeper defects that were not visible in TSR and raw data such as in Figure 4.29. for the 2.0wt% NaCl with PLA filament.

PPT processing produced the phase images that detected the surface, near surface and certain subsurface features of the samples. PPT processing in turn has revealed the most of defects information.

Phase wrapping was a phenomenon that can occur at any frequency, it was therefore present in some phase images. Phase wraps were the 2π jumps occurred in data [117].

Wavelet transform (denoising) made significant impact on PPT phase data images, in which it achieved in both noise reduction and feature preservation, as demonstrated in Figure 4.36F, for the 0.125wt% harakeke mixed with PLA filament.

There was a balance between noise reduction and smoothing, this was to ensure the signals were not removed, nor losing important information.

The developed processing procedures were able to detect all FBH defects of PMMA plate, in both transmission and reflection modes. In transmission mode, the flash heating and IR camera were positioned closer to the sample, and more direct heating was applied than in reflection mode. The defects were therefore easier to identify in transmission mode (for FHB). Non-uniform heating was the main reason for the non-uniform colours in FBH's surrounding regions.

Surface and near-surface details were more distinguishable when comparing PPT phase and the thermal results of the filaments. Different frequencies were tested during the PPT analysis. This was to investigate at which depth the defect can be probed with current IRT technique.

Surface features occurred when spray paint droplets were accumulated, either with each other, causing surface features which could mask fainted subsurface information, particularly in reflection mode. It is noted that the process of spray painting, while useful for method development is not practical for implementation.

For the filament samples, IRT was able to detect the surface and near-surface features using reflection mode. The current infrared thermography techniques was able to detect all 2 mm depth of pure polymers (PMMA and PLA) in transmission mode regardless of front surface curvature. Notches were not revealed in reflection mode. The heat path propagated was dependent on experimental mode of data collection; either in transmission or reflection mode. The heating stimulus was more focused on sample defects when in transmission mode. Whereas in reflection mode, the sample surface was further away from the flash heating, which was emitted at 45 degrees to the horizontal plane.

Data in reflection mode has indicated that the subsurface defects may exist within the inspected samples but were not detectable in reflection mode particularly if they are at depths of more than half the thickness of the sample as was the case with the notches.

For pure polymer samples (notched PLA filaments), the deepest defect detected was at notch depth of 1.75 mm. For polymer composites (salt or harakeke fibres mixed polymer filaments), some of the surface and near-surface features were detected, but the exact defect depths were unidentifiable at this stage. Although the overall shapes and/or sizes of few defects were revealed, salt particles and air bubble/void as such, without further testing it is not certain if all subsurface defects were detected. These findings suggest that alternative inspection and/or further processing would be needed for verification of the technique.

When inspecting NaCl (salt) mixed PLA filaments, best results were collected in reflection mode. This finding supports the potential of the IRT technique developed in this project as collecting data in reflection mode was for smaller features than transmission mode.

For untreated harakeke mixed PLA filaments, the sample that had the most of near-surface and potentially subsurface details were from reflection inspection of 0.125wt% untreated harakeke fibres mixed PLA filament. The bulge-shaped region had large and possible unpulped fibres. The thermograms of the bulge region was compared with its original photograph for verification.

For both 10wt% harakeke reinforced PLA and 30wt% harakeke reinforced PP, significant features or texture was identified. As the sizes of the fibres were equal or less than 13 micrometres they are not expected to be identified, however averaged surface and subsurface information was collected.

Overall, the signal data processing techniques developed was able to detect certain types of defect and to characterize their edge structure. The edge definition of defects differed when processing defects at deeper regions of the samples and/or within different types of samples.

It was in general more challenging when inspecting smaller defects at deeper depths. Curved surfaces added an additional complexity. This was particularly for raw or TSR data. The PPT processed data sets however, were still distinguishable in terms of the defects' shapes and sizes.

It is suggested that the current IRT processing technique can detect relatively large defects in polymer composites however further investigation is required to confirm the lower limit in terms of size and depth limit.

5.2 Future recommendations

Thermograms may have revealed the defect's shape, general location and possibly sizes, better calibration and measurements could be used to evaluate the defects' depth and size. For an example, to identify the exact depth of the detected salt particles would need further investigation. Further research is required to identify the sensitivity of setup to frequencies and to confirm if the technique can be used to enable a small-scale increased weight percent (i.e. fibre bundle) to be detected.

There are many variables within the wavelet denoising process that given further research could be better tailored specifically for the thermal imaging data. The impact of emissivity variations on filament samples would also need to be quantified. The local variations along the filaments that were identified such as in the final harakeke samples need to be interrogated further to identify these features conclusively. Furthermore, a conclusive identification of the cause is also important.

Phase unwrapping is given as an area of future work, this should be applied during the PPT processing to eliminate the features it causes which can prevent feature identification. A two-dimensional (2D) phase unwrapping algorithm can be used to process the phase data [117] [118]. Phase shifting the data could be explored to reduce this impact.

Further work could include investigation of the sensitivity of the data to optical effects such as the vignette effect caused by lens distortion which could be eliminated by using a reference frame/image [65].

The findings presented suggested that further processing is needed in order to reveal deeper defects. It is acknowledged that there will always be a maximum detection limit however this barrier could be compensated/lowered by improving the signal data processing procedures or tailoring the external heating. Other inspection methods or destructive testing can be explored further to verify the depth of features, such as the suspected void in Figure 4.45. Advanced thermographic techniques such as dynamic thermal tomography (DTT) could be explored although the time required to collect and process should be considered. DTT has been shown to visualise solids at maximum depth of 4 mm for fibre reinforce plastics [119].

References

[1] Wang, X., Jiang, M., Zhou, Z., Gou, J., & Hui, D. (2017). 3D printing of polymer matrix composites: A review and prospective. *Composites Part B: Engineering, 110,* 442-458.

[2] Noor, N., Shapira, A., Edri, R., Gal, I., Wertheim, L., & Dvir, T. (2019). Tissue Engineering: 3D Printing of Personalized Thick and Perfusable Cardiac Patches and Hearts (Adv. Sci. 11/2019). *Advanced Science, 6*(11), 1970066.

[3] Sanz-Izquierdo, B., & Parker, E. A. (2014). 3-D Printing of Elements in Frequency Selective Arrays. *IEEE Transactions on Antennas and Propagation, 62*(12), 6060-6066.

[4] Leigh, S. J., Bradley, R. J., Purssell, C. P., Billson, D. R., & Hutchins, D. A. (2012). A simple, low-cost conductive composite material for 3D printing of electronic sensors. *PloS one, 7*(11).

[5] Gutierrez, C., Salas, R., Hernandez, G., Muse, D., Olivas, R., MacDonald, E., Irwin, M. D., Wicker, R., Newton, M., & Church, K. (2011). CubeSat fabrication through additive manufacturing and micro-dispensing. In *International Symposium on Microelectronics* (Vol. 2011, pp. 001021-001027): International Microelectronics Assembly and Packaging Society.

[6] Alonso, M. P., Malone, E., Moon, F. C., & Lipson, H. (2012). Reprinting the telegraph: Replicating the Vail register using multi-materials 3D printing. *Cornell. Edu. Web.*

[7] Czyżewski, J., Burzyński, P., Gaweł, K., & Meisner, J. (2009). Rapid prototyping of electrically conductive components using 3D printing technology. *Journal of Materials Processing Technology, 209*(12-13), 5281-5285.

[8] Hamzah, H. H., Shafiee, S. A., Abdalla, A., & Patel, B. A. (2018). 3D printable conductive materials for the fabrication of electrochemical sensors: A mini review. *Electrochemistry Communications, 96,* 27-31.

[9] Masood, S., & Song, W. (2004). Development of new metal/polymer materials for rapid tooling using fused deposition modelling. *Materials & design, 25*(7), 587-594.

[10] Mohan, N., Senthil, P., Vinodh, S., & Jayanth, N. (2017). A review on composite materials and process parameters optimisation for the fused deposition modelling process. *Virtual and Physical Prototyping, 12*(1), 47-59.

[11] Sun, Q., Rizvi, G. M., Bellehumeur, C. T., & Gu, P. (2008). Effect of processing conditions on the bonding quality of FDM polymer filaments. *Rapid Prototyping Journal, 14*(2), 72-80.

[12] Marques, A. T., Esteves, S., Pereira, J. P., & Oliveira, L. M. (Compiler) (2020). *Additive Manufacturing Hybrid Processes for Composites Systems*: Springer.

[13] Blok, L. G., Longana, M. L., Yu, H., & Woods, B. K. S. (2018). An investigation into 3D printing of fibre reinforced thermoplastic composites. *Additive Manufacturing, 22*, 176-186.

[14] Dickson, A. N., Barry, J. N., McDonnell, K. A., & Dowling, D. P. (2017). Fabrication of continuous carbon, glass and Kevlar fibre reinforced polymer composites using additive manufacturing. *Additive Manufacturing, 16*, 146-152.

[15] Stoof, D., & Pickering, K. (2018). Sustainable composite fused deposition modelling filament using recycled pre-consumer polypropylene. *Composites Part B: Engineering $V 135*, 110-118.

[16] Stoof, D., Pickering, K., & Zhang, Y. (2017). Fused deposition modelling of natural fibre/polylactic acid composites. *Journal of Composites Science, 1*(1), 8.

[17] Towsyfyan, H., Biguri, A., Boardman, R., & Blumensath, T. (2020). Successes and challenges in non-destructive testing of aircraft composite structures. *Chinese Journal of Aeronautics, 33*(3), 771-791.

[18] Emerson, M. J., Jespersen, K. M., Dahl, A. B., Conradsen, K., & Mikkelsen, L. P. (2017). Individual fibre segmentation from 3D X-ray computed tomography for characterising the fibre orientation in unidirectional composite materials. *Composites Part A: Applied Science and Manufacturing, 97*, 83-92.

[19] Madra, A., El Hajj, N., & Benzeggagh, M. (2014). X-ray microtomography applications for quantitative and qualitative analysis of porosity in woven glass fiber reinforced thermoplastic. *Composites Science and technology, 95*, 50-58.

[20] Duan, Y., Zhang, H., Maldague, X. P., Ibarra-Castanedo, C., Servais, P., Genest, M., Sfarra, S., & Meng, J. (2019). Reliability assessment of pulsed thermography and ultrasonic testing for impact damage of CFRP panels. *NDT & E International, 102*, 77-83.

[21] Waugh, R. C. (2016). *Development of infrared techniques for practical defect identification in bonded joints*. Springer.

[22] Campeau, F., & Fleitz, J. (2016). *Limited radiography*. Cengage Learning.

[23] Lopez, A., Bacelar, R., Pires, I., Santos, T. G., Sousa, J. P., & Quintino, L. (2018). Non-destructive testing application of radiography and ultrasound for wire and arc additive manufacturing. *Additive Manufacturing, 21*, 298-306.

[24] Avdelidis, N., Gan, T.-H., Ibarra-Castanedo, C., & Maldague, X. (2011). Infrared thermography as a nondestructive tool for materials characterisation and assessment. In *Thermosense: Thermal Infrared Applications XXXIII* (Vol. 8013, pp. 801313): International Society for Optics and Photonics.

[25] Stoof, D., Pickering, Kim., & Zhang, Yuanji. (2017). Fused deposition modelling of natural Fibre/Polylactic acid composites. *Journal of Composites Science; Basel, 1*(1).

[26] Maldague, X., Galmiche, F., & Ziadi, A. (2002). Advances in pulsed phase thermography. *Infrared Physics & Technology, 43*(3), 175-181.

[27] Loera, A. G., Cara, F., Dumon, M., & Pascault, J. P. (2002). Porous Epoxy Thermosets Obtained by a Polymerization-Induced Phase Separation Process of a Degradable Thermoplastic Polymer. *Macromolecules, 35*(16), 6291-6297.

[28] Caulfield, D. F., Clemons, C., Jacobson, R. E., & Rowell, R. M. (2005). 13 Wood Thermoplastic Composites. *Handbook of wood chemistry and wood composites*, 365.

[29] Bunsell, A. R., & Renard, J. (2005). *Fundamentals of fibre reinforced composite materials*. CRC Press.

[30] van Rijswijk, K., & Bersee, H. E. N. (2007). Reactive processing of textile fiber-reinforced thermoplastic composites – An overview. *Composites Part A: Applied Science and Manufacturing, 38*(3), 666-681.

[31] Talreja, R. (2001). *Polymer matrix composites*. Elsevier.

[32] Mohanty, A., Misra, M., & Hinrichsen, G. (2000). Biofibres, Biodegradable Polymers and Biocomposites: An Overview. *Macromolecular Materials and Engineering, 276-277*, 1-24.

[33] Wong, K. V., & Hernandez, A. (2012). A review of additive manufacturing. *International scholarly research notices, 2012*.

[34] Kroll, E., & Artzi, D. (2011). Enhancing aerospace engineering students' learning with 3D printing wind - tunnel models. *Rapid Prototyping Journal*.

[35] Rajak, D. K., Pagar, D. D., Menezes, P. L., & Linul, E. (2019). Fiber-Reinforced Polymer Composites: Manufacturing, Properties, and Applications. *Polymers, 11*(10), 1667.

[36] Pickering, K. L., Efendy, M. A., & Le, T. M. (2016). A review of recent developments in natural fibre composites and their mechanical performance. *Composites Part A: Applied Science and Manufacturing, 83*, 98-112.

[37] Pickering, K. L., Efendy, M. G. A., & Le, T. M. (2015). A review of recent developments in natural fibre composites and their mechanical performance. *Composites Part A: Applied Science and Manufacturing, 83*, 98-112.

[38] Al-Oqla, F. M., & Sapuan, S. M. (2014). Natural fiber reinforced polymer composites in industrial applications: feasibility of date palm fibers for sustainable automotive industry. *Journal of Cleaner Production, 66*, 347-354.

[39] Majka, T. M., & Pielichowski, K. (2019). 15 - Future Perspectives. In K. Pielichowski & T. M. Majka (Eds.), *Polymer Composites with Functionalized Nanoparticles* (pp. 467-470). Elsevier.

[40] Mochane, M. J., Mokhena, T. C., Sadiku, E. R., Ray, S., & Mofokeng, T. (2019). Green Polymer Composites Based on Polylactic Acid (PLA) and Fibers. In *Green Biopolymers and their Nanocomposites* (pp. 29-54). Springer.

[41] Ren, J., Fu, H., Ren, T., & Yuan, W. (2009). Preparation, characterization and properties of binary and ternary blends with thermoplastic starch, poly (lactic

acid) and poly (butylene adipate-co-terephthalate). *Carbohydrate polymers, 77*(3), 576-582.

[42] Oksman, K., Skrifvars, M., & Selin, J.-F. (2003). Natural fibres as reinforcement in polylactic acid (PLA) composites. *Composites science and technology, 63*(9), 1317-1324.

[43] Liu, H., & Zhang, J. (2011). Research Progress in Toughening Modification of Poly(lactic acid). *Journal of Polymer Science Part B: Polymer Physics, 49,* 1051-1083.

[44] Alias, N. F., & Ismail, H. (2019). An overview of toughening polylactic acid by an elastomer. *Polymer-Plastics Technology and Materials, 58*(13), 1399-1422.

[45] Mohammed, L., Ansari, M. N., Pua, G., Jawaid, M., & Islam, M. S. (2015). A review on natural fiber reinforced polymer composite and its applications. *International Journal of Polymer Science, 2015*.

[46] Qiu, T. Y., Song, M., & Zhao, L. G. (2016). Testing, characterization and modelling of mechanical behaviour of poly (lactic-acid) and poly (butylene succinate) blends. *Mechanics of Advanced Materials and Modern Processes, 2*(1), 7.

[47] Faruk, O., Tjong, J., & Sain, M. (2017). *Lightweight and Sustainable Materials for Automotive Applications*. CRC Press.

[48] González-Henríquez, C. M., Sarabia-Vallejos, M. A., & Rodriguez-Hernandez, J. (2019). Polymers for additive manufacturing and 4D-printing: Materials, methodologies, and biomedical applications. *Progress in Polymer Science*.

[49] Yakout, M., & Elbestawi, M. (2017). *Additive Manufacturing of Composite Materials: An Overview*.

[50] Matsuzaki, R., Ueda, M., Namiki, M., Jeong, T.-K., Asahara, H., Horiguchi, K., Nakamura, T., Todoroki, A., & Hirano, Y. (2016). Three-dimensional printing of continuous-fiber composites by in-nozzle impregnation. *Scientific Reports, 6,* 23058.

[51] Wan, L., & Zhang, Y. (2018). Jointly modified mechanical properties and accelerated hydrolytic degradation of PLA by interface reinforcement of PLA-WF. *Journal of the Mechanical Behavior of Biomedical Materials, 88,* 223-230.

[52] Gholizadeh, S. (2016). A review of non-destructive testing methods of composite materials. *Procedia Structural Integrity, 1*, 50-57.

[53] Nikzad, M., Masood, S. H., & Sbarski, I. (2011). Thermo-mechanical properties of a highly filled polymeric composites for Fused Deposition Modeling. *Materials & Design, 32*(6), 3448-3456.

[54] Justo, J., Távara, L., García-Guzmán, L., & París, F. (2018). Characterization of 3D printed long fibre reinforced composites. *Composite Structures, 185*, 537-548.

[55] Caminero, M. A., Chacón, J. M., García-Moreno, I., & Reverte, J. M. (2018). Interlaminar bonding performance of 3D printed continuous fibre reinforced thermoplastic composites using fused deposition modelling. *Polymer Testing, 68*, 415-423.

[56] Cheung, H.-y., Ho, M.-p., Lau, K.-t., Cardona, F., & Hui, D. (2009). Natural fibre-reinforced composites for bioengineering and environmental engineering applications. *Composites Part B: Engineering, 40*(7), 655-663.

[57] Boritu, A., Anghel, V., Constantin, N., Gãvan, A., & Pascu, A. (2011). Non-destructive inspection of composite structures using active IR-thermography methods. *UPB Science Bulletin Series D, 73*, 71-84.

[58] Parvasi, S. M., Xu, C., Kong, Q., & Song, G. (2016). Detection of multiple thin surface cracks using vibrothermography with low-power piezoceramic-based ultrasonic actuator—a numerical study with experimental verification. *Smart Materials and Structures, 25*(5), 055042.

[59] Ishikawa, M., Hatta, H., Habuka, Y., Fukui, R., & Utsunomiya, S. (2013). Detecting deeper defects using pulse phase thermography. *Infrared physics & technology, 57*, 42-49.

[60] Toscano, C., Meola, C., Iorio, M., & Carlomagno, G. (2012). *Porosity and Inclusion Detection in CFRP by Infrared Thermography*. (Vol. 2012).

[61] Manohar, A., & di Scalea, F. L. (2014). Modeling 3D heat flow interaction with defects in composite materials for infrared thermography. *NDT & E International, 66*, 1-7.

[62] Fitzgerald, A., & Berentson-Shaw, J. (2012). Thermography as a screening and diagnostic tool: a systematic review. *NZ Med J, 125*(1351), 80-91.

[63] Almond, D. P., & Pickering, S. G. (2012). An analytical study of the pulsed thermography defect detection limit. *Journal of Applied Physics, 111*(9), 093510.

[64] Avdelidis, N. P., Gan, T.-H., Ibarra-Castanedo, C., & Maldague, X. P. V. (2011). *Infrared thermography as a nondestructive tool for materials characterisation and assessment*. SPIE Defense, Security, and Sensing (Vol. 8013). SPIE.

[65] Ólafsson, G., Tighe, R. C., & Dulieu-Barton, J. M. (2018). Improving the probing depth of thermographic inspections of polymer composite materials. *Measurement Science and Technology, 30*(2), 025601.

[66] Meola, C., Boccardi, S., & Carlomagno, G. M. (2016). *Infrared thermography in the evaluation of aerospace composite materials: infrared thermography to composites*. Woodhead Publishing.

[67] Lu, Q. Y., & Wong, C. H. (2018). Additive manufacturing process monitoring and control by non-destructive testing techniques: challenges and in-process monitoring. *Virtual and Physical Prototyping, 13*(2), 39-48.

[68] Lee, H., Lee, K., Kim, Y., Yim, H., & Bae, D. (2004). Ultrasonic in-situ monitoring of setting process of high-performance concrete. *Cement and Concrete Research, 34*(4), 631-640.

[69] Clark, R. (2004). Rail flaw detection: overview and needs for future developments. *Ndt & E International, 37*(2), 111-118.

[70] Garnier, C., Pastor, M.-L., Eyma, F., & Lorrain, B. (2011). The detection of aeronautical defects in situ on composite structures using Non Destructive Testing. *Composite structures, 93*(5), 1328-1336.

[71] Oguma, I., Goto, R., & Sugiura, T. (2012). Ultrasonic inspection of an internal flaw in a ferromagnetic specimen using angle beam EMATs. *Przeglad Elektrotechniczny, 88*(7B), 78-81.

[72] Lu, Y. (2010). *Non-destructive Evaluation on Concrete Materials and Structures using Cement-based Piezoelectric Sensor*. Hong Kong University of Science and Technology (Hong Kong).

[73] Edwards, R., Sinclair, M., Goldsack, T., Krushelnick, K., Beg, F., Clark, E., Dangor, A., Najmudin, Z., Tatarakis, M., & Walton, B. (2002). Characterization of a gamma-ray source based on a laser-plasma accelerator with applications to radiography. *Applied Physics Letters, 80*(12), 2129-2131.

[74] Rynes, J., Bendahan, J., Gozani, T., Loveman, R., Stevenson, J., & Bell, C. (1999). Gamma-ray and neutron radiography as part of a pulsed fast neutron analysis inspection system. *Nuclear Instruments and Methods in Physics Research Section A: Accelerators, Spectrometers, Detectors and Associated Equipment, 422*(1-3), 895-899.

[75] Ataş, A., & Soutis, C. (2013). Subcritical damage mechanisms of bolted joints in CFRP composite laminates. *Composites Part B: Engineering, 54*, 20-27.

[76] Bayraktar, E., Antolovich, S., & Bathias, C. (2008). New developments in non-destructive controls of the composite materials and applications in manufacturing engineering. *Journal of materials processing technology, 206*(1-3), 30-44.

[77] Maldague, X. (2001). Theory and practice of infrared technology for nondestructive testing.

[78] Corcoran, P. (2011). *Reviews, Refinements and New Ideas in Face Recognition*. BoD–Books on Demand.

[79] Kylili, A., Fokaides, P. A., Christou, P., & Kalogirou, S. A. (2014). Infrared thermography (IRT) applications for building diagnostics: A review. *Applied Energy, 134*, 531-549.

[80] Casana, J., Kantner, J., Wiewel, A., & Cothren, J. (2014). Archaeological aerial thermography: a case study at the Chaco-era Blue J community, New Mexico. *Journal of Archaeological Science, 45*, 207-219.

[81] P. V. Maldague, X. (2002). *Introduction to NDT by active infrared thermography*. (Vol. 60).

[82] Usamentiaga, R., Venegas, P., Guerediaga, J., Vega, L., Molleda, J., & Bulnes, F. G. (2014). Infrared thermography for temperature measurement and non-destructive testing. *Sensors (Basel, Switzerland), 14*(7), 12305-12348.

[83] Measurements, O. I. (2019). *IR-Basics* [Online brochure]. Downloads. Retrieved April, 2019, from https://www.optris.global/search?keywords=OPTPI640033T900&x=14&y=5.

[84] Carlomagno, G. M., & Cardone, G. (2010). Infrared thermography for convective heat transfer measurements. *Experiments in fluids, 49*(6), 1187-1218.

[85] Widmer, L., & Pauchard, A. (2007). Quantum detection: photon counters in comparison. *PHOTONIK-STUTTGART-, 39*(I), 40.

[86] Trout, J. (2020). *What Is Infarred Thermography*. Retrieved Jan, 2020, from https://www.reliableplant.com/infrared-thermography-31572.

[87] Kim, K., & Feng, S. (2016). Thermal Mapping Using Infrared Thermography. In *Application of Thermo-Fluidic Measurement Techniques* (pp. 215-250). Elsevier.

[88] Ciampa, F., Mahmoodi, P., Pinto, F., & Meo, M. (2018). Recent advances in active infrared thermography for non-destructive testing of aerospace components. *Sensors, 18*(2), 609.

[89] Abrate, S. (2005). *Impact on composite structures*. Cambridge university press.

[90] Vavilov, V. P., & Burleigh, D. D. (2015). Review of pulsed thermal NDT: Physical principles, theory and data processing. *NDT & E International, 73*, 28-52.

[91] Ibarra-Castanedo, C., Avdelidis, N. P., & P. Maldague, X. (2005). *Quantitative pulsed phase thermography applied to steel plates*. (Vol. 5782).

[92] Bird, R., Stewart, W., & Lightfoot, E. (Compiler) (2007). *Transport Phenomena, 2nd Edn. New York, NY: John Wilwe & Sons*: Inc.

[93] Duan, Y., Huebner, S., Hassler, U., Osman, A., Ibarra-Castanedo, C., & Maldague, X. P. (2013). Quantitative evaluation of optical lock-in and pulsed thermography for aluminum foam material. *Infrared Physics & Technology, 60*, 275-280.

[94] Maldague, X., Marinetti, S., & Couturier, J.-P. (1997). Applications of pulse phase thermography. In *Review of Progress in Quantitative Nondestructive Evaluation* (pp. 339-344). Springer.

[95] Ibarra-Castanedo, C., & Maldague, X. (2004). Pulsed phase thermography reviewed. *Quantitative InfraRed Thermography Journal, 1*(1), 47-70.

[96] Almond, D. P., Angioni, S. L., & Pickering, S. G. (2017). Long pulse excitation thermographic non-destructive evaluation. *NDT & E International, 87*, 7-14.

[97] Hickel, R. O., & Pollack, F. (1969). Surface temperature mapping with infrared photographic pyrometry for turbine cooling investigations.

[98] Kosugi, A., Ihara, I., & Matsuya, I. (2012). Accuracy evaluation of surface temperature profiling by a laser ultrasonic method. *Japanese Journal of Applied Physics, 51*(7S), 07GB01.

[99] Oswald-Tranta, B. (2017). Time and frequency behaviour in TSR and PPT evaluation for flash thermography. *Quantitative InfraRed Thermography Journal, 14*(2), 164-184.

[100] Lu, X., Tian, G., Wu, J., Gao, B., & Tian, P. (2020). Pulsed Air-flow Thermography for Natural Crack Detection and Evaluation. *IEEE Sensors Journal*.

[101] Shepard, S. M. (2007). Flash thermography of aerospace composites. In *IV Conferencia Panamericana de END Buenos Aires* (Vol. 7).

[102] Pan, M., He, Y., Tian, G., Chen, D., & Luo, F. (2012). Defect characterisation using pulsed eddy current thermography under transmission mode and NDT applications. *Ndt & E International, 52*, 28-36.

[103] Vollmer, M., Henke, S., Karstädt, D., Möllmann, K. P., & Pinno, F. (2004). Identification and Suppression of Thermal Reflections in Infrared Thermal Imaging. *5*.

[104] Balageas, D. L., Roche, J.-M., Leroy, F.-H., Liu, W.-M., & Gorbach, A. M. (2015). The thermographic signal reconstruction method: A powerful tool for the enhancement of transient thermographic images. *Biocybernetics and Biomedical Engineering, 35*(1), 1-9.

[105] Tran, Q. H., Han, D., Kang, C., Haldar, A., & Huh, J. (2017). Effects of Ambient Temperature and Relative Humidity on Subsurface Defect Detection in Concrete Structures by Active Thermal Imaging. *Sensors (Basel, Switzerland), 17*(8), 1718.

[106] Optris infrared sensing, L. (2015). *Optris PI 640 Technical Data* [Optris technical data document]. from https://www.optris.global/thermal-imager-optris-pi-640.

[107] Optris infrared sensing, L. (2015). *Optris PI 640 Technical Data* [Optris technical data document]. Retrieved January, 2020, from https://www.optris.global/thermal-imager-optris-pi-640.

[108] Canon. (2016). *Speedlite 430EX III 430EX III-RT Brochure*. 2019, from https://www.canon.co.nz/speedlite-flashes/speedlite-430ex-iii.

[109] Optris infrared sensing, L. (2015). Infrared camera optris PI 640. Product Program.

[110] Optris Infrared Measurements. (2015). *Infrared camera optris PI 640*. Retrieved July, 2019, from https://www.optris.global/thermal-imager-optris-pi-640.

[111] Technologies, A. C. F. o. A. M., & Terminology, A. C. F. o. A. M. T. S. F. o. (2012). *Standard terminology for additive manufacturing technologies*. ASTM International.

[112] Mahmud, S., & Fraser, R. A. (2003). The second law analysis in fundamental convective heat transfer problems. *International Journal of Thermal Sciences, 42*(2), 177-186.

[113] MathWorks. (2020). *wdenoise, wavelet signal denoising*. Documentation. Retrieved January, 2020, from https://au.mathworks.com/help/wavelet/ref/wdenoise.html#d120e91061.

[114] Shepard, S. M. (Compiler) (2004). *System for generating thermographic images using thermographic signal reconstruction*: Google Patents.

[115] Waugh, R., Dulieu-Barton, J., & Quinn, S. (2014). Modelling and evaluation of pulsed and pulse phase thermography through application of composite and metallic case studies. *Ndt & E International, 66*, 52-66.

[116] Pickering, K., & Stoof, D. (2017). Sustainable Composite Fused Deposition Modelling Filament Using Post-Consumer Recycled Polypropylene. *Journal of Composites Science, 1*, 17.

[117] Gdeisat, M., & Lilley, F. (2016). Two-dimensional phase unwrapping problem. *ljmu. ac. uk, 1*, 1-32.

[118] Cook, M. R., Gee, K. L., Sommerfeldt, S. D., & Neilsen, T. B. (2017). Coherence-based phase unwrapping for broadband acoustic signals. In *Proceedings of Meetings on Acoustics 173EAA* (Vol. 30, pp. 055005): Acoustical Society of America.

[119] Vavilov, V. (2015). Dynamic thermal tomography: Recent improvements and applications. *NDT & E International, 71*.